Modelling of Electrohydrodynamic Droplet Motion under the Influence of Strong Electric Fields

Ouedraogo, Yun

(2020)

Modelling of Electrohydrodynamic Droplet Motion under the Influence of Strong Electric Fields

Elektrohydrodynamische Modellierung von Tropfen unter der Einfluss von starken elektrischen Felder

Zur Erlangung des akademischen Grades Doktor-Ingenieur (Dr.-Ing.)
genehmigte Dissertation von Yun Louis Ouedraogo aus Rennes, France
Tag der Einreichung: 16.03.2020, Tag der Prüfung: 05.06.2020
Darmstadt — D 17

1. Gutachten: PD Dr. rer. nat. habil. Erion Gjonaj
2. Gutachten: Prof. Dr.-Ing. Herbert De Gersem
3. Gutachten: Prof. Dr.-Ing. Cameron Tropea

TECHNISCHE UNIVERSITÄT DARMSTADT

Modelling of Electrohydrodynamic Droplet Motion under the Influence of Strong Electric Fields
Elektrohydrodynamische Modellierung von Tropfen unter der Einfluss von starken elektrischen Felder

Genehmigte Dissertation von Yun Louis Ouedraogo aus Rennes, France

1. Gutachten: PD Dr. rer. nat. habil. Erion Gjonaj
2. Gutachten: Prof. Dr.-Ing. Herbert De Gersem
3. Gutachten: Prof. Dr.-Ing. Cameron Tropea

Tag der Einreichung: 16.03.2020
Tag der Prüfung: 05.06.2020

Darmstadt — D 17

Erklärung laut Promotionsordnung

§8 Abs. 1 lit. c PromO
Ich versichere hiermit, dass die elektronische Version meiner Dissertation mit der schriftlichen Version übereinstimmt.

§8 Abs. 1 lit. d PromO
Ich versichere hiermit, dass zu einem vorherigen Zeitpunkt noch keine Promotion versucht wurde. In diesem Fall sind nähere Angaben über Zeitpunkt, Hochschule, Dissertationsthema und Ergebnis dieses Versuchs mitzuteilen.

§9 Abs. 1 PromO
Ich versichere hiermit, dass die vorliegende Dissertation selbstständig und nur unter Verwendung der angegebenen Quellen verfasst wurde.

§9 Abs. 1 PromO
Die Arbeit hat bisher noch nicht zu Prüfungszwecken gedient.

Darmstadt, den 16.03.2020,

Yun Louis Ouedraogo

“Tout ce qui va arriver peut et doit être prévu.”

Les Shadoks, Jacques Rouxel

Abstract

This work focuses on the numerical study of electrohydrodynamic multiphase fluid flow problems. Liquid bodies experience deformations caused by strong external electric fields. These deformations can be used in industrial applications to accurately control the motion of single droplets. In the limiting case, strong electric fields can force atomisation of fine microdroplets from much larger liquid bulks. Due to differences in the electrical properties of the different fluid phases, the flow affects in turn the electric field distribution.

The analysis of such coupled flows requires numerical modelling of the interdependent hydrodynamic and electrodynamic problems. Since most liquids exhibit some conductivity due to intrinsic ionic species and dissolved impurities, the electrodynamic problem must be modelled by an electroquasistatic model taking into account capacitive, resistive and convective electrical currents. This electroquasistatic problem is coupled to an incompressible fluid flow problem described by the Navier-Stokes equations. Both problems are solved on the same computational grid, using the finite volume method.

The fluid-fluid interface is modelled using the volume of fluid method. The resulting diffuse interface captures the motion of the phase boundaries while efficiently handling topology changes. The motion of contact lines is furthermore modelled using a dynamic contact angle model including hysteresis effects. Pinned contact lines and stick-slip contact line motion in transient problems can therefore be represented. The developed solver is readily applicable to a large range of electrohydrodynamic flow problems.

This work investigates electrohydrodynamic flows occurring in three technical applications. First, the dynamics of sessile droplets subjected to an AC electric field on the surface of an insulator are considered. The dynamics of the oscillating droplets are compared with experimental data. Partial discharge inception fields are then estimated for similar configurations. Secondly, the detachment dynamics of two liquids in an on-demand droplet generator, where droplet detachment is enforced by electric fields, are considered and compared to experimental data. The different conductivities of the liquids are shown to lead to substantially different detachment dynamics. Relevant parameters in the detachment dynamics are extracted from the simulations. Finally, transient electrosprays in the cone-jet mode are characterised for a number of liquids with different electromechanical properties. The charge-radius correlations of the first ejections are found to obey the scaling laws reported in the literature. Moreover, additional scaling laws are found for the subsequent ejections.

Kurzfassung

Diese Arbeit behandelt die numerische Untersuchung von elektrohydrodynamischen Mehrphasenströmungsproblemen. Flüssigkeitsansammlungen können durch starke externe elektrische Felder deformiert werden. In industriellen Anwendungen wird dieser Effekt genutzt, um die Bewegung einzelner Flüssigkeitströpfchen mit hoher Genauigkeit zu steuern. Außerdem werden starke elektrische Felder zur Zerstäubung von Flüssigkeitsansammlungen in Mikrotröpfchen verwendet.

Aufgrund der unterschiedlichen elektrischen Eigenschaften verschiedener Flüssigkeitsphasen bewirkt die Strömungsdynamik eine Rückkopplung auf die Verteilung des elektrischen Feldes. Eine numerische Modellierung derartiger Strömungsprobleme erfordert deshalb eine gekoppelte Lösung der hydrodynamischen und der elektrodynamischen Gleichungen. Weil die meisten Flüssigkeiten eine gewisse Ionenleitfähigkeit aufweisen, ist ein elektroquasistatisches Modell unter Beachtung von kapazitiven, resistiven und konvektiven elektrischen Ströme erforderlich. Dieses Modell wird durch eine Kopplung an das Strömungsproblem für inkompressible Flüssigkeiten erweitert, welches durch die Navier-Stokes-Gleichungen beschrieben wird. Beide Probleme werden auf demselben Rechengitter mittels der Finite-Volumen-Methode gelöst.

Aufgrund des Verhaltens der simulierten Strömungen, das unter anderem Änderungen der Topologie an der Grenzschicht zwischen den Flüssigkeiten beinhaltet, wird die Bewegung der Grenzschicht mittels der Fluidvolumenmethode für diffuse Grenzschichten abgebildet. Außerdem wird die Bewegung der Kontaktlinien mittels eines dynamischen Kontaktwinkelmodells unter Beachtung von Hystereseeffekten modelliert. Dieses Modell erlaubt eine akkurate Beschreibung von Haftgleiteffekten bei transienten Bewegungen der Kontaktlinie. Die entwickelte Lösungsmethode kann leicht auf eine Vielzahl elektrohydrodynamischer Strömungsprobleme angewandt werden.

In dieser Arbeit werden die elektrohydrodynamische Strömungen für drei technische Anwendungen untersucht. Zuerst wird die Dynamik von Tröpfchen auf einem Isolator unter Einfluss eines elektrischen Wechselfelds untersucht. Die Dynamik der oszillierenden Tröpfchen wird mit experimentellen Daten verglichen. Im Anschluss werden die Teilentladungseinsetzfeldstärken in ähnlichen Konfigurationen abgeschätzt. Als zweites wird die feldstärkeninduzierten Ablösedynamik in einem Tröpfchengenerator für zwei verschiedener Flüssigkeiten untersucht und mit Messdaten verglichen. Die unterschiedliche Leitfähigkeit der beiden Flüssigkeiten führt zu substanziellen Unterschieden in der Ablösedynamik. Die relevanten Parameter für die Ablösedynamik werden aus den Simulationen extrahiert. Zuletzt werden transiente Elektrosprays im Cone-Jet Modus für Flüssigkeiten mit unterschiedlichen elektromechanischen Eigen-

schaften charakterisiert. Die Korrelation zwischen Ladung und Radius des zuerst erzeugten Tröpfchens reproduziert bekannte Skalengesetze. Außerdem liefert die Untersuchung modifizierte Skalengesetze für die nachfolgend erzeugten Tröpfchen.

Contents

1 Introduction

Dynamical processes of droplets under the influence of strong electric fields are at the core of many technical applications. Forces induced by the electric field drive fluid motion, which in turn affects the distribution of the driving electric fields. Complex flow patterns can therefore be induced by applying external electric fields. This allows to accurately control droplet motion in applications such as electrowetting [76] and on-demand droplet generation [106]. In other atomisation processes, such as electrospraying [17, 54], electric fields can be used to modulate the size of atomised droplets and the angle of the spray cone. The motion of fluids in these applications depends on both the mechanical and the electrical properties of fluids. The behaviour of these droplet systems is therefore referred as Electrohydrodynamic (EHD).

In general, the coupling between the hydrodynamic and electrodynamic problem describing the dynamical charging effects is non-trivial, so that EHD processes can only be accurately described by the means of numerical simulation. In order to do so, a few challenges related to the nature of the problem at hand must be overcome. In multiphase fluid flow problems, the discontinuities of the material properties and physical quantities across the interface need to be carefully handled. The contact line formed at the intersection of the phase boundary with solids also plays a major role in the dynamics of droplets in strong electric fields and requires a proper dynamic description.

The modelling of the interface is also of importance for the electric problem. For conductive liquids, the discontinuities of the electric displacement and conduction current densities result in the apparition of unbalanced free charge at the interface. This charge redistribution effect can lead to detachment of charged droplets from initially uncharged liquids. Such a configuration can be described neither by the electrostatic nor the steady conduction approximations: an electroquasistatic formulation is required to accurately capture dynamical charging effects.

The time scales of the phenomena associated to the dynamics of the fluids and of free charge are, in many EHD applications, similar. Therefore, a fully coupled multiphase solver is required to provide an accurate description of EHD problems. Such a solver is described in this dissertation. A conduction-convection model captures the dynamics of free charge in the conductive liquids. Droplet merging and splitting events are furthermore efficiently handled by using a diffuse interface representation for the fluid-fluid boundary. In addition, the dynamics of the contact line formed on a surface by the fluid-fluid interface are modelled using a dynamic contact angle model including contact line hysteresis effects. The coupled solver thus obtained is employed to characterise the dynamics of different EHD problems.

1.1 Outline

The thesis is organised as follows. Chapter 2 describes the physical phenomena occurring in EHD flows. A few semi-analytic methods to solve some problems supporting the rest of the work are furthermore described. In Chapter 3, the Finite Volume Method (FVM) and the schemes used to solve the different parts of the EHD problem are introduced. Chapter 4 completes this description with some details on the coupling between the hydrodynamic and electroquasistatic problems. Three applications of interest are presented in Chapters 5 to 7. The dynamics of rain droplets subjected to AC fields on insulating plates and its relation to the inception of partial discharges are described in Chapter 5. An on-demand droplet generator is characterised in Chapter 6, showing strongly conductivity-dependent droplet behaviour. The presented material is partly taken from [83]. Finally, the dynamics of transient electrosprays are considered in Chapter 7. The size and net charge of successively ejected droplets are studied for a range of different test liquids. Parts of the presented results are taken from [82]. Chapter 8 summarises the results and offers an outlook.

1.2 Cooperations

This project was conducted in the framework of the Collaborative Research Center Transregio 75 (SFB-TRR 75) “Droplet Dynamics Under Extreme Ambient Conditions”, within subproject A5. Multiple cooperations have contributed to the results presented in this thesis.

The study of the behaviour of sessile droplets on high-voltage insulators was performed in collaboration with subproject C5 of the SFB-TRR 75: Jens-Michael Löwe and Prof. Dr.-Ing. Volker Hinrichsen (High Voltage Laboratory, Technical University of Darmstadt). The videos of experiments and partial discharge inception voltages presented in Chapter 5 were obtained by subproject C5.

The characterisation of the on-demand droplet generator is the result of a collaborative work with subproject B2 of the SFB-TRR 75: Christoph Steinhausen, Dr.-Ing. Grazia Lamanna, Prof. Dr.-Ing. habil. Bernhard Weigand, (Institute for Aerospace Thermodynamics, University of Stuttgart), Andreas Preusche, Prof. Dr. habil. Andreas Dreizler, (Institute of Reactive Flows and Diagnostics, Technical University of Darmstadt). The experimental results presented in Chapter 6 were obtained by subproject B2.

The load balanced adaptive mesh refinement code used for electrosprays simulations presented in Chapter 7 was developed in collaboration with Daniel Deising (Mathematical Modeling and Applied Analysis, Technical University of Darmstadt) and Dr.-Ing. Daniel Rettenmaier (Graduate School CE; Fluid Mechanics and Aerodynamics, Technical University of Darmstadt).

1.3 Publications

- Y. Ouedraogo, E. Gjonaj, H. De Gersem, and S. Schöps. Simulation of transient electrospray dynamics in conductive fluids. *IEEE Transactions on Magnetics*, 56(2), 2020.
- D. Rettenmaier, D. Deising, Y. Ouedraogo, E. Gjonaj, H. De Gersem, D. Bothe, C. Tropea, and H. Marschall. Load balanced 2D and 3D adaptive mesh refinement in OpenFOAM. *SoftwareX*, 10:100317, 2019.
- Y. Ouedraogo, E. Gjonaj, T. Weiland, H. De Gersem, C. Steinhausen, G. Lamanna, B. Weigand, A. Preusche, and A. Dreizler. Modelling and simulation of electrically controlled droplet dynamics. *Scientific Computing in Electrical Engineering SCEE 2016*, U. Langer, W. Amrhein, W. Zulehner, Eds., pages 101–109, Cham, Springer International Publishing, 2018.
- Y. Ouedraogo, E. Gjonaj, T. Weiland, H. De Gersem, C. Steinhausen, G. Lamanna, B. Weigand, A. Preusche, A. Dreizler, and M. Schremb. Electrohydrodynamic simulation of electrically controlled droplet generation. *International Journal of Heat and Fluid Flow*, 64:120–128, 2017.
- Y. Ouedraogo, E. Gjonaj, T. Weiland, H. De Gersem, C. Steinhausen, G. Lamanna, B. Weigand, A. Preusche and A. Dreizler. Modeling of an Electrically Driven Droplet Generator. *Proceedings of the VII International Conference on Coupled Problems in Science and Engineering*, 2017.

2 Theory of Electrohydrodynamic Flows

2.1 Physical Phenomena in Electrohydrodynamic Flows

2.1.1 Capillary Effects

Surface tension

Surface tension is a property of fluids, originating from molecular forces. At the surface between two immiscible fluids, cohesive forces and adhesive forces are usually not balanced, resulting in a pressure difference across the interface. This pressure difference, depending only on the fluid properties and local interface geometry, follows the Young-Laplace equation [60, 137]:

$$\Delta p = \gamma \left(\frac{1}{R_1} + \frac{1}{R_2} \right), \tag{2.1}$$

where γ is the surface tension, R_1 and R_2 denote the two principal radii of curvature, so that $\left(\frac{1}{R_1} + \frac{1}{R_2}\right)$ is twice the mean local curvature of the surface. The internal pressure tends to deform the interface to minimise its area. Thus, in the absence of external forces, a liquid mass takes a spherical shape. This effect is observed in daily life, through the formation of water droplets. For droplets residing on surfaces, the equilibrium shape is flattened by the influence of gravity.

The surface tension γ varies with temperature, typically decreasing monotonically with increasing temperature and reaching a value of zero at the critical temperature. It is also impacted by the presence and concentration of surfactants and solutes. When the surface tension varies locally due to non uniform conditions, the interface is subjected to Marangoni effects [71, 117], where the gradient of surface tension drives liquid flow in the direction of higher surface tension.

In the absence of surface tension gradients, the surface force originating from the pressure difference acts only in the direction $\mathbf{n}$ normal to the interface. The effective surface tension force density can therefore be written as

$$\mathbf{f}_s = -\Delta p \mathbf{n}\,. \tag{2.2}$$

In this work, only pure fluids are considered, in the absence of temperature gradient and surfactants. Furthermore, it is assumed that any impurities in liquids are in very low concentration and do not affect surface tension. Thus, the expression (2.2) for the surface tension force applies.

Contact line

The intersection between multiple fluids and a solid surface is referred to as contact line. Along this line, two additional surface tension contributions must be considered. Given the situation shown in Fig. 2.1, involving a liquid phase, a gas phase and a solid (indexed respectively with L, G and S) three surface tension contributions, γ_{LS}, γ_{SG} and γ_{LG} act at the contact line. The balance of forces at equilibrium between the three surface tensions, tangential to the solid surface, results in Young's equation:

$$\gamma_{SG} = \gamma_{LG} \cos\theta + \gamma_{SL}\,, \tag{2.3}$$

where θ is the apparent angle between the liquid-gas boundary and the solid surface. At equilibrium, this angle is referred to as the static contact angle.

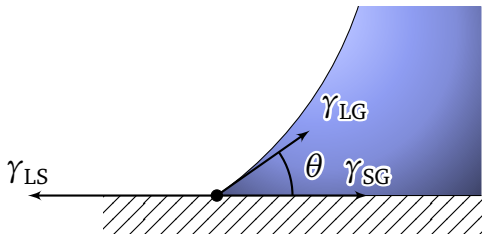

Figure 2.1: Schematic of the surface tension contributions of two fluids and a solid defining a contact line.

The static contact angle is related to the wettability properties of the surface for the involved liquid-gas pair. Low contact angle values are observed for highly wettable surfaces where a given amount of deposited liquid tends to cover a large area. In the limiting case of perfect wettability, $\theta = 0°$, any given amount of liquid expands to cover the entirety of the solid surface. Conversely, low wettability surfaces are characterised by large contact angles and a low contact area. In the limiting case $\theta = 180°$, any given amount of liquid has a single point of contact with the solid surface. In the case of water, the terms hydrophobic and hydrophilic are used, respectively, to qualify surfaces with low and high wettability.

Static contact angle hysteresis

The Young-Laplace equation (2.1) describes the equilibrium contact angle between three phases for ideally smooth and homogeneous surfaces. In presence of surface roughness or material inhomogeneity, the contact line exhibits a so-called contact angle hysteresis [27]. The term hysteresis is used in the literature to indicate that the fluid pair meeting at a surface may exhibit a range of admissible contact angle values at equilibrium, $\theta_{rec} < \theta < \theta_{adv}$. Here, θ_{rec} denotes the minimal contact angle required for the contact line to exhibit receding motion, i.e. motion in the direction of the bulk of the liquid. Conversely, θ_{adv} denotes the maximal angle required for the contact line to exhibit advancing motion. For a given portion of contact line with

contact angle values in the range of static hysteresis, the non-moving contact line is described as being 'pinned' to the surface.

This effect is readily observed on inclined surfaces holding water droplets. The droplet is asymmetrically deformed due to gravity. Yet, the droplet remains pinned on the surface as long as all contact angle values at their contact lines remain in the range of hysteresis (cf. Fig. 2.2).

Dynamic contact angle

When considering the dynamic case, the assumptions of equilibrium contact angles do not hold anymore. As liquids cannot wet nor dewet surfaces instantly, a slight delay is observed in the motion of the contact line compared to the bulk. At the macroscopic scale, this translates to a deviation from the static contact angle value. Various models, e.g. [56, 101, 125, 136], relate the dynamic contact angle to the capillary number $\mathrm{Ca} = \frac{\mu_{\mathrm{liq}} V_{\mathrm{cl}}}{\gamma_{\mathrm{LG}}}$, where μ_{liq} is the dynamic viscosity of the liquid, V_{cl} is the velocity of the contact line and γ_{LG} is the surface tension between the liquid and gas phase, abbreviated as γ. These models are based on both analytic considerations and experimental observations. A sketch of the general behaviour of the dynamic contact angle with respect to the capillary number is shown in Fig. 2.2b. Here, the capillary number is assumed to be positive for an advancing contact line and negative for a receding contact line. The discontinuity at capillary number $\mathrm{Ca} = 0$ in Fig. 2.2b represents static hysteresis.

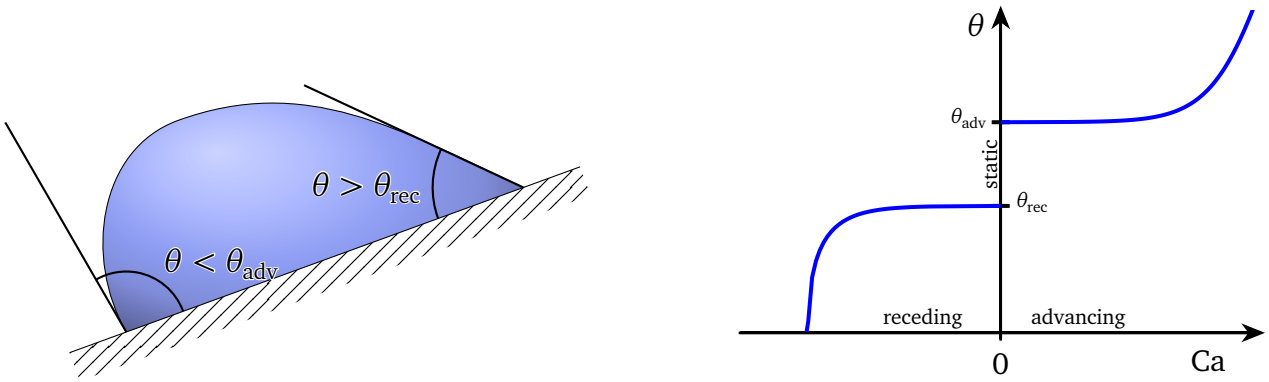

(a) **(b)**

Figure 2.2: Illustration of static and dynamic contact angle hysteresis. (a) Pinned droplet on an inclined surface. The contact angle values at the contact line are within the range of hysteresis, preventing motion of the contact line. (b) Sketch of the dynamic behaviour of the contact angle with respect to the signed capillary number.

Static hysteresis of the contact line introduces the concept of mobility, which qualitatively characterises the ease with which a given contact line can be forced into motion. When the range of hysteresis is large, the associated contact line is said to have a low mobility. In droplets characterised by low mobility, external forces can induce local deformations of the droplet without associated motion of the contact line. The effect is relevant in applications such

as electrowetting, where the application of external electric fields is used to induce motion of the contact line in a controlled manner [76].

In this work, the contact angle is modelled according to Kistler's correlation [56], which relates the value of the dynamic contact angle to the capillary number as

$$\theta_{\mathrm{dyn}} = f_{\mathrm{H}}\left(\mathrm{Ca} + f_{\mathrm{H}}^{-1}(\theta_{\mathrm{adv/rec}})\right), \tag{2.4}$$

where f_{H} is Hoffman's empirical function [49],

$$f_{\mathrm{H}}(x) = \arccos\left(1 - 2\tanh\left[5.16\left(\frac{x}{1+1.31x^{0.99}}\right)^{0.706}\right]\right), \tag{2.5}$$

and f_{H}^{-1} its inverse. The angle $\theta_{\mathrm{adv/rec}}$ takes the value of θ_{adv} or θ_{rec} depending on the sign of the local capillary number.

It should be noted that the contact angle model provides only a macroscopic description. Effects at the microscopic scale are not described by this model. Assuming a no-slip condition at the interface, fluids at solid surfaces undergo a rolling motion [25]. This motion is not compatible with the picture of a moving contact line as described above [50]. It leads to a stress singularity, implying that the hypotheses of the continuum representation of the flow does not hold at the contact line. The issue of the stress singularity is solved in the numerical model by applying a special contact angle boundary condition.

2.1.2 Electrohydrodynamic Forces

In dielectric materials, electric charges are bound in the individual molecules. The response of the material to external fields is due to dipole moments of these molecules. When an external electric field is applied, the dipolar moments tend to align with the electric field. A polarisation density field, $\mathbf{P}$, thus arises in reaction to the application of the electric field $\mathbf{E}$. Typical liquids are isotropic and linear dielectric media, so that the polarisation density is

$$\mathbf{P} = \varepsilon_0 \chi_{\mathrm{e}} \mathbf{E} = (\varepsilon - \varepsilon_0)\mathbf{E}, \tag{2.6}$$

where ε_0 is electric permittivity of free space, χ_{e} the electric susceptibility of the material and ε the permittivity of the material. The electric displacement field, $\mathbf{D}$, defined as

$$\mathbf{D} = \varepsilon_0 \mathbf{E} + \mathbf{P} = \varepsilon \mathbf{E}, \tag{2.7}$$

combines the electric field and polarisation density. $\mathbf{D}$ obeys Gauss's law, relating it to the density ϱ_{e} of free charge:

$$\nabla \cdot \mathbf{D} = \varrho_{\mathrm{e}}. \tag{2.8}$$

The electric force on dielectrics can be calculated by integrating the force on dipoles. The force acting on a single dipole $\mathbf{p}$ is

$$\mathbf{F} = (\mathbf{p} \cdot \nabla)\mathbf{E}\,. \tag{2.9}$$

Taking the polarisation density in the dielectric as $\mathbf{P} = n\mathbf{p}$, where n is the density of dipoles, the Kelvin polarisation force density is obtained as [74, p. 3.6]

$$\mathbf{f}_\mathrm{p} = (\mathbf{P} \cdot \nabla)\mathbf{E}\,. \tag{2.10}$$

The total electric force density including the force on free charges is then

$$\mathbf{f}_\mathrm{e} = \varrho_\mathrm{e}\mathbf{E} + \mathbf{f}_\mathrm{p} = \varrho_\mathrm{e}\mathbf{E} + (\mathbf{P} \cdot \nabla)\mathbf{E}\,. \tag{2.11}$$

In the EHD case considered here, due to the absence of magnetic materials and low velocities involved, the electric field is irrotational, i.e. $\nabla \times \mathbf{E} = 0$. Using the vector identity $\frac{1}{2}\nabla(\mathbf{E}^2) = (\mathbf{E} \cdot \nabla)\mathbf{E} + \mathbf{E} \times (\nabla \times \mathbf{E})$ and substituting (2.6) in (2.10), the polarisation force density can be rewritten as

$$\mathbf{f}_\mathrm{p} = \frac{1}{2}(\varepsilon - \varepsilon_0)\nabla(\mathbf{E} \cdot \mathbf{E}) \tag{2.12}$$

$$= \frac{1}{2}\nabla[(\varepsilon - \varepsilon_0)\mathbf{E} \cdot \mathbf{E}] - \frac{1}{2}(\mathbf{E} \cdot \mathbf{E})\nabla\varepsilon\,. \tag{2.13}$$

The electric force density can also be calculated from the variation of energy stored in the electric field. The electrostatic energy density W stored in a dielectric medium is

$$W = \int_0^{\mathbf{D}} \mathbf{E}(\alpha_1, \ldots, \alpha_n, \mathbf{D}') \cdot \mathrm{d}\mathbf{D}'\,. \tag{2.14}$$

Here, the notation $\mathbf{E}(\alpha_1, \ldots, \alpha_n, \mathbf{D})$ represents the constitutive law for the dielectric medium, where the $\alpha_i, 1 \leq i \leq n$ are parameters corresponding to the physical model. The force density acting on the medium is then given by [74, p. 3.11]:

$$\mathrm{f}_\mathrm{KH} = \varrho_\mathrm{e}\mathbf{E} - \sum_{i=1}^{n} \alpha_i \nabla\left(\frac{\partial W}{\partial \alpha_i}\right). \tag{2.15}$$

Equation (2.15) is commonly referred as the Korteweg-Helmholtz force density.

For a linear and isotropic dielectric medium, the constitutive law takes the form

$$\mathbf{E} = \frac{1}{(1 + \chi_\mathrm{e})\varepsilon_0}\mathbf{D}\,. \tag{2.16}$$

For incompressible fluids where the electric susceptibility remains constant, the electrostatic energy density is thus

$$W = \int_0^{\mathbf{D}} \frac{1}{(1+\chi_e)\varepsilon_0} \mathbf{D} \cdot \mathrm{d}\mathbf{D} = \frac{\mathbf{D}\cdot\mathbf{D}}{2(1+\chi_e)\varepsilon_0}. \tag{2.17}$$

so that

$$\frac{\partial W}{\partial \chi_e} = -\frac{\mathbf{D}\cdot\mathbf{D}}{2(1+\chi_e)^2\varepsilon_0} = -\frac{\varepsilon_0}{2}\mathbf{E}\cdot\mathbf{E}. \tag{2.18}$$

The Korteweg-Helmholtz force density (2.15) becomes

$$\mathrm{f}_{\mathrm{KH}} = \varrho_e \mathbf{E} + \frac{\chi_e \varepsilon_0}{2}\nabla(\mathbf{E}\cdot\mathbf{E}) = \varrho_e \mathbf{E} + \frac{1}{2}(\varepsilon - \varepsilon_0)\nabla(\mathbf{E}\cdot\mathbf{E}), \tag{2.19}$$

thus recovering the expression for the polarisation force density (2.12).

The force densities can also be directly derived from the electric field and the permittivity, as the divergence of electromechanical stress tensors [74, p. 3.18]. Consider the coordinate system indexed with (x_1, x_2, x_3), with unitary vectors $(\mathbf{u}_1, \mathbf{u}_2, \mathbf{u}_3)$. Writing D_i and E_i, $i \in \{1,2,3\}$, the components of $\mathbf{D}$ and $\mathbf{E}$ respectively, and $E^2 = \mathbf{E}\cdot\mathbf{E}$, the total electric force density can be written, using the Kelvin polarisation force density (2.12), as:

$$\begin{aligned}
\mathbf{f}_e &= \varrho_e \mathbf{E} + \frac{1}{2}(\varepsilon - \varepsilon_0)\nabla(\mathbf{E}\cdot\mathbf{E}) && (2.20)\\
&= (\nabla\cdot\mathbf{D})\mathbf{E} + \frac{1}{2}(\varepsilon - \varepsilon_0)\nabla(\mathbf{E}\cdot\mathbf{E}) && (2.21)\\
&= \sum_{k=1}^{3}\left(\sum_{i=1}^{3}\frac{\partial D_i}{\partial x_i}E_k + \frac{1}{2}(\varepsilon-\varepsilon_0)\frac{\partial E^2}{\partial x_k}\right)\mathbf{u}_k && (2.22)\\
&= \sum_{k=1}^{3}\left(\sum_{i=1}^{3}\frac{\partial D_i}{\partial x_i}E_k + \frac{\varepsilon}{2}\frac{\partial E^2}{\partial x_k} - \frac{\varepsilon_0}{2}\frac{\partial E^2}{\partial x_k}\right)\mathbf{u}_k && (2.23)\\
&= \sum_{k=1}^{3}\left(\sum_{i=1}^{3}\frac{\partial D_i}{\partial x_i}E_k + \varepsilon\sum_{i=1}^{3}\frac{\partial E_i}{\partial x_k}E_i - \frac{\varepsilon_0}{2}\frac{\partial E^2}{\partial x_k}\right)\mathbf{u}_k. && (2.24)
\end{aligned}$$

Since $\mathbf{E}$ is irrotational, $\frac{\partial E_i}{\partial x_k} = \frac{\partial E_k}{\partial x_i}$, so that (2.24) becomes

$$\begin{aligned}
\mathbf{f}_e &= \sum_{k=1}^{3}\left(\sum_{i=1}^{3}\frac{\partial D_i}{\partial x_i}E_k + \varepsilon\sum_{i=1}^{3}\frac{\partial E_k}{\partial x_i}E_i - \frac{\varepsilon_0}{2}\frac{\partial E^2}{\partial x_k}\right)\mathbf{u}_k && (2.25)\\
&= \sum_{k=1}^{3}\left(\sum_{i=1}^{3}\frac{\partial D_i}{\partial x_i}E_k + \sum_{i=1}^{3}\frac{\partial E_k}{\partial x_i}D_i - \frac{\varepsilon_0}{2}\frac{\partial E^2}{\partial x_k}\right)\mathbf{u}_k && (2.26)\\
&= \sum_{k=1}^{3}\left(\sum_{i=1}^{3}\frac{\partial D_i E_k}{\partial x_i} - \frac{\varepsilon_0}{2}\frac{\partial E^2}{\partial x_k}\right)\mathbf{u}_k. && (2.27)
\end{aligned}$$

Introducing the Kronecker delta δ_{ik},

$$\delta_{ik} = \begin{cases} 1, & \text{if } i = k \\ 0 & \text{otherwise} \end{cases}, \tag{2.28}$$

Equation (2.27) can be rewritten as

$$\mathbf{f}_\mathrm{e} = \sum_{k=1}^{3}\sum_{i=1}^{3}\left(\frac{\partial D_i E_k}{\partial x_i} - \frac{\varepsilon_0}{2}\frac{\partial E^2}{\partial x_i}\delta_{ik}\right)\mathbf{u}_k\,. \tag{2.29}$$

The corresponding electromechanical stress tensor $\mathbb{T}_\mathrm{e}$ so that $\mathbf{f}_\mathrm{e} = \nabla\cdot\mathbb{T}_\mathrm{e}$ can then be identified as

$$\mathbb{T}_\mathrm{e} = \mathbf{D}\otimes\mathbf{E} - \frac{\varepsilon_0}{2}E^2\mathbb{I} = \varepsilon\mathbf{E}\otimes\mathbf{E} - \frac{\varepsilon_0}{2}E^2\mathbb{I}, \tag{2.30}$$

where $\otimes$ is the dyadic product and $\mathbb{I}$ the unit tensor.

Alternatively, another electromechanical stress tensor can be derived from (2.13). In the case of incompressible flow, the conservative term $\frac{1}{2}\nabla[(\varepsilon-\varepsilon_0)\mathbf{E}\cdot\mathbf{E}]$ can be integrated to the pressure, yielding the same resulting flow [74, p. 3.13]. The effective electric force derived from (2.13) then becomes

$$\begin{aligned}
\mathbf{f}_\mathrm{e} &= \varrho_\mathrm{e}\mathbf{E} - \frac{1}{2}(\mathbf{E}\cdot\mathbf{E})\nabla\varepsilon && (2.31)\\
&= (\nabla\cdot\mathbf{D})\,\mathbf{E} - \frac{1}{2}(\mathbf{E}\cdot\mathbf{E})\nabla\varepsilon && (2.32)\\
&= \sum_{k=1}^{3}\left(\sum_{i=1}^{3}\frac{\partial D_i}{\partial x_i}E_k - \frac{1}{2}E^2\frac{\partial\varepsilon}{\partial x_k}\right)\mathbf{u}_k && (2.33)\\
&= \sum_{k=1}^{3}\left(\sum_{i=1}^{3}\frac{\partial D_i}{\partial x_i}E_k - \frac{1}{2}\frac{\partial\varepsilon E^2}{\partial x_k} + \frac{\varepsilon}{2}\frac{\partial E^2}{\partial x_k}\right)\mathbf{u}_k && (2.34)\\
&= \sum_{k=1}^{3}\left(\sum_{i=1}^{3}\frac{\partial D_i}{\partial x_i}E_k + \varepsilon\sum_{i=1}^{3}\frac{\partial E_i}{\partial x_k}E_i - \frac{1}{2}\frac{\partial\varepsilon E^2}{\partial x_k}\right)\mathbf{u}_k\,. && (2.35)
\end{aligned}$$

Rearranging the terms of (2.35) similarly to (2.24), an electromechanical tensor can be identified as

$$\mathbb{T}'_\mathrm{e} = \varepsilon\mathbf{E}\otimes\mathbf{E} - \frac{\varepsilon}{2}E^2\mathbb{I}. \tag{2.36}$$

The expression (2.36) is similar, but not equal, to (2.30).

In this work, for numerical calculations, the total electrically induced force density is calculated from the stress tensor $\mathbb{T}'_\mathrm{e}$ so that

$$\mathbf{f}_\mathrm{e} = \nabla\cdot\left(\varepsilon\mathbf{E}\otimes\mathbf{E} - \frac{\varepsilon}{2}E^2\mathbb{I}\right). \tag{2.37}$$

This expression allows for the application of Gauss' theorem using in the discretisation procedure, as detailed in Section 3.1.2.

2.1.3 Free Charge Dynamics in Conductive Liquids

In problems involving only perfect dielectrics and in the absence of initial net charge, the free charge density ϱ_e in (2.8) and (2.11) remains zero. However, many liquids exhibit a significant electrical conductivity. This conductivity arises from the presence of free ionic species in the bulk of the liquid. These may originate from dissolved impurities or from self-dissociation of the liquid itself. Three mechanisms are responsible for the dynamics of free charges in liquids: conduction, diffusion and convective transport. In the following, the equations governing free charge dynamics are derived following the analysis from [97].

When an electric field $\mathbf{E}$ is applied to the liquid, the conservation equation for a charged species i with concentration n_i, mobility ω_i and valency z_i reads

$$\frac{\partial n_i}{\partial t} + \nabla \cdot (n_i \mathbf{u}) = \nabla \cdot (\omega_i k_B T \nabla n_i) \mp \nabla \cdot (\omega_i n_i z_i e \mathbf{E}) + r_i \,, \tag{2.38}$$

where e is the elementary charge, k_B Boltzmann's constant and T the temperature. $\mp$ indicates that the term $\nabla \cdot (\omega_i n_i z_i e \mathbf{E})$ is subtracted for positive charge, and added for negative charge.

In (2.38), the term $\nabla \cdot n_i \mathbf{u}$ represents the convective transport of the charged species by the fluid flow. The terms on the right hand side describe diffusion and conduction processes; r_i denotes the reaction source term describing generation and recombination of the ionic species.

Consider first a reaction between an anion A^{z_A-} and a cation C^{z_C+}, producing a neutral species N. The reaction is of the form

$$k_A A^{z_A-} + k_C C^{z_C+} \rightleftharpoons k_N N \,, \tag{2.39}$$

where k_A, k_C and k_N are the stoichiometric factors associated to the reaction. The reaction rates are $K_r n_a^{k_a} n_c^{k_c}$ for the recombination reaction and $K_d n_N^{k_N}$ for the dissociation reaction. At equilibrium, the two reactions occur with the same rate, so that

$$K_r n_a^{k_a} n_c^{k_c} = K_d n_N^{k_N} \,. \tag{2.40}$$

For each of the three species considered, (2.38) reads:

$$\frac{\partial n_A}{\partial t} + \nabla \cdot (n_A \mathbf{u}) = \nabla \cdot (\omega_A k_B T \nabla n_A) + \nabla \cdot (\omega_A n_A z_A e \mathbf{E}) + k_A \left(K_d n_N^{k_N} - K_r n_A^{k_A} n_C^{k_C} \right) , \tag{2.41a}$$

$$\frac{\partial n_C}{\partial t} + \nabla \cdot (n_C \mathbf{u}) = \nabla \cdot (\omega_C k_B T \nabla n_C) - \nabla \cdot (\omega_C n_C z_C e \mathbf{E}) + k_C \left(K_d n_N^{k_N} - K_r n_A^{k_A} n_C^{k_C} \right) , \tag{2.41b}$$

$$\frac{\partial n_N}{\partial t} + \nabla \cdot (n_N \mathbf{u}) = \nabla \cdot (\omega_N k_B T \nabla n_N) - k_N \left(K_d n_N^{k_N} - K_r n_A^{k_A} n_C^{k_C} \right) . \tag{2.41c}$$

By combining (2.41c) and (2.41a) and (2.41b), such that the reaction term cancels, one obtains

$$\frac{\partial}{\partial t}\left(n_\mathrm{A}+\frac{k_\mathrm{A}}{k_\mathrm{N}}n_\mathrm{N}\right)+\nabla\cdot\left[\left(n_\mathrm{A}+\frac{k_\mathrm{A}}{k_\mathrm{N}}n_\mathrm{N}\right)\mathbf{u}\right]=\nabla\cdot\left[\omega_\mathrm{A}k_\mathrm{B}T\nabla\left(n_\mathrm{A}+\frac{k_\mathrm{A}}{k_\mathrm{N}}n_\mathrm{N}\right)\right]+\nabla\cdot(\omega_\mathrm{A}n_\mathrm{A}z_\mathrm{A}e\mathbf{E})\,, \tag{2.42a}$$

$$\frac{\partial}{\partial t}\left(n_\mathrm{C}+\frac{k_\mathrm{C}}{k_\mathrm{N}}n_\mathrm{N}\right)+\nabla\cdot\left[\left(n_\mathrm{C}+\frac{k_\mathrm{C}}{k_\mathrm{N}}n_\mathrm{N}\right)\mathbf{u}\right]=\nabla\cdot\left[\omega_\mathrm{C}k_\mathrm{B}T\nabla\left(n_\mathrm{C}+\frac{k_\mathrm{C}}{k_\mathrm{N}}n_\mathrm{N}\right)\right]-\nabla\cdot(\omega_\mathrm{C}n_\mathrm{C}z_\mathrm{C}e\mathbf{E})\,. \tag{2.42b}$$

For this pair of ionic species, the total free charge density reads $\varrho_\mathrm{e}=n_\mathrm{C}z_\mathrm{C}e-n_\mathrm{A}z_\mathrm{A}e$. Combining (2.42b) and (2.42a) yields

$$\begin{aligned}\frac{\partial\varrho_\mathrm{e}}{\partial t}+\frac{\partial}{\partial t}\left(\frac{k_\mathrm{C}z_\mathrm{C}-k_\mathrm{A}z_\mathrm{A}}{k_\mathrm{N}}en_\mathrm{N}\right)+\nabla\cdot(\varrho_\mathrm{e}\mathbf{u})+\nabla\cdot\left(\frac{k_\mathrm{C}z_\mathrm{C}-k_\mathrm{A}z_\mathrm{A}}{k_\mathrm{N}}en_\mathrm{N}\mathbf{u}\right)=\\ -\nabla\cdot\left[(\omega_\mathrm{C}z_\mathrm{C}n_\mathrm{C}+\omega_\mathrm{A}z_\mathrm{A}n_\mathrm{A})e^2\mathbf{E}\right]+k_\mathrm{B}Te\nabla\cdot(\omega_\mathrm{C}z_\mathrm{C}\nabla n_\mathrm{C}-\omega_\mathrm{A}z_\mathrm{A}\nabla n_\mathrm{A})\\ +k_\mathrm{B}Te\frac{\omega_\mathrm{N}}{k_\mathrm{N}}\nabla\cdot\left[\frac{k_\mathrm{C}z_\mathrm{C}-k_\mathrm{A}z_\mathrm{A}}{k_\mathrm{N}}\nabla n_\mathrm{N}\right].\end{aligned} \tag{2.43}$$

Noticing that $k_\mathrm{C}z_\mathrm{C}-k_\mathrm{A}z_\mathrm{A}=0$, all terms depending on n_N cancel out, yielding:

$$\frac{\partial\varrho_\mathrm{e}}{\partial t}+\nabla\cdot(\varrho_\mathrm{e}\mathbf{u})=-\nabla\cdot\left[(\omega_\mathrm{C}z_\mathrm{C}n_\mathrm{C}+\omega_\mathrm{A}z_\mathrm{A}n_\mathrm{A})e^2\mathbf{E}\right]+k_\mathrm{B}Te\nabla\cdot(\omega_\mathrm{C}z_\mathrm{C}\nabla n_\mathrm{C}-\omega_\mathrm{A}z_\mathrm{A}\nabla n_\mathrm{A})\,. \tag{2.44}$$

Equation (2.44) can be rewritten in dimensionless form as:

$$\frac{\tau_\mathrm{D}}{\tau_\mathrm{P}}\frac{\partial\varrho_\mathrm{e}}{\partial t}+\mathrm{Pe}\nabla\cdot(\varrho_\mathrm{e}\mathbf{u})=-\beta\nabla\cdot[(\omega_\mathrm{C}z_\mathrm{C}n_\mathrm{C}+\omega_\mathrm{A}z_\mathrm{A}n_\mathrm{A})\mathbf{E}]+\nabla\cdot(\omega_\mathrm{C}z_\mathrm{C}\nabla n_\mathrm{C}-\omega_\mathrm{A}z_\mathrm{A}\nabla n_\mathrm{A})\,, \tag{2.45}$$

where $\tau_\mathrm{D}=l^2/\omega_N k_\mathrm{B}T$ is a characteristic diffusion time, τ_P is the time scale of the transport process, $\mathrm{Pe}=l^2\varepsilon_0E_0^2/\mu\omega_N k_\mathrm{B}T$ is the Péclet number, ratio of ion transfer rate by convection to diffusion, and $\beta=leE_0/k_\mathrm{B}T$ is a dimensionless field strength. Considering typical values $E_0=10\,\mathrm{kV\,m^{-1}}$, $l=1\,\mathrm{mm}$, $\mu=1\,\mathrm{mN\,m^{-1}}$, $\omega_\mathrm{N}=2\times10^{11}\,\mathrm{m^2\,V^{-1}\,s^{-1}}$, $T=293\,\mathrm{K}$, the characteristic quantities are $\tau_\mathrm{D}\approx1\times10^3\,\mathrm{s}$, $\mathrm{Pe}\approx1\times10^5$ and $\beta\approx5000$. Under these conditions, the diffusion term is negligible compared to the other terms in (2.45). Furthermore, the term $(\omega_\mathrm{C}z_\mathrm{C}n_\mathrm{C}+\omega_\mathrm{A}z_\mathrm{A}n_\mathrm{A})e^2$ in (2.44) can be identified as the electrical conductivity κ.

Thus, (2.44) reduces to the charge conservation equation in a moving fluid with velocity $\mathbf{u}$

$$\frac{\partial\varrho_\mathrm{e}}{\partial t}+\nabla\cdot(\varrho_\mathrm{e}\mathbf{u})+\nabla\cdot(\kappa\mathbf{E})=0\,. \tag{2.46}$$

Equation (2.46) is the form taken by the charge conservation equation under the assumption of the Taylor-Melcher leaky dielectric model [75], where charge diffusion phenomena are neglected. Note that under this assumption, for a homogeneous and initially uncharged liquid, free charge can only arise at the interface. The bulk of the liquid can acquire free charge only from convection effects from the charged interface since the initial divergence of the electric field vanishes. Electrical conduction opposes the presence of free charges in the volume by tending to push charges out of the volume, towards the interface.

Electroquasistatic problem

Equation (2.44) cannot be solved by itself, as it requires the knowledge of the electric field. Thus, Gauss's law, (2.8), is used in order to obtain the electric field. In the absence of magnetic materials, the typical time scale of magnetic effects, $\tau_\mathrm{m} = \mu\kappa l^2$, is short compared to the time scale of charge relaxation $\tau_\mathrm{e} = \frac{\kappa}{\varepsilon}$, so that the electroquasistatic approximation applies. An electric potential Φ can be introduced, with $-\nabla\Phi = \mathbf{E}$.

Equation (2.46) can be reformulated as

$$\frac{\partial \varrho_\mathrm{e}}{\partial t} + \nabla\cdot(\varrho_\mathrm{e}\mathbf{u}) = \nabla\cdot(\kappa\nabla\Phi)\,, \tag{2.47}$$

where the electric potential Φ is calculated from Gauss's law

$$\nabla\cdot(\varepsilon\nabla\Phi) = -\varrho_\mathrm{e}\,. \tag{2.48}$$

The two equations (2.47) and (2.48), when complemented with boundary and initial conditions, completely describe the electroquasistatic problem. Furthermore, this formulation provides directly a solution for the free charge density which is often a quantity of interest in droplet applications.

Hydrodynamic problem

The conservation of mass for fluids with velocity $\mathbf{u}$ and density ρ reads

$$\frac{\partial \rho}{\partial t} + \nabla\cdot(\rho\mathbf{u}) = 0\,. \tag{2.49}$$

In the absence of strong pressure gradients, the fluids can be considered as incompressible, so that ρ remains constant. Then, (2.49), reduces to

$$\nabla\cdot\mathbf{u} = 0\,. \tag{2.50}$$

The conservation of momentum is described by the Navier-Stokes equation,

$$\frac{\partial \rho\mathbf{u}}{\partial t} + \nabla\cdot(\rho\mathbf{u}\otimes\mathbf{u}) = -\nabla p + \nabla\cdot\left(\mu\left(\nabla\mathbf{u} + \nabla\mathbf{u}^\mathsf{T}\right)\right) + \rho\mathbf{g} + \mathbf{f}_\mathrm{s} + \mathbf{f}_\mathrm{e}\,, \tag{2.51}$$

where p is the pressure and μ the dynamic viscosity. The source term $\rho\mathbf{g}$ is the gravitational force density; the other source terms, $\mathbf{f}_\mathrm{s}$ and $\mathbf{f}_\mathrm{e}$ are, respectively, the surface tension force density at the fluid-fluid interface and the force density originating from the electric field, described in Sections 2.1.1 and 2.1.2. The set of equations (2.47), (2.48), (2.50) and (2.51) provides a complete description of electrohydrodynamic processes in electroquasistatic approximation.

2.2 Analytical and Semi-analytical Solutions of Supporting Problems

Due to complex electrohydrodynamic interactions, numerical simulations are usually required for the study of electrohydrodynamic processes in millimetric droplets. Analytical and semi-analytical calculations can nevertheless be performed for some simple droplet configurations. In this section, a few supporting formulas and considerations that are later using electrohydrodynamic simulations are detailed.

2.2.1 Pendant and Sessile Droplets at Equilibrium

The shapes of static pendant droplets are of interest for acquiring insight into droplet formation from a capillary as well as for measurements of surface tension [61, 94]. The calculation of axisymmetric shapes for pendant droplets at equilibrium can be performed in a semi-analytical manner. Consider an axisymmetric pendant liquid drop at hydrostatic equilibrium as shown in Fig. 2.3. Let ρ_l denote the density of the liquid, ρ_g the density of the surrounding gas, $\Delta\rho = \rho_l - \rho_g$, and γ the surface tension for the liquid-gas pair. The pressure difference across the interface is given by the Young-Laplace equation $\Delta p = \gamma\left(\frac{1}{R_1} + \frac{1}{R_2}\right)$. At hydrostatic equilibrium, the pressure difference may also be written $\Delta p = \Delta p_0 - \Delta\rho g z$, where Δp_0 is the pressure difference at the apex of the droplet. Combining the two equations for the pressure difference yields

$$\gamma\left(\frac{1}{R_1} + \frac{1}{R_2}\right) = \Delta p_0 - \Delta\rho g z\,, \tag{2.52}$$

at all points of the interface.

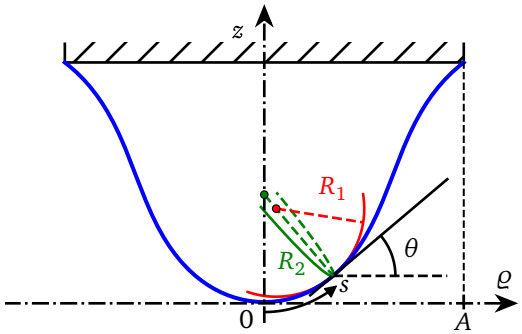

Figure 2.3: Surface of an axisymmetric pendant droplet.

At the apex of the droplet, the principal radii of curvature are equal: $R_1 = R_2 = b$. Thus, (2.52) can be rewritten using the apex curvature b as

$$\gamma\left(\frac{1}{R_1} + \frac{1}{R_2}\right) = \frac{2\gamma}{b} - \Delta\rho g z\,. \tag{2.53}$$

Denoting s the arc length of the interface profile from the origin (see Fig. 2.3), the radii of curvature $R_1(s)$ and $R_2(s)$ can be calculated as

$$\frac{1}{R_1} = \frac{\mathrm{d}\theta}{\mathrm{d}s}, \tag{2.54}$$

$$\frac{1}{R_2} = \frac{\sin(\theta)}{\varrho}. \tag{2.55}$$

Introducing (2.54) and (2.55) into (2.53) yields

$$\frac{\mathrm{d}\theta}{\mathrm{d}s} + \frac{\sin(\theta)}{\varrho} = \frac{2}{b} - \frac{\Delta\rho g z}{\gamma}. \tag{2.56}$$

Using the relations

$$\frac{\mathrm{d}\varrho}{\mathrm{d}s} = \cos(\theta), \tag{2.57}$$

$$\frac{\mathrm{d}z}{\mathrm{d}s} = \sin(\theta), \tag{2.58}$$

and introducing the capillary constant

$$c = \frac{\Delta\rho g}{\gamma}, \tag{2.59}$$

a system of equations is obtained as

$$\begin{cases} \mathrm{d}\varrho &= \cos(\theta)\mathrm{d}s, \\ \mathrm{d}z &= \sin(\theta)\mathrm{d}s, \\ \mathrm{d}\theta &= \left(\frac{2}{b} - \frac{\sin(\theta)}{\varrho} - cz\right)\mathrm{d}s. \end{cases} \tag{2.60}$$

Combined with the initial conditions $\varrho = 0$, $z = 0$, $\theta = 0$, (2.60) defines the shape of pendant droplets as a function of the curvature b at the apex of the droplet. The system of equations can be numerically integrated, using, e.g., the Runge-Kutta-Fehlberg RKF45 method [29]. The integration itself does not include information about the actual constraints of the problem (capillary radius, contact angle, droplet volume, etc.). One of these parameters must therefore be used as end condition for the integration to obtain the actual droplet shape.

The typical constraints for the integration of the droplet shape are the volume of the droplet and either the contact angle with the surface of contact or the radius of the contact line. One of the constraints is guaranteed to be fulfilled by the end condition for the integration. For the other constraint, the initial radius of curvature typically has to be varied to ensure that the integrated droplet shape fulfils both criteria.

The same analysis can be performed for sessile droplets [94], by integrating the system of equations

$$\begin{cases} \mathrm{d}\varrho &= \cos(\theta)\mathrm{d}s\,, \\ \mathrm{d}z &= \sin(\theta)\mathrm{d}s\,, \\ \mathrm{d}\theta &= \left(-\dfrac{2}{b} - \dfrac{\sin(\theta)}{\varrho} + cz\right)\mathrm{d}s\,, \end{cases} \tag{2.61}$$

which is similar to (2.60).

It should be noted that the same end conditions may be fulfilled by different droplet shapes with the same apex curvature radius. Consider the situation shown in Fig. 2.4. The three droplet shapes are integrated with the same apex curvature; the capillary radius is used as end condition. The number of crossings of the $\varrho = a$ line determines the shape of the droplet, which can be classified in three types. Droplets of type II have an equator, droplets of type III have both an equator and a neck, while droplets of type I exhibit none of these features.

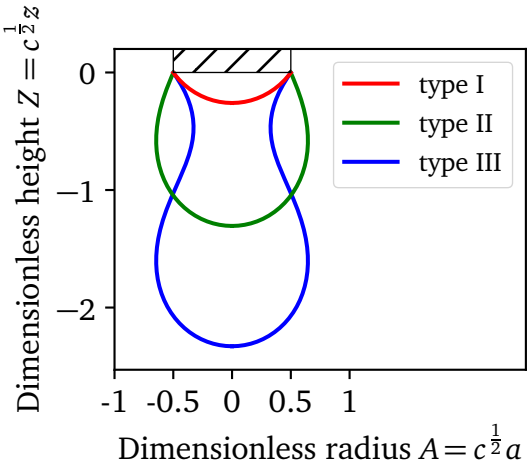

Figure 2.4: Types of pendant droplets at the tip of a capillary with radius a. Droplet shapes are integrated with parameters $a = 0.5c^{-\frac{1}{2}}$, $b = 0.6c^{-\frac{1}{2}}$. Type I: droplet without equator nor neck; type II: droplet with equator and without neck; type III: droplet with equator and neck.

The semi-analytical results can be used to provide initial conditions for numerical simulations involving axisymmetric droplets initially at rest. The benefit of this method of initialisation are two-fold. Firstly, simulating the droplet generation process may be avoided, thus reducing computational costs. Secondly, by providing initial conditions corresponding to the equilibrium shape, initial transient oscillations of droplets are suppressed and do not interfere with the dynamics of interest.

2.2.2 Oscillation Modes of Free and Sessile Droplets

The mechanical modes of isolated droplets can be calculated in the limiting case of small deformations. The analysis of these modes can be used to evaluate the damping constants of different oscillation modes and therefore their influence in transient dynamics.

As shown in [59], the shape of the droplet interface can be described by the means of spherical harmonics. For axisymmetric oscillations, the shape of a droplet can be expanded in zonal harmonics as

$$R(\theta,t) = R_0 + \sum_{n=2}^{n_{\max}} a_n(t) P_n(\cos\theta), \tag{2.62}$$

where (R,θ) are the spherical polar coordinates and P_n legendre polynomials.

For sufficiently small viscosity, the $a_n(t)$ are independent and take the form [108, 121]

$$a_n(t) = a_n(0)\cos(\omega_n t)\exp(-\frac{t}{\tau_n}), \tag{2.63}$$

$$\omega_n^2 = \frac{(n-1)n(n+1)(n+2)}{(n+1)\rho_\mathrm{i} + n\rho_\mathrm{o}}\frac{\gamma}{R_0^3}, \tag{2.64}$$

$$\tau_n = \frac{[(n+1)\rho_\mathrm{i} + n\rho_\mathrm{o}]R_0^2}{(n-1)(n+1)(2n+1)\mu_\mathrm{i} + n(n+2)(2n+1)\mu_\mathrm{o}}, \tag{2.65}$$

where ρ_i, ρ_o are the densities of the inner and outer fluid, respectively, μ_i and μ_o their dynamic viscosities, γ the surface tension and R_0 the bubble or drop radius.

For a liquid droplet immersed in a gas such that $\rho_\mathrm{l} \gg \rho_\mathrm{g}$ and $\mu_\mathrm{l} \gg \mu_\mathrm{g}$, (2.64) and (2.65) reduce to

$$\omega_n^2 = \frac{(n-1)n(n+2)}{\rho_\mathrm{l}}\frac{\gamma}{R_0^3}, \tag{2.66}$$

$$\tau_n = \frac{\rho_\mathrm{l} R_0^2}{(n-1)(2n+1)\mu_\mathrm{l}}. \tag{2.67}$$

In the case of sessile droplets, the constraint imposed by the substrate plane breaks the assumptions leading to (2.66). This case has been studied numerically in [6, 7, 86, 108, 121]. In [108], the constraint imposed by a substrate is reported to introduce a low frequency mode not present for free drops, while higher order modes are shifted to higher frequencies. In [28], the modes of hemispherical sessile drops, both with and without contact line hysteresis are considered. In the absence of contact line hysteresis, the modes of the drops were found to approach the even modes of free droplets. However, the presence of contact line hysteresis introduced a non-trivial shift of resonance frequencies.

By considering standing wave states at the surface of the droplet, a formula giving the frequency of the n^{th} oscillation mode of a droplet as a function of its mass m and contact angle θ can be derived [99]:

$$f_n = \alpha \frac{\pi}{2} \left(\frac{n^3 \gamma}{24m} \frac{\cos^3\theta - 3\cos\theta + 2}{\theta^3} \right)^{\frac{1}{2}}, \tag{2.68}$$

where $\alpha \approx 0.81$ is an experimentally fitted scaling factor. In [116], it was further found that droplet elongation leads to superposition of modes obtained from the length of the free surface in the different directions. In the case of forced oscillations, azimuthally degenerate modes oscillate with half the frequency of the forcing motion [13, 14].

The oscillations of sessile drops are thus essentially modal, with resonance frequencies following similar trends as for free droplets. However, due to the effects discussed above, the presence of the substrate may lead to slight shifts in the resonance frequencies of oscillations modes. In the case of droplets oscillations forced by external electric fields, complex dynamics may arise, both from purely electrodynamic effects and from contact line hysteresis effects.

2.2.3 Electric Fields at Dielectric and Conductive Wedges

Due to hysteretic effects, the contact line of oscillating droplets forced by electric fields plays a significant in the dynamics of the droplets. In addition, the electric stress on the insulator surface is maximal along the contact line of droplets. In many configurations of materials, the electric field at the contact line is singular. The existence of electric field singularities at contact lines between multiple materials can be studied analytically by considering a two-dimensional wedge where multiple media meet [8, 10, 70, 73, 79, 109], as shown in Fig. 2.5.

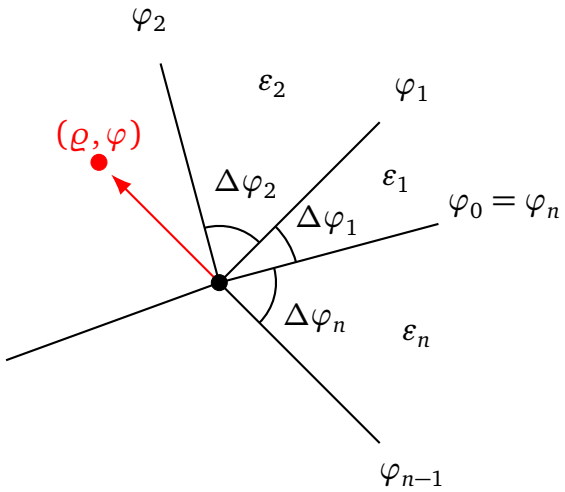

Figure 2.5: Wedge configuration where multiple media with different permittivities meet.

Consider first, for simplicity the solution of an electrostatic field problem. The electric potential $\Phi(\varrho, \varphi)$ is a solution of Laplace's equation in each of the materials

$$\Delta\Phi = 0 \iff \varrho^2 \frac{\partial^2 \Phi}{\partial \varrho^2} + \varrho \frac{\partial \Phi}{\partial \varrho} + \frac{\partial^2 \Phi}{\partial \varphi^2} = 0\,. \tag{2.69}$$

Since Laplace's equation is separable for the polar coordinate system, Φ can be rewritten as $\Phi(\varrho, \varphi) = f(\varrho)g(\varphi)$. Thus, (2.69) becomes

$$\frac{1}{f(\varrho)}\left(\varrho^2 \frac{\partial^2 f(\varrho)}{\partial \varrho^2} + \varrho \frac{\partial f(\varrho)}{\partial \varrho}\right) + \frac{1}{g(\varphi)} \frac{\partial^2 g(\varphi)}{\partial \varphi^2} = 0\,. \tag{2.70}$$

As each of its terms depends only on one of the coordinates, (2.70) can be further separated in a system of two equations

$$\begin{cases} \varrho^2 \dfrac{\partial^2 f}{\partial \varrho^2} + \varrho \dfrac{\partial f}{\partial \varrho} & -m^2 f = 0\,, \\ \dfrac{\partial^2 g}{\partial \varphi^2} & +m^2 g = 0\,, \end{cases} \tag{2.71}$$

where $m^2 \in \mathbb{R}$ is a constant. Solutions of the system (2.71) are of the form:

$$\Phi(\varrho, \varphi) = f_m(\varrho) g_m(\varphi)\,, \tag{2.72}$$

$$f_m(\varrho) = \begin{cases} c_{0,1} + c_{0,2} \ln(\varrho) & , m = 0 \\ c_{m,1} \varrho^m + c_{m,2} \varrho^{-m} & , m^2 > 0 \\ c_{m,1} \cos(m \ln(\varrho)) + c_{m,2} \sin(m \ln(\varrho)) & , m^2 < 0 \end{cases} \tag{2.73}$$

$$g_m(\varphi) = \begin{cases} c_{0,3} + c_{0,4}\varphi & , m = 0 \\ c_{m,3} \cos(m\varphi) + c_{m,4} \sin(m\varphi) & , m^2 > 0 \\ c_{m,3} \exp(m\varphi) + c_{m,4} \exp(-m\varphi) & , m^2 < 0 \end{cases} \tag{2.74}$$

The set of admissible values for m can be reduced by requiring that the energy in the domain remain finite. Thus, the electric field $\mathbf{E} = -\nabla\Phi$ must be square integrable in the vicinity of the wedge [10]. The admissible, non-constant solutions therefore have the form

$$f_m(\varrho) = \varrho^m \tag{2.75}$$

$$g_m(\varphi) = c_{m,1} \cos(m\varphi) + c_{m,2} \sin(m\varphi) \tag{2.76}$$

with $m > 0$. The corresponding electric fields are

$$\mathbf{E}_m(\varrho, \varphi) = m\varrho^{m-1} \left[\left(c_{m,1} \cos(m\varphi) + c_{m,2} \sin(m\varphi) \right) \mathbf{u}_\varrho + \left(c_{m,1} \sin(m\varphi) - c_{m,2} \cos(m\varphi) \right) \mathbf{u}_\varphi \right], \tag{2.77}$$

where $\mathbf{u}_\varrho$ and $\mathbf{u}_\varphi$ are the unitary vectors of the polar coordinate system.

In order to obtain solutions of the Laplace equation, the boundaries between materials must be taken into account. Denoting the electric potential in each material with the correspond superscript i, the continuity conditions for the electric potential and electric displacement are

$$\Phi^{i-1}(\varrho, \varphi_i) = \Phi^i(\varrho, \varphi_i), \tag{2.78}$$

$$\varepsilon_{i-1} \left.\frac{\partial \Phi^{i-1}(\varrho, \varphi)}{\partial \varphi}\right|_{\varphi=\varphi_i} = \varepsilon_i \left.\frac{\partial \Phi^{i}(\varrho, \varphi)}{\partial \varphi}\right|_{\varphi=\varphi_i}. \tag{2.79}$$

Exploiting the linear independence of the ϱ^m functions, the continuity conditions (2.78) and (2.79) can be fulfilled only by solutions with an identical parameter m. Therefore, only the functions $g_m^i(\varphi)$ need to fulfil the continuity equations:

$$g_m^i(\varphi_i) = g_m^{i+1}(\varphi_i), \tag{2.80}$$

$$\varepsilon_i \frac{\partial g_m^i}{\partial \varphi}(\varphi_i) = \varepsilon_{i+1} \frac{\partial g_m^{i+1}}{\partial \varphi}(\varphi_i). \tag{2.81}$$

Each of the n continuity conditions is characterised by a vector $\mathbf{C}_m^i$ defined as

$$\mathbf{C}_m^i = \begin{pmatrix} g_m^i(\varphi_i) \\ \varepsilon_i \frac{\partial g_m^i}{\partial \varphi}(\varphi_i) \end{pmatrix}. \tag{2.82}$$

Denoting $\mathbf{M}_m^i(\varphi)$ the matrices

$$\mathbf{M}_m^i(\varphi) = \begin{pmatrix} \cos(m\varphi) & \sin(m\varphi) \\ -m\varepsilon_i \sin(m\varphi) & m\varepsilon_i \cos(m\varphi) \end{pmatrix}, \tag{2.83}$$

the continuity equations can be written as

$$\mathbf{C}_m^i = \mathbf{M}_m^i(\varphi_i) \begin{pmatrix} c_{m,1}^i \\ c_{m,2}^i \end{pmatrix} = \mathbf{M}_{i+1}(\varphi_i) \begin{pmatrix} c_{m,1}^{i+1} \\ c_{m,2}^{i+1} \end{pmatrix}. \tag{2.84}$$

The matrices $\mathbf{M}_m^i(\varphi)$ have determinants $\det(\mathbf{M}_m^i(\varphi)) = m\varepsilon_i > 0$ and are thus invertible.

By noticing that

$$\mathbf{C}_m^{i-1} = \mathbf{M}_m^i(\varphi_{i-1}) \begin{pmatrix} c_{m,1}^i \\ c_{m,2}^i \end{pmatrix} \iff \begin{pmatrix} c_{m,1}^i \\ c_{m,2}^i \end{pmatrix} = \mathbf{M}_m^i(\varphi_{i-1})^{-1} \mathbf{C}_m^{i-1} \tag{2.85}$$

a relation between $\mathbf{C}_m^i$ and $\mathbf{C}_m^{i-1}$ can be established as

$$\mathbf{C}_m^i = \mathbf{M}_m^i(\varphi_i)\mathbf{M}_m^i(\varphi_{i-1})^{-1}\mathbf{C}_m^{i-1}\,. \tag{2.86}$$

The products $\mathbf{M}_m^i(\varphi_i)\mathbf{M}_m^i(\varphi_{i-1})^{-1}$ only depend on the wedge angles $\Delta\varphi_i$ and define transitions matrices $\mathbf{T}_m^i(\Delta\varphi_i)$:

$$\mathbf{T}_m^i(\Delta\varphi_i) = \mathbf{M}_m^i(\varphi_i)\mathbf{M}_m^i(\varphi_{i-1})^{-1} = \begin{pmatrix} \cos(m\Delta\varphi_i) & -\frac{\sin(m\Delta\varphi_i)}{m\varepsilon_i} \\ m\varepsilon_i \sin(m\Delta\varphi_i) & \cos(m\Delta\varphi_i) \end{pmatrix}. \tag{2.87}$$

Using the recursion formula (2.86) yields

$$\mathbf{C}_m^0 = \mathbf{C}_m^n = \mathbf{T}_m^n(\Delta\varphi_n)\mathbf{T}_m^{n-1}(\Delta\varphi_{n-1})\ldots\mathbf{T}_m^1(\Delta\varphi_1)\mathbf{C}_m^0\,. \tag{2.88}$$

A homogeneous system of equations

$$(\mathbf{T}_m^n(\Delta\varphi_n)\mathbf{T}_m^{n-1}(\Delta\varphi_{n-1})\ldots\mathbf{T}_m^1(\Delta\varphi_1) - \mathbf{I})\mathbf{C}_m^0 = 0 \tag{2.89}$$

is thus obtained. Non-trivial solutions exists only when

$$\det(\mathbf{T}_m^n(\Delta\varphi_n)\mathbf{T}_m^{n-1}(\Delta\varphi_{n-1})\ldots\mathbf{T}_m^1(\Delta\varphi_1) - \mathbf{I}) = 0\,. \tag{2.90}$$

For a given set of wedge angles and electric permittivities, a transcendental equation on m is obtained, thus defining admissible values for m. Admissible values of m smaller than 1 correspond to singular electric fields patterns. In the following, such values are referred to as singularity index.

Singularity index for the water droplet

The procedure described above is used in this section to characterise the case of a water droplet in the electroquasistatic approximation, as shown in Fig. 2.6. When considering the water droplet as a perfect dielectric, the procedure directly applies. However, since even distilled water exhibits a significant conductivity, conduction must also be considered. In the case of AC excitation, the effect of conductivity can be taken into account by performing the substitution $\varepsilon_\mathrm{w} \to \underline{\varepsilon}_\mathrm{w} = \varepsilon_\mathrm{w} + \frac{\kappa}{j\omega}$.

Equation (2.90) reduces to the transcendental equation

$$\sin^2(m\pi) + \frac{(\varepsilon_\mathrm{w}-\varepsilon_\mathrm{a})(\varepsilon_\mathrm{s}-\varepsilon_\mathrm{w})}{(\varepsilon_\mathrm{a}+\varepsilon_\mathrm{w})(\varepsilon_\mathrm{s}+\varepsilon_\mathrm{w})}\sin^2(m(\pi-\theta)) + \frac{(\varepsilon_\mathrm{s}-\varepsilon_\mathrm{a})(\varepsilon_\mathrm{a}-\varepsilon_\mathrm{w})}{(\varepsilon_\mathrm{s}+\varepsilon_\mathrm{a})(\varepsilon_\mathrm{a}+\varepsilon_\mathrm{w})}\sin^2(m\theta) = 0\,. \tag{2.91}$$

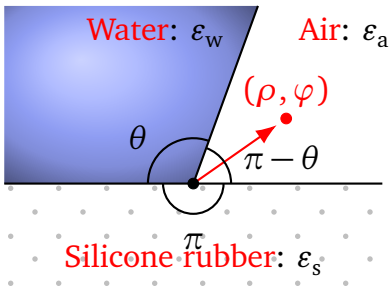

Figure 2.6: Wedge configuration for a dielectric droplet.

A similar equation involving the complex permittivity gives the solutions for the leaky dielectric case:

$$\sin^2(m\pi) + \frac{(\varepsilon_w + \frac{\kappa}{j\omega} - \varepsilon_a)(\varepsilon_s - \varepsilon_w + \frac{\kappa}{j\omega})}{(\varepsilon_a + \varepsilon_w + \frac{\kappa}{j\omega})(\varepsilon_s + \varepsilon_w + \frac{\kappa}{j\omega})} \sin^2(m(\pi - \theta)) + \frac{(\varepsilon_s - \varepsilon_a)(\varepsilon_a - \varepsilon_w - \frac{\kappa}{j\omega})}{(\varepsilon_s + \varepsilon_a)(\varepsilon_a + \varepsilon_w + \frac{\kappa}{j\omega})} \sin^2(m\theta) = 0\,. \tag{2.92}$$

In the case of the perfect conductor, the equation

$$\sin(m\pi)\cos(m(\pi - \theta)) + \frac{\varepsilon_s}{\varepsilon_a} \sin(m(\pi - \theta))\cos(m\pi) = 0 \tag{2.93}$$

gives admissible indices for the solution of Laplace's equation.

The typical case of droplet oscillations considered in Chapter 5 employs $\omega = 2\pi \cdot 27\,\mathrm{Hz}$; this choice is therefore natural for the frequency of the excitation. For distilled water, the conductivity is $\kappa = 5.5\,\mu\mathrm{S\,m^{-1}}$; it can become several orders of magnitude larger when dissolved impurities are involved. This typically results in nearly instantaneous charge dynamics, compared to the time scale of fluid motion. Numerically obtained solutions of (2.91) and (2.93) are shown in Fig. 2.7 in function of the contact angle θ. For all contact angle values, one singular solution, $m < 1$, is found. Thus, for the three models considered, singular fields can exist for all contact angle values. In the pure dielectric case, the strongest singularity observed is $m \approx 0.572$, for all substrate permittivities. In the conductive cases, however, the singularity strength can reach values close to $m = 0.5$ for all substrate permittivities. Additionally, the finite conductivity and perfect conductor cases have indistinguishable singularity indices for nearly all contact angles. The only discrepancy exists in the close vicinity of $\theta = 0$, where the singularity strength diminishes for finite conductivity, but reaches its lowest value $m = 0.5$ at $\theta = 0$ for perfect conductors.

The strength of singularities in conductive cases worsens with decreasing contact angle. The permittivity of the substrate also increases the strength of singularities for all contact angle values. The effect is more pronounced for large contact angle values. Thus, an appropriate choice of substrate properties, permittivity and wettability, can be a factor for the reduction of the electric field enhancement at contact lines, and therefore of partial discharge inception in the vicinity of the contact line.

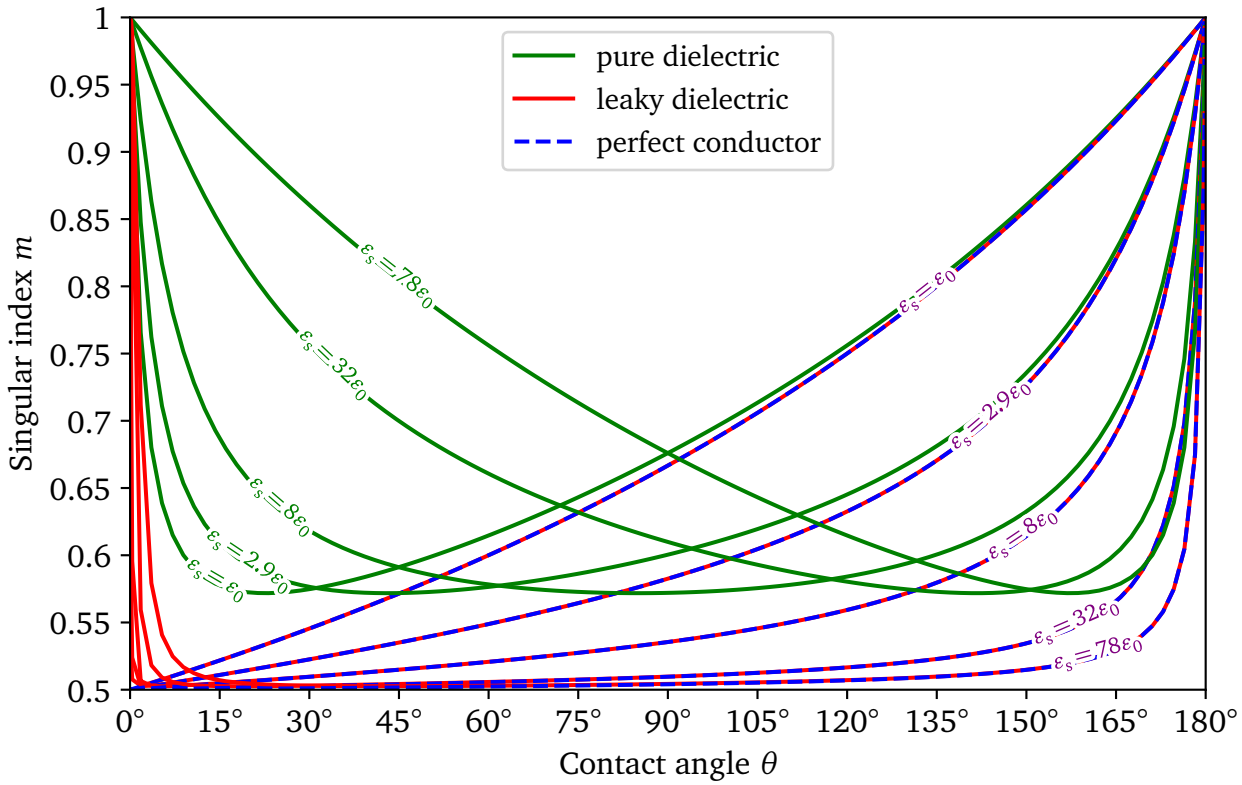

Figure 2.7: Singularity index m in function of the contact angle for different conductivity models for water and different insulator permittivities ε_s. Lower values of m indicate stronger singularities. The curves for the perfect conductor and leaky dielectric cases overlap nearly perfectly for $\theta > 20°$.

.

Non-singular solutions

Solutions with $m > 1$ exist, indicating non-singular electric field configurations. The solutions $m < 5.5$ are shown in Fig. 2.8 for $\varepsilon_s = 2.9\varepsilon_0$ for the three models.

For the pure and leaky dielectric cases, the solutions are organised in branches of solutions, bounded by successive half-integer values. It can be easily shown, from expression (2.91), that for all angles of the form $\theta = \frac{p}{q}\pi$, $p, q \in \mathbb{N}$, $m = q$ is an admissible index. Furthermore, each of these points are intersections of two corresponding branches of solutions. Considering the conductivity as an increased effective permittivity [115], the structure of solution branches in the leaky dielectric case is the same as for the pure dielectric case. However, as $\frac{\kappa}{\omega} \gg \varepsilon_w$, it becomes clear that half-integer index values nearly become double solutions at $\theta = (1 - \frac{k}{n+\frac{1}{2}})\pi$, $k \in \mathbb{N}$. This becomes true in the case of infinite permittivity, resulting directly from the form of (2.91) when $\varepsilon_w \to \infty$.

For the perfectly conducting case, no branch crossing is observed. However, admissible values for the case of perfect conductivity are also near solutions for the leaky dielectric case. The discrepancy is negligible, except for extremely low contact angle values.

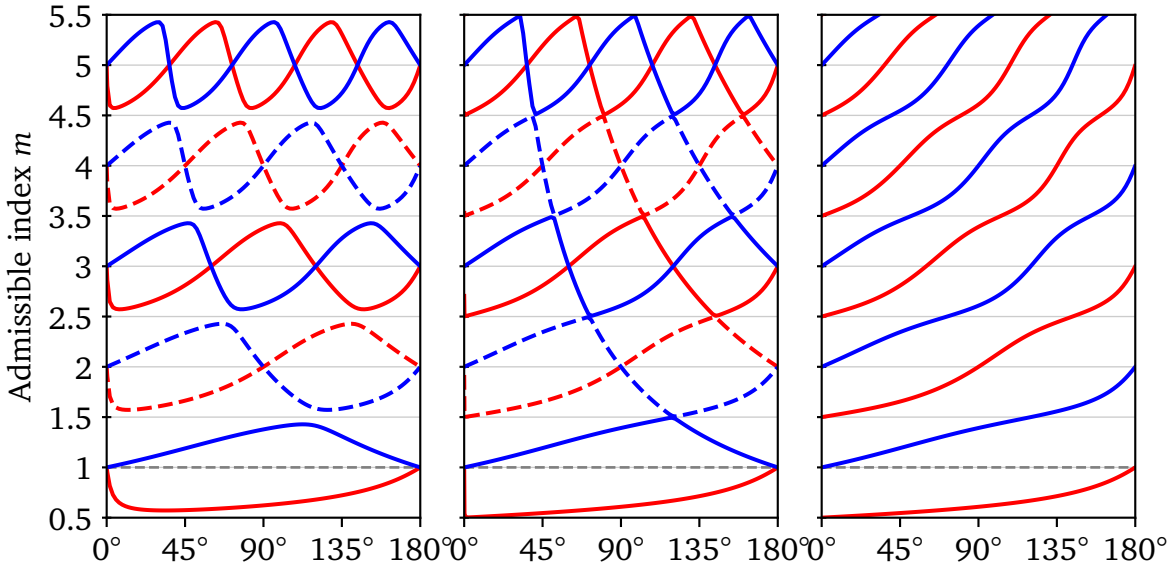

(a) Pure dielectric (b) Leaky dielectric (c) Perfect conductor

Figure 2.8: Admissible values for the parameter m in function of the contact angle for different conductivity models for water. Values $m < 1$ correspond to singular field configurations.

A mention is made in the literature of the degeneracy of the equations at branching values, giving rise to logarithmic terms [10, 51, 70]. Using the idea of confluence introduced in [51], the form of these terms can be retrieved.

Under the assumption that m_1 and m_2 are two admissible indices, converging towards m_0 at the angle value θ_0, the behaviour of the solution for the electric potential can be studied as θ goes to θ_0. The superposition of the two solutions reads

$$\begin{aligned}\Phi(\varrho,\varphi) = \varrho^{m_1}\left(A_1(m_1)\cos(m_1\varphi) + B_1(m_1)\sin(m_1\varphi)\right)\\ +\varrho^{m_2}\left(A_2(m_2)\cos(m_2\varphi) + B_2(m_2)\sin(m_2\varphi)\right),\end{aligned} \tag{2.94}$$

where the parameters A_1, B_1, A_2 and B_2 depend on θ. When these parameters tend towards finite limits, the superposition trivially tends towards a potential of the expected form for $m = m_0$. However, A_1, B_1, A_2 and B_2 may also diverge in the vicinity of θ_0, in a manner such that $A_1 + A_2$ and $B_1 + B_2$ remain bounded. Thus, when

$$A_1(m_1) \underset{\theta\to\theta_0}{\approx} A_1^* + \frac{1}{2}\cdot\frac{C^*}{m_1 - m_0}, \tag{2.95}$$

$$B_1(m_1) \underset{\theta\to\theta_0}{\approx} B_1^* + \frac{1}{2}\cdot\frac{D^*}{m_1 - m_0}, \tag{2.96}$$

$$A_2(m_2) \underset{\theta\to\theta_0}{\approx} A_2^* + \frac{1}{2}\cdot\frac{C^*}{m_2 - m_0}, \tag{2.97}$$

$$B_2(m_2) \underset{\theta\to\theta_0}{\approx} B_2^* + \frac{1}{2}\cdot\frac{D^*}{m_2 - m_0}, \tag{2.98}$$

where A^*, B^*, C_1, C_2, D_1 and D_2 are finite constants, (2.94) takes the form

$$\begin{aligned}\Phi(\varrho,\varphi) = A_1^*\varrho^{m_1}\cos(m_1\varphi) + A_2^*\varrho^{m_2}\cos(m_2\varphi) + B_1^*\varrho^{m_1}\sin(m_1\varphi) + B_2^*\varrho^{m_2}\sin(m_2\varphi) \\ + \frac{C^*}{m_1-m_2}\left(\varrho^{m_1}\cos(m_1\varphi) - \varrho^{m_2}\cos(m_2\varphi)\right) \\ + \frac{D^*}{m_1-m_2}\left(\varrho^{m_1}\sin(m_1\varphi) - \varrho^{m_2}\sin(m_2\varphi)\right).\end{aligned} \tag{2.99}$$

Taking the limit yields

$$\begin{aligned}\Phi(\varrho,\varphi) \underset{\theta\to\theta_0}{\to} (A_1^* + A_2^*)\varrho^{m_0}\cos(m_0\varphi) + (B_1^* + B_2^*)\varrho^{m_0}\sin(m_0\varphi) \\ + C^*\left.\frac{\partial(\varrho^m\cos(m\varphi))}{\partial m}\right|_{m=m_0} + D^*\left.\frac{\partial(\varrho^m\sin(m\varphi))}{\partial m}\right|_{m=m_0}.\end{aligned} \tag{2.100}$$

Hence, the potential at $m = m_0$ takes the form

$$\begin{aligned}\Phi(\varrho,\varphi) = A_0\varrho^{m_0}\cos(m_0\varphi) + B_0\varrho^{m_0}\sin(m_0\varphi) + \varrho^{m_0}(D_0\varphi\cos(m_0\varphi) - C_0\varphi\sin(m_0\varphi)) \\ + \varrho^{m_0}\ln\varrho\,(C_0\cos(m_0\varphi) + D_0\sin(m_0\varphi))\end{aligned} \tag{2.101}$$

The additional terms in (2.101) are in non-separable form and, thus, did not appear in the derivation above. The corresponding electric field exhibits terms in ϱ^{m_0-1} and $\varrho^{m_0-1}\ln(\varrho)$. In the case $m_0 = 1$, the possibility of a logarithmic singularity for the electric field is thus retrieved. For larger values of m_0, the factor ϱ^{m_0-1} dominates. The logarithmic term is not indicative of a logarithmic singularity in those cases.

3 Numerical Methods

In order to solve the coupled flow problem described in Section 2.1.4, a numerical method must be chosen. In computational fluid dynamics, two commonly employed methods are the Finite Element Method (FEM) and the Finite Volume Method (FVM). Both methods discretise the partial differential equations on a computational mesh.

The main challenge in the simulation of multiphase flow lies in the sharp interface formed by the boundary between fluids. One of the solutions to represent the interface is to conform the computational mesh to the interface [119]. The main advantage of this approach is that the boundary between the two phases is accurately described, and so can be discontinuities of quantities across the interface. Electrohydrodynamic simulations of water droplet oscillations subjected to AC fields were performed using this method in [103]. The FEM was used in this work to solve the electrodynamic problem on a moving mesh of curved elements conforming to the water-air interface. One large drawback of this method, however, is that large grid deformations may lead to reduced element quality or even singular grids, requiring remeshing. While remeshing to handle topology changes is possible in principle [87], doing so is rather computationally costly. The approach used in [103] is therefore disadvantageous for the simulation of processes involving large interface deformations and topology changes. This becomes especially true when considering atomisation processes.

In this work, numerical simulations are performed on static meshes[1] on which the interface is indirectly represented. In order to identify the fluid-fluid interface on such meshes, two main families of methods are commonly used: interface tracking methods and interface capturing methods. In interface tracking methods, the interface is explicitly tracked. The Marker and Cell method [16, 47] uses a set of massless markers in the bulk of one fluid or at the interface, which are passively advected with the fluids to provide an updated fluid front. In the Front Tracking method [120], the interface is directly tracked using an additional unstructured grid moving through the grid used for the solution of the fluid flow equations. Interface capturing methods are characterised by implicit tracking of the interface, by defining a colour function in the domain, associated with a transport equation. The advantage of these approaches is that the interface can be evolved in time without being explicitly reconstructed. In practice, many implementations perform local reconstruction of the interface in order to calculate derived quantities, e.g. the interface curvature.

A commonly used interface capturing method is the Level Set method [81]. In this method, the chosen colour function is the distance to the interface, taking negative values in one of the

[1] In the sense that the points defining the mesh are not moved to adapt to the interface.

fluids, positive values in the other, and therefore defining the interface as its zero isosurface. The colour function is transported with the fluid mixture at each time step, providing an update for the shape of the interface. The main advantage of the method is the accuracy of its representation of the curvature of the interface. However, the transport of the colour function does not ensure mass conservation. This may result in loss of mass over the duration of the simulation. The method is therefore not appropriate for simulations over a large number of time steps without modifications.

Another commonly used method is the Volume of Fluid (VoF) method [48]. In the VoF method, the colour function is the volume fraction, denoted α, of a chosen fluid, usually the denser phase. Similarly to the Level Set method, the volume fraction α is evolved in time by solving a transport equation. As the volume fraction is, by definition, bounded, a donor-acceptor scheme is used to solve the transport equation, which ensures mass conservation.

In this work, motivated by its mass conservation properties and robustness with respect to topology changes, the VoF method is used as detailed in Section 3.3.1. The implemented solver is based on the `interFoam` solver for multiphase flow of the `OpenFOAM` library [80].

3.1 Finite Volume Discretisation

3.1.1 Spatial Discretisation

In a first step, the computational domain is decomposed in a set of non-overlapping control volumes, referred to as cells, bounded by plane faces. For a given cell, the primary variables are computed at its centroid $\mathbf{C}$, defined by integration over the control volume V_P it delimits:

$$\mathbf{C} = \frac{1}{V_\mathrm{P}} \int_{V_\mathrm{P}} \mathbf{r} \mathrm{d}V \,. \tag{3.1}$$

Each face f of the computational domain is shared by at most two cells: faces at the boundary of the computational domain are used by one cell, while internal faces delimit two cells. Additional properties required for the numerical solution may be defined at the centroid $\mathbf{C}_f$ of cell faces defined similarly as for cell centroids:

$$\mathbf{C}_f = \int_{S_f} \mathbf{r} \mathrm{d}S \,. \tag{3.2}$$

Face area vectors $\mathbf{S}_f$ are vectors normal to faces with a magnitude equal to their area. The face area vectors and centroids for a given cell are sketched in Fig. 3.1. By convention, face area vectors point outwards, towards a neighbouring cell denoted N. Finally, $\mathbf{d}_f$ denotes the vector between the centroids P and N.

In the FVM, primary unknown quantities are located at cell centres. The coupling between these unknown quantities is realised by the means of fluxes associated to face centres. The spatial discretisation of the FVM allows for arbitrary unstructured meshes; no restriction is imposed on the number of faces for each control volume, providing flexibility for the mesh generation process.

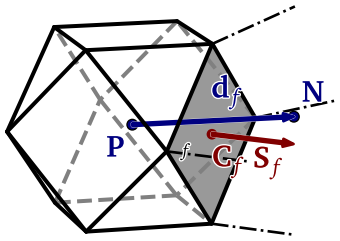

Figure 3.1: Main geometrical properties defined by the spatial discretisation of the computational domain. Two cells of arbitrary shapes are separated by a face f. Primary quantities are defined at cell centres P and N; secondary quantities may be defined at face centres $\mathbf{C}_f$.

3.1.2 Discretisation of the PDE

The volume integral of an arbitrary quantity ϕ over a control volume V_P is approximated from its value at the cell centre as:

$$\int_{V_\mathrm{P}} \phi \,\mathrm{d}V \approx \phi_\mathrm{P} V_\mathrm{P}\,, \tag{3.3}$$

where ϕ_P denotes the value of ϕ at the cell centre P. This approximation is exact for quantities varying linearly in the control volume, and is second-order accurate otherwise. The surface integral over the boundary ∂V_P of a control volume is similarly approximated from its values ϕ_f at face centres:

$$\int_{\partial V_\mathrm{P}} \phi \,\mathrm{d}S = \sum_f \int_f \mathrm{d}S\phi \approx \sum_f S_f \phi_f\,. \tag{3.4}$$

Volume integrals of differential operators in Partial Differential Equations (PDEs) are transformed to surface integrals using Gauss's theorem. For a scalar quantity ϕ and for a vectorial quantity $\boldsymbol{\chi}$, the volume integrals become:

$$\int_{V_\mathrm{P}} \nabla\phi \,\mathrm{d}V = \int_{\partial V_\mathrm{P}} \phi \,\mathrm{d}\mathbf{S}\,, \tag{3.5}$$

$$\int_{V_\mathrm{P}} \nabla\cdot\boldsymbol{\chi} \,\mathrm{d}V = \int_{\partial V_\mathrm{P}} \mathrm{d}\mathbf{S}\cdot\boldsymbol{\chi}\,. \tag{3.6}$$

For the solution of the problem at hand, the terms that need to be treated using this method are diffusion, convection, divergence and gradient terms.

Gradient terms

For a scalar or vector ψ, the gradient is integrated over a control volume V_P as

$$\int_{V_\mathrm{P}} \nabla\psi \mathrm{d}V = \int_{\partial V_\mathrm{P}} \mathrm{d}\mathbf{S}\psi \approx \sum_f \mathbf{S}_f \psi_f \,. \tag{3.7a}$$

When the face centred values ψ_f of ψ are known, the sum is directly evaluated. Otherwise, interpolation is used to obtain the ψ_f from cell centred values.

The cell centred gradient $(\nabla\psi)_P$ is often used as an intermediate quantity. It can be approximated as

$$(\nabla\psi)_P \approx \frac{1}{V_\mathrm{P}} \sum_f \mathbf{S}_f \psi_f \,. \tag{3.8}$$

The face centred gradient $(\nabla\psi)_f$ can be obtained by interpolation of cell centred gradients.

Diffusion terms

The diffusion term associated to a quantity ϕ and a diffusion constant Γ is discretised as

$$\int_{V_\mathrm{P}} \nabla\cdot(\Gamma\nabla\phi)\,\mathrm{d}V_\mathrm{P} = \int_{\partial V_\mathrm{P}} \mathrm{d}\mathbf{S}\cdot(\Gamma\nabla\phi) \approx \sum_f \Gamma_f \mathbf{S}_f \cdot (\nabla\phi)_f \,. \tag{3.9}$$

The diffusion flux normal to the face f, $\mathbf{S}_f \cdot (\nabla\phi)_f$, is evaluated from the values ϕ_P and ϕ_N of ϕ at the centre of adjacent faces. For orthogonal meshes, i.e. when $\mathbf{S}_f$ and $\mathbf{d}_f$ are colinear, $\mathbf{S}_f \cdot (\nabla\phi)_f$ is approximated as

$$\mathbf{S}_f \cdot (\nabla\phi)_f \approx ||\mathbf{S}_f|| \frac{\phi_\mathrm{N} - \phi_\mathrm{P}}{||\mathbf{d}_f||} \,. \tag{3.10}$$

For non-orthogonal meshes, $\mathbf{S}_f \cdot (\nabla\phi)_f$ is split as

$$\mathbf{S}_f \cdot (\nabla\phi)_f = \boldsymbol{\Delta} \cdot (\nabla\phi)_f + \mathbf{k} \cdot (\nabla\phi)_f \,, \tag{3.11}$$

where the vectors $\boldsymbol{\Delta}$ and $\mathbf{k}$ satisfy $\mathbf{S}_f = \boldsymbol{\Delta} + \mathbf{k}$ and $\boldsymbol{\Delta} \parallel \mathbf{S}_f$. The orthogonal contribution $\boldsymbol{\Delta}\cdot(\nabla\phi)_f$ is treated implicitly, while $\mathbf{k}\cdot(\nabla\phi)_f$ defines an explicit non-orthogonal correction. A typical scheme for the evaluation of $\mathbf{S}_f \cdot (\nabla\phi)_f$, obtained by imposing $\boldsymbol{\Delta} \perp \mathbf{k}$, is

$$\mathbf{S}_f \cdot (\nabla\phi)_f \approx ||\mathbf{S}_f|| \left[\frac{\phi_\mathrm{N} - \phi_\mathrm{P}}{\mathbf{d}_f \cdot \mathbf{n}_f} + \left(\mathbf{n}_f - \frac{\mathbf{d}_f}{\mathbf{d}_f \cdot \mathbf{n}_f} \right) \cdot (\nabla\phi)_f \right] , \tag{3.12}$$

where $\mathbf{n}_f = \frac{\mathbf{S}_f}{||\mathbf{S}_f||}$ is the face normal vector. In (3.12), the face gradient term $(\nabla\phi)_f$ is interpolated from the cell centred gradient calculated using (3.8). Other possible decompositions of $\mathbf{S}_f \cdot (\nabla\phi)_f$ are given in [53].

Divergence terms

For a vector or tensor $\boldsymbol{\chi}$, the divergence is integrated as

$$\int_{V_\mathrm{P}} \nabla \cdot \boldsymbol{\chi} \, \mathrm{d}V_\mathrm{P} = \int_{\partial V_\mathrm{P}} \mathrm{d}\mathbf{S} \cdot \boldsymbol{\chi} \approx \sum_f \mathbf{S}_f \cdot \boldsymbol{\chi}_f \,. \tag{3.13a}$$

Similarly to gradient terms, interpolation is performed to obtain the $\boldsymbol{\chi}_f$ if needed, before the summation.

Convection terms

For a scalar quantity ϕ and a given vector field $\boldsymbol{\chi}$ the convection term $\nabla\cdot(\boldsymbol{\chi}\,\phi)$ is approximated as

$$\int_{V_\mathrm{P}} \nabla \cdot (\boldsymbol{\chi}\phi) = \int_{\partial V_\mathrm{P}} \mathrm{d}\boldsymbol{S} \cdot (\boldsymbol{\chi}\phi) \approx \sum_f \mathbf{S}_f \cdot \boldsymbol{\chi}_f \phi_f \,. \tag{3.14a}$$

The field of interest ϕ_f is located at face centres and therefore needs to be evaluated from cell centred values. A variety of schemes can be used, with different properties.

For a given face f, linear interpolation (CDS) approximates the values at the two neighbouring cells P and N:

$$\phi_f = f_x \phi_\mathrm{P} + (1 - f_x)\phi_\mathrm{N} \,. \tag{3.15}$$

where the interpolation factor $f_x = \frac{f\bar{\mathrm{N}}}{\mathrm{P}\bar{\mathrm{N}}} = \frac{||\mathbf{C}_f - \mathbf{C}_\mathrm{N}||}{||\mathbf{d}_f||}$ is the ratio between the distance from the face to the centre of cell N and the distance between the centres of cells P and N. The CDS is second order accurate in space but leads to an unbounded scheme (cf. [34] for more details).

Upwind interpolation (UDS) extracts the value of ϕ in the upwind direction, i.e. in the direction opposite to the vector $\boldsymbol{\chi}$.

$$\phi_f = \begin{cases} \phi_\mathrm{P} & \text{for } (\mathbf{C}_\mathrm{P} - \mathbf{C}_\mathrm{N}) \cdot \boldsymbol{\chi} \geq 0 \,, \\ \phi_\mathrm{N} & \text{otherwise} \,. \end{cases} \tag{3.16}$$

Upwinding guarantees boundedness at the expense of accuracy, as it is clearly only first-order accurate in space. It furthermore introduces numerical diffusion.

In order to increase the accuracy of the differencing scheme while guaranteeing boundedness, linear and upwind interpolation can be combined:

$$\phi_f = (1-\gamma)(\phi_f)_{UDS} + \gamma(\phi_f)_{CDS} \,. \tag{3.17}$$

The blending factor γ can be set identically for all faces or individualised for each face, thus modifying the properties of the scheme according to the problem at hand.

Boundary conditions

At boundaries of the computational domain, values of the form ϕ_f and $(\nabla\phi)_f$ need to be treated specifically. The values ϕ_b and $(\nabla\phi)_\mathrm{b} = \frac{\phi_\mathrm{b}-\phi_\mathrm{P}}{||\mathbf{C}_\mathrm{b}-\mathbf{C}_\mathrm{P}||}$ at boundaries are obtained from the boundary conditions. The general form of the boundary condition is

$$\beta\phi_\mathrm{b} + (1-\beta)(\nabla\phi)_\mathrm{b} = v_\mathrm{b}\,, \tag{3.18}$$

where v_b is a prescribed value. The parameter β controls the behaviour of the boundary condition; the values $\beta = 0$ and $\beta = 1$ represent Neumann and Dirichlet boundary conditions, respectively.

Temporal discretisation

The equations are solved for discrete time steps (t_n) separated by step sizes $\Delta t_n = t_{n+1} - t_n$. For readability reasons, the values of fields at given time instants are denoted with the time index as superscript: $\phi^n := \phi(t_n)$. Furthermore, unless otherwise specified, Δt denotes the step size of the time instant of interest, i.e. $\Delta t := \Delta t_n$.

The time derivative is integrated over a control volume and rewritten in terms of its values at different time instants.

For an arbitrary spatial operator $\mathscr{A}$, a transient equation integrates in time as:

$$\int_{t_n}^{t_{n+1}} \left[\frac{\partial}{\partial t} \int_{V_\mathrm{P}} \rho\phi \,\mathrm{d}V + \int_{V_\mathrm{P}} \mathscr{A}\phi \,\mathrm{d}V \right] \mathrm{d}t = 0 \tag{3.19}$$

The first term is approximated as

$$\int_{t_n}^{t_{n+1}} \left[\frac{\partial}{\partial t} \int_{V_\mathrm{P}} \rho\phi \,\mathrm{d}V \right] \mathrm{d}t = (\rho\phi V_\mathrm{P})^{n+1} - (\rho\phi V_\mathrm{P})^n\,. \tag{3.20}$$

Introducing the discretised form $\mathscr{A}^*$ of $\mathscr{A}$, the second term becomes:

$$\int_{t_n}^{t_{n+1}} \left[\int_{V_\mathrm{P}} \mathscr{A}\phi \,\mathrm{d}V \right] \mathrm{d}t = \int_{t_n}^{t_{n+1}} \mathscr{A}^*\phi \,\mathrm{d}t\,. \tag{3.21}$$

(3.21) can be evaluated in various manners. First, the spatial terms can be discretised implicitly, i.e. using the yet unknown values:

$$\int_{t_n}^{t_{n+1}} \mathscr{A}^*\phi \,\mathrm{d}t = \mathscr{A}^*\phi^{n+1}\Delta t\,. \tag{3.22}$$

This discretisation is first order accurate in time and unconditionally stable.

The spatial term can be discretised explicitly, i.e. using previous time step values:

$$\int_{t_n}^{t_{n+1}} \mathscr{A}^* \phi \, \mathrm{d}t = \mathscr{A}^* \phi^n \Delta t \,, \tag{3.23}$$

yielding a first order scheme.

The time discretisation scheme can also be selected using a θ–scheme, by combining implicit and explicit terms:

$$\int_{t_n}^{t_{n+1}} \mathscr{A}^* \phi \, \mathrm{d}t = \mathscr{A}^* \left(\theta \phi^{n+1} + (1-\theta) \phi^n \right) \Delta t \,. \tag{3.24}$$

Setting $\theta = 1/2$ yields the Crank-Nicolson scheme [20], which is second order accurate. In this thesis, time discretisation is performed according to (3.24), with $\theta = 0.55$, for most terms. One exception is the update of the fluid-fluid interface, for which the first order scheme (3.23) is employed.

In general, due to constraints originating from the solution schemes, a Courant-Friedrichs-Lewy (CFL) [19] type condition for each cell i of the computational mesh limits the time step size, which guarantees stability:

$$\max_i C_i = \max_i \Delta t \frac{1}{2V_i} \sum_{f \in \partial V_i} |\varphi_f| \leq C_{\max} \,, \tag{3.25}$$

where $\varphi_f = \mathbf{S}_f \cdot \mathbf{u}_f$ denotes the volumetric flux through face f. The Courant number limit $C_{\max}$ depends on the solution scheme. For an explicit solver, the typical value is $C_{\max} = 1$.

The Courant number depends on the instantaneous volumetric fluxes, so that the largest allowed time step varies during the simulation. In order to reduce computational efforts, adaptive control of the time step is desirable. When high velocities are involved in the calculations, the time step must be reduced to conform to the CFL condition. Conversely, when the maximal velocity is reduced, the time step size can be chosen larger. Consequently, introducing damping factors λ_1, λ_2 to avoid large time step variations leading to time step oscillations, the time step size is chosen as:

$$\Delta t = \min \left[\min \left(\frac{C_{\max}}{C^n}, 1 + \lambda_1 \frac{C_{\max}}{C^n}, 1 + \lambda_2 \right) \Delta t, \Delta t_{\max} \right] , \tag{3.26}$$

where C^n is the maximum Courant number observed at time step t_n. Typical values for the damping factors are $\lambda_1 = 0.1$ and $\lambda_2 = 0.2$.

Using the discretisation methods defined above, equations that need to be solved on the computational mesh can be written as a linear system of equation as $\mathbf{A}\phi = \mathbf{b}$. Such a system can be solved using an iterative solver (see e.g. [95] for more details).

3.2 Solution of the Momentum Equation

The momentum equations (2.50) and (2.51) have two free variables that need to be solved for, namely the velocity field $\mathbf{u}$ and the pressure field p. As only the gradient of the pressure field appears, in (2.51) for incompressible fluid flow, the pressure field is uniquely defined up to an additive constant. Thus, the solution is provided in terms of a relative pressure with respect to some reference pressure.

For the numerical solution of (2.51), the viscous, pressure and gravity force density terms are first rewritten. The dynamic pressure field p_d is introduced in terms of the dynamic pressure p_d as

$$p = p_\mathrm{d} + \rho \mathbf{g} \cdot \mathbf{r}\,, \tag{3.27}$$

$$\nabla p = \nabla p_\mathrm{d} + \rho \mathbf{g} + (\mathbf{g} \cdot \mathbf{r}) \nabla \rho\,. \tag{3.28}$$

Furthermore, the contribution of the viscous stress tensor is rewritten using vector identities and the incompressibility condition (2.50) as

$$\nabla \cdot \left(\mu \left(\nabla \mathbf{u} + \nabla \mathbf{u}^\mathsf{T}\right)\right) = \nabla \mu \cdot \nabla \mathbf{u} + \nabla \cdot \left[\mu \left(\nabla \mathbf{u}^\mathsf{T} - \frac{\mathrm{tr}(\nabla \mathbf{u}^\mathsf{T})}{3} \mathbb{I}\right)\right], \tag{3.29}$$

where $\mathbb{I}$ denotes the unit tensor.

Introducing the substitutions defined by (3.27) and (3.29) in (2.51) yields

$$\frac{\partial \rho \mathbf{u}}{\partial t} + \nabla \cdot (\rho \mathbf{u} \otimes \mathbf{u}) = -\nabla p_\mathrm{d} - (\mathbf{g} \cdot \mathbf{r}) \nabla \rho + \nabla \mu \cdot \nabla \mathbf{u} + \nabla \cdot \left[\mu \left(\nabla \mathbf{u}^\mathsf{T} - \frac{\mathrm{tr}(\nabla \mathbf{u}^\mathsf{T})}{3} \mathbb{I}\right)\right] + \mathbf{f}_\mathrm{s} + \mathbf{f}_\mathrm{e}\,. \tag{3.30}$$

The convective term $\nabla \cdot (\rho \mathbf{u} \otimes \mathbf{u})$ is non-linear in $\mathbf{u}$. It is linearised in the discretised form by considering the term $\rho \mathbf{u}$ as a known secondary quantity. The term $\nabla \cdot \left[\mu \left(\nabla \mathbf{u}^\mathsf{T} - \frac{\mathrm{tr}(\nabla \mathbf{u}^\mathsf{T})}{3} \mathbb{I}\right)\right]$ is discretised using already known values for $\mathbf{u}$ at time step n.

The momentum equations are solved using the Pressure-Implicit with Splitting of Operators (PISO) algorithm [52], which solves the equations using a predictor-corrector approach. Regardless of the chosen time discretisation and spatial discretisation schemes, contributions of all control volume for (3.30) can be summarised in matrix-vector form as

$$\mathbf{C} U^{n+1} = r^n - \nabla P_\mathrm{d}^{n+1} + S\,, \tag{3.31}$$

where U^{n+1} and P_d^{n+1} are the solution vectors for the velocity and dynamic pressure, $\mathbf{C}$ is the square matrix multiplying the solution vector U^{n+1}, r^n is the vector aggregating the explicit

terms of the discretisation of the momentum equation, and S denotes the source terms corresponding to external forces. The matrix $\mathbf{C}$ is split into a diagonal matrix $\mathbf{A}$ and a matrix of off-diagonal coefficients $\mathbf{H}$: $\mathbf{C} = \mathbf{A} + \mathbf{H}$.

In order to solve (3.31) for the two unknowns U^{n+1} and P_d^{n+1}, an additional condition is needed. For incompressible flows, this condition is provided by the vanishing divergence of the velocity. The PISO algorithm provides a divergence free solution for U^{n+1} by proceeding as follows.

First, a predicted velocity field U^* is determined using the known pressure distribution as

$$\mathbf{C}U^* = r - \nabla P_\mathrm{d}^n + S\,. \tag{3.32}$$

The divergence-free condition is not enforced for U^*. U^* is therefore corrected into a divergence-free velocity field by splitting of operators as

$$\mathbf{A}U^{**} + \mathbf{H}U^* = r - \nabla P_\mathrm{d}^* + S\,, \tag{3.33}$$

where U^{**} is a second corrected velocity and P_d^* a corrected pressure to be determined. The matrix $\mathbf{A}$ is diagonal, and can easily be inverted. By rearranging the terms of (3.33), U^{**} is expressed as

$$U^{**} = \mathbf{A}^{-1}\left(r - \mathbf{H}U^* - \nabla P_\mathrm{d}^* + S\right). \tag{3.34}$$

Imposing the divergence free condition on (3.34) yields

$$\nabla \cdot U^{**} = 0 = \nabla \cdot \left[\mathbf{A}^{-1}\left(r - \mathbf{H}U^* - \nabla P_\mathrm{d}^* + S\right)\right], \tag{3.35}$$

eliminating the corrected field U^{**} from the equation. The still unknown first corrected pressure P_d^* can therefore be obtained by rearranging the terms and solving the resulting Poisson equation:

$$\nabla \cdot \left(\mathbf{A}^{-1}\nabla P_\mathrm{d}^*\right) = \nabla \cdot \left[\mathbf{A}^{-1}\left(r - \mathbf{H}U^* + S\right)\right]. \tag{3.36}$$

U^{**} then results from (3.34). The computation of the second corrections for the pressure and velocity require to solve for the pressure and update the velocity field accordingly:

$$\nabla \cdot \left(\mathbf{A}^{-1}\nabla P_\mathrm{d}^{**}\right) = \nabla \cdot \left(\mathbf{A}^{-1}r - \mathbf{A}^{-1}\mathbf{H}U^{**} + \mathbf{A}^{-1}S\right), \tag{3.37}$$

$$U^{***} = \mathbf{A}^{-1}r - \mathbf{A}^{-1}\mathbf{H}U^* - \mathbf{A}^{-1}\nabla P_\mathrm{d}^{**} + \mathbf{A}^{-1}S\,. \tag{3.38}$$

Further corrections can be performed, following the same procedure, until convergence is achieved. In this work, the PISO loop is used with three corrector steps.

3.3 Interface Capturing Scheme

The discretisation and solution of the momentum equations has been introduced in Section 3.1 for a single phase flow. The treatment of the two phase interface using the VoF method is presented in the following section. The contribution of the surface tension force density $\mathbf{f}_s$ in (2.51) and the treatment of material properties in the different media are detailed.

3.3.1 Volume of Fluid (VoF) Method

The VoF method relies on the advection of a colour function defined by the volume fraction α of one of the fluids in each cell of the computational domain. In the following, it is assumed that the two fluids of interest are indexed with 1 and 2, and that α identifies the volume fraction of fluid 1. By definition, $0 \leq \alpha \leq 1$ in all cells of the computational domain. Furthermore, $\alpha = 1$ in each cell entirely filled by fluid 1 and $\alpha = 0$ in each cell filled by fluid 2. The intermediate values define a diffuse interface between the two fluids and has typically a thickness of a few cells, see Fig. 3.2.

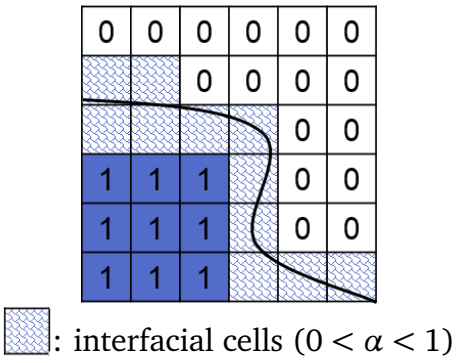

Figure 3.2: The volume fraction corresponding to a sharp interface on a computational grid.

The transport equation

$$\frac{\partial \alpha}{\partial t} + \nabla \cdot (\alpha \mathbf{u}) = 0\,, \tag{3.39}$$

with the constraint $0 \leq \alpha \leq 1$, provides a description of interface motion without need for explicit interface reconstruction. The solution of (3.39) can be performed with a donor-acceptor scheme to ensure boundedness of the volume fraction field α. In this work, the Multidimensional Universal Limiter for Explicit Solutions (MULES) [93] is used here for the solution of (3.39).

One difficulty of the VoF method is that the solution of (3.39) is prone to numerical diffusion. This is manifested by an increase of the diffuse interface thickness over the course of simulations. In order to preserve interface sharpness, (3.39) is modified by adding an artificial compressive velocity term [132], as

$$\frac{\partial \alpha}{\partial t} + \nabla \cdot (\alpha [\mathbf{u} + \mathbf{u}_c]) = 0\,, \tag{3.40}$$

where $\mathbf{u}_c$ acts only in the vicinity of the interface and in the direction normal to it.

Given a volume fraction distribution, the material properties μ and ρ of the fluids on the mesh are computed as weighted averages:

$$\mu = \alpha\mu_1 + (1-\alpha)\,\mu_2\,, \tag{3.41a}$$

$$\rho = \alpha\rho_1 + (1-\alpha)\,\rho_2\,. \tag{3.41b}$$

The two phase problem is thus reworked into a single phase problem with varying material properties across the diffuse interface.

3.3.2 Surface Tension Contribution

According to the Young-Laplace equation, the surface tension force density depends on the surface tension γ, the interface curvature $K = \left(\frac{1}{R_1} + \frac{1}{R_2}\right)$, and the interface normal $\mathbf{n}$. Typically, the discrete interface normal $\mathbf{n}_\alpha$ is calculated from the gradient of the volume fraction,

$$\mathbf{n}_\alpha = -\frac{\nabla\alpha}{||\nabla\alpha||}\,. \tag{3.42}$$

The discrete curvature K_α is derived from its divergence:

$$\left(\frac{1}{R_1} + \frac{1}{R_2}\right) \approx K_\alpha = \nabla\cdot\mathbf{n}_\alpha\,. \tag{3.43}$$

Finally, using the gradient of the volume fraction as a distribution representing the interface, the surface tension force density can be written as

$$\mathbf{f}_s = \gamma\nabla\cdot\left(\frac{\nabla\alpha}{||\nabla\alpha||}\right)\nabla\alpha\,. \tag{3.44}$$

This approach is called the Continuum Surface Force (CSF) model [9]. Under this representation, the surface force density becomes a volume force density acting only in the transition region formed by the diffuse interface. In the limit of a mesh characteristic size h approaching 0, the CSF model ensures that the surface force density is correctly represented.

One of the limitations of using the interface normal calculated as in (3.42) is the tendency to produce unphysical spurious currents tangential to the interface [37]. Numerical simulations performed in Chapters 5 and 7 are sensitive to the limitations of this approach. The isosurface-based model for curvature calculation developed by [3] is therefore adopted for these simulations. In this curvature model, the $\alpha = 0.5$ isosurface of the volume fraction is reconstructed. The normal vectors are then distributed in a stencil surrounding the fluid-fluid interface. The interface curvature is then calculated from these vectors.

3.3.3 Contact Angle Model

The calculation of the curvature requires values for both $\mathbf{n}_\alpha$ and $\nabla\alpha$ at boundaries of the computational domain. The contact angle model provides these values, by prescribing values for the contact angle θ.

The contact angle model is implemented as a condition at boundaries using the volume fraction α. With respect to α, the contact angle model prescribes a value g_b for the gradient of α at boundaries:

$$\mathbf{n}_\mathrm{b} \cdot (\nabla\alpha)_\mathrm{b} = g_\mathrm{b}\,. \tag{3.45}$$

The orientation of $\nabla\alpha$ is furthermore corrected to achieve the prescribed contact angle value with respect to the solid surface. The prescribed contact angle value is achieved when

$$\mathbf{n}_\mathrm{b} \cdot \mathbf{n}_\alpha = \cos(\theta) \tag{3.46}$$

at the boundary. Given an uncorrected estimate for the interface normal $\mathbf{n}_\alpha^*$, $\mathbf{n}_\alpha$ can be calculated as a linear combination of $\mathbf{n}_\alpha^*$ and $\mathbf{n}_\mathrm{b}$. Replacing $\nabla\alpha$ with $||\nabla\alpha||\mathbf{n}_\alpha$ implements the contact angle model at the boundary.

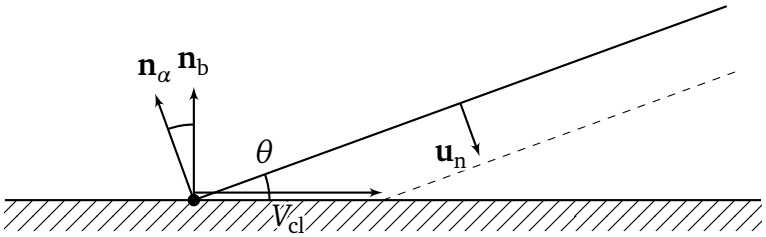

Figure 3.3: Parameters for the application of the dynamic contact angle model: contact angle θ, boundary normal $\mathbf{n}_\mathrm{b}$, interface normal $\mathbf{n}_\alpha$, normal interface velocity $\mathbf{u}_\mathrm{n}$, contact line velocity V_cl.

For dynamic contact lines, the gradient g_b at the boundary must be reevaluated when the fields (e.g. $\mathbf{u}$) prescribing the value of θ are updated. Since the velocity of the contact line is not that of a fluid particle, the velocity of the fluid close to the contact line cannot be used to evaluate contact line velocities. Instead, the contact line velocity is evaluated from the normal interface velocity, as described in [64, 92]. Using purely geometrical arguments, the contact line velocity is evaluated from the normal velocity of the interface close to the contact line,

$$V_\mathrm{cl} = \frac{\mathbf{n}_\alpha \cdot \mathbf{u}_\mathrm{n}}{\sin(\theta)} = \frac{\mathbf{n}_\alpha \cdot \mathbf{u}_P}{\sin(\theta)} = \frac{\mathbf{n}_\alpha \cdot \mathbf{u}_P}{\sqrt{1-(\mathbf{n}_\mathrm{b} \cdot \mathbf{n}_\alpha)^2}}\,, \tag{3.47}$$

where $\mathbf{u}_P$ is the velocity at the centre of cells adjacent to the boundary. When hysteretic effects are taken into account, an additional step is required to calculate the contact angle. The choice

of the model for determining the contact angle depends on whether the contact line should remain static, advancing or receding. If the current contact angle θ^n and the predicted contact line velocity V_{cl}^{n+1} indicate an advancing contact line, i.e. if $\theta^n > \theta_{\mathrm{adv}}$ and $V_{\mathrm{cl}}^{n+1} > 0$, the dynamic contact angle model (see (2.4)) applies. Idem for receding contact lines when $\theta^n < \theta_{\mathrm{rec}}$ and $V_{\mathrm{cl}}^{n+1} < 0$. In any other case, the contact line is set as static.

Implementation-wise, the contact angle model acts as a mixed boundary condition on the volume fraction α. At boundary faces where the contact line should remain static, a Dirichlet Boundary Condition (BC) is set, forcing the value of α to remain the same for the next time step. At other faces, where the dynamic contact angle model is used, the Neumann BC, (3.45), is applied.

The application of the contact angle model modifies the volume fraction field at the boundary, allowing it to change regardless of the imposition of a no-slip boundary condition. The no-slip boundary condition is therefore implicitly relaxed at the boundary, thus removing the stress singularity that would otherwise occur at the contact line.

3.4 Electroquasistatic Field Problem

Similarly to the hydrodynamic problem, the solution of the electric field problem requires a description for the interface between fluids. Conventional discretisation methods for the solution of the electric field problem rely on a sharp interface description for the boundaries between the materials involved. These methods exhibit the same limitations regarding moving interfaces as for multiphase flows. The natural approach is therefore to use the same diffuse interface representation as for the hydrodynamic problem. Consequently, the VoF method is adapted in this work for the solution of the Electroquasistatic (EQS) field problem (2.47) and (2.48).

A similar approach was described by [118] in the limiting cases of electrostatics and stationary currents. The extension to the EQS field problem was considered in [35, 66, 65], mostly for the study of charge separation and electrokinetic effects.

A common consideration in [35, 66, 65], is the choice of the averaging scheme for the electrical properties. Using the volume fraction α, an electric material property $\xi \in \{\varepsilon, \kappa\}$ is approximated within the diffuse interface either by arithmetic or harmonic averaging, as

$$\xi_{\mathrm{a}} = \alpha\xi_1 + (1-\alpha)\xi_2\,, \tag{3.48}$$

$$\frac{1}{\xi_{\mathrm{h}}} = \frac{\alpha}{\xi_1} + \frac{1-\alpha}{\xi_2}\,. \tag{3.49}$$

In [91], the numerical accuracy of these approximations was investigated. Arithmetic averaging is shown to be the more accurate choice for electric fields tangential to the interface. Conversely, harmonic averaging is more accurate for electric fields normal to the interface. Regardless of the chosen scheme, the spatial discretisation remains first order, as expected due to the inherent limitations of the diffuse interface representation.

Another factor in the choice of the averaging scheme is the ratio between material properties. For large ratios, the choice of harmonic interpolation has been shown to be more accurate, see e.g. [134]. Due to the large ratio of conductivity between different involved fluids, the harmonic interpolation scheme is chosen here. It was moreover found to produce less charge diffusion at the interface. The harmonic interpolation scheme is therefore chosen for the electrical conductivity, κ, and permittivity, ε.

The electroquasistatic problem composed of (2.47) and (2.48) is discretised in time as:

$$\nabla \cdot \left(\varepsilon^{n+1} \nabla \Phi^{n+1}\right) = -\rho_{\mathrm{e}}^{n+1}, \tag{3.50}$$

$$\frac{\rho_{\mathrm{e}}^{n+1} - \rho_{\mathrm{e}}^{n}}{\Delta t} + \nabla \cdot \left(\rho_{\mathrm{e}}^{n+\frac{1}{2}} \mathbf{u}^{n+\frac{1}{2}}\right) = \nabla \left(\kappa^{n+\frac{1}{2}} \nabla \Phi^{n+\frac{1}{2}}\right). \tag{3.51}$$

The spatial discretisation of (3.50) and (3.51) is performed using the FVM as described in Section 3.1.2. The values indexed at time n+1/2 are approximated using the θ scheme (3.25). As the charge density ρ_{e}^{n+1} is initially unknown, fixed-point iterations are used to ensure the consistency of the solution of (3.50) and (3.51). In practice, three fixed-point iterations were found sufficient to reduce initial residuals of the iterative solvers below the target threshold.

4 Coupled Electrohydrodynamic Solver

4.1 Adaptive Mesh Refinement and Load Balancing

4.1.1 Adaptive Mesh Refinement

The accuracy of a numerical simulation can be controlled by varying the mesh density. Uniformly refining a computational mesh increases accuracy, at the expense of largely increased computational costs. One way to alleviate issues of computational costs is to apply mesh refinement only in regions where additional resolution is required. In the case of multiphase electrohydrodynamic flows, the interface is typically the location where fine mesh resolution is needed. This results from the high gradients at the interface, limiting numerical convergence to the first order. Furthermore, the minimal radius of droplets and liquid threads that can be resolved by the method are limited by the cell characteristic size at the interface. Unsufficiently refined meshes result in artificially large droplets and liquid threads.

In electrospray simulations in particular, the size of generated droplets is in the micrometer range, much smaller than the size of the computational domain. In order to ensure that sufficient numerical resolution is obtained, the mesh must be refined at the interface as it moves. This can result in a large required number of degrees of freedom if performed statically. Dynamical refinement of the mesh at the interface can allow to reduce drastically the number of degrees of freedom required to resolve the interface, at the cost of additional mesh refinement operations.

In OpenFOAM, adaptive mesh refinement is available for hexahedral meshes, using an octree structure. At given timesteps, hexahedral cells needing refinement are, possibly recursively, split equally in all three directions, into eight child cells each. An octree representing successive refinement steps is associated to each cell in the base (coarse) mesh. The depth of each cell in its octree is called its level of refinement. Cells in the base mesh are also referred as level 0 cells. Child cells where no additional accuracy is needed can be coarsened by reconstructing the parent cell from the tree structure.

Quadtree refinement

OpenFOAM is a dimension agnostic library, i.e. the same code is reused for computations in one-dimensional (1D), two-dimensional (2D) and three-dimensional (3D). In order to perform two-dimensional computations, rather than reducing control volumes to control surfaces, the

computational mesh is defined with a thickness of a single cell in the invariant direction. Special boundary conditions indicate that the direction is invariant, and can therefore be ignored when assembling linear systems of equations to be solved. The same procedure is used to define axisymmetric geometries, by utilising a wedge geometry with a small opening angle and special cyclic boundary conditions in the direction of invariance.

These types of meshes can be specified as hexahedral, so that the octree refinement code available in the official release of OpenFOAM can be applied. However, doing so breaks the single cell thickness constraint and typically introduces spurious modes in the invariant direction. To a lesser extent, the number of degrees of freedom is also artificially increased by the procedure. In order to avoid these issues, a quadtree approach, splitting cells in only two of the three directions, needs to be utilised. In this work, such a method was developed and further applied in the simulations, based on the code of [1]. This code was extended to include dynamic load balancing capabilities as well as other features, as described in [89].

4.1.2 Load Balancing

Parallel processing

Parallelisation of numerical computations is a typical mean to reduce simulation times. In OpenFOAM, parallel processing is performed using the Message Passing Interface (MPI) to communicate between different processors. Data allocated to each processor is determined by domain decomposition. There, the computational mesh is split into non-overlapping subdomains, each associated to one processor. Communication between the different domains is performed using a zero-halo-layer approach. In this approach, neighbouring subdomains only share boundary faces; data exchange between processors is handled, transparently to the user, by the means of appropriate boundary conditions. It should be noted that the computation domain can be described without need for a global reference domain. Data is only exchanged when needed by the MPI workers.

Dynamical load balancing

The domain decomposition of the computational domain is, in principle, initially set to equalise the load (number of mesh cells) on the different processors. Since the subdomains are defined spatially, adaptive mesh refinement can increase the load on only some of the subdomains. For computations where the refined region travels through the domain, a large load unbalance may arise. In that case, parallel efficiency is lost and the computation time is increased.

A solution to avoid such a loss of efficiency is to force a redistribution of the subdomains when the load unbalance grows above a user defined threshold. This operation can be performed during the parallel execution of the solver. [126] is an example of implementation of the method,

on which the procedure used in this work is based [89]. Using this method, parallel efficiency can be preserved by rebalancing the subdomains occasionally. The rebalancing procedure is illustrated in Fig. 4.1. While costly, these operations need to be performed only rarely, so that their total cost over the whole computation process is small. In order to maintain the capability to coarsen of the mesh, which relies on the refinement tree structure, each of its branches must lie in a single subdomain. This is achieved by forcing all child cells originating from the same level 0 cell to remain in the same subdomain.

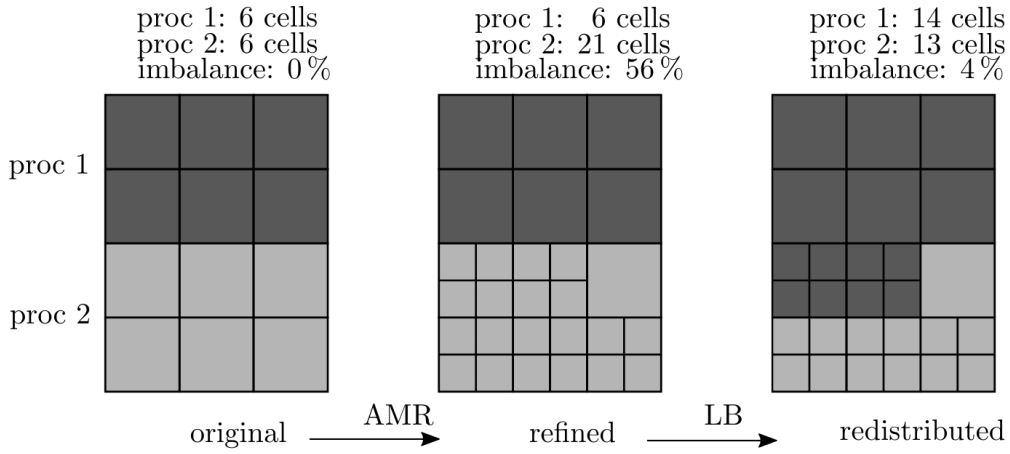

Figure 4.1: Load balancing mesh redistribution after refinement. After refinement, the loads associated to each of the processors differ. The imbalance is reduced by moving cells between subdomains. Picture courtesy of Dr.-Ing. D. Rettenmaier.

4.2 Two Mesh Procedure

The simulation of multiphase flow requires, in general, a description of the fluid motion only outside of solid parts. Solid parts are therefore usually excluded from the computational domain, acting on the fluids only from their physical boundaries. Similarly, the simulation of electroquasistatic fields requires a description of the electric potential only outside of perfect electrical conductors which typically represent electrodes in the problem. When the only elements in the computational domain are the fluids and metallic parts, a single grid can be used for the solution of the Electrohydrodynamic (EHD) problem. However, in presence of non-metallic solids, e.g. electrodes with dielectric coating, flow properties are undefined in these solids. The computational procedure must be modified accordingly.

One approach is to identify degrees of freedom associated with solid parts. Those can be simply ignored when assembling the system of linear equations; boundary conditions can be added to appropriately marked faces of the computational domain. The drawback of this approach is that the data structure of the degrees of freedom can no longer be associated with the mesh structure. Another approach is to introduce a second computational mesh as a subset of the

first, excluding solid parts. In this approach, the hydrodynamic problem is solved on the subset mesh, while the electroquasistatic problem is solved on the larger mesh. Index maps are used to transfer the field solutions from one mesh to the other. Since the fluid problem mesh is a subset of the electric field problem mesh, no field interpolation is required.

The second approach, used in this work, requires duplication of the geometry of part of the problem and of the associated fields. For parallel computations, the two different meshes can be decomposed independently. Thus, when the region of interest for fluid flow is small, the domain decomposition remains balanced on the subdomain, at the expense of additional communication to transfer quantities coupling the hydrodynamic and electroquasistatic problems.

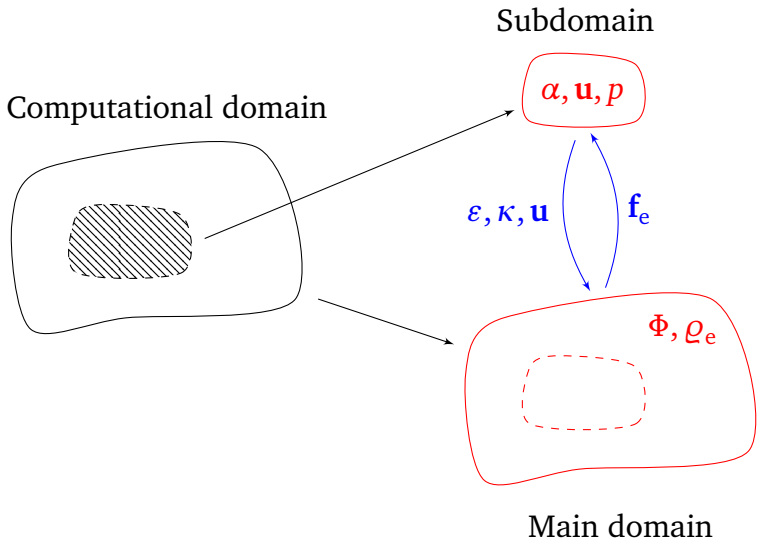

Figure 4.2: Two domain decomposition for the inclusion of solid bodies in computations. Two overlapping subdomains are used for the electroquasistatic and the hydrodynamic problem, respectively. Primary quantities (red) are calculated only on the corresponding subdomain. Secondary quantities (blue) are mapped consistently between the two domains to provide the coupling terms.

4.3 Coupling Procedure

The hydrodynamic solver and the EQS solver need to be coupled in order to obtain the fully coupled multiphase EHD solver. Due to the strong coupling between the electric fields and the fluid motion, the two problems need to be updated conjointly. In this work, this update is performed in a segregated manner, since the PISO algorithm solves the pressure-velocity coupled that way. First, the fluid-fluid interface is updated, according to the transport equation (3.40), and the surface tension force density is updated. In a second step, the fluid velocity and pressure distributions are calculated. Finally, the electric potential and free charge distributions are computed.

The hydrodynamic and electroquasistatic problems exhibit a strong mutual coupling that is due to the convection of free charges, and the electric force acting on fluid. The update of the velocity field must therefore be performed using the electric force value at the previous time step. This yields a prediction for the velocity field, used to calculate the free charge density. An additional outer loop can be used to provide a correction to the electric force distribution. In practice, this fixed point iteration procedure converges within a few iterations. This is primarily due to the small time steps typically used for the integration of convection dominated problems. An overview of the computations performed during a time step is shown in Fig. 4.3.

4.4 Moving Layer Problem

In order to validate the numerical approach and in particular the charge transport procedure, a simple one-dimensional problem is considered. A planar liquid layer of thickness L_l is transported passively with a constant velocity u in a surrounding gaseous environment. The two fluids are characterised by their permittivities, ε_l and ε_g, and conductivities, κ_l and κ_g, respectively. At time $t = 0$, an electric voltage U is applied between the two boundaries of the computational domain. The problem is schematically represented in Fig. 4.4. It can be related to a Maxwell-Wagner polarisation problem [127].

Since the velocity of the moving fluids is well below the speed of light, a transformation of reference frame alters the current density while preserving the electric field and charge density. Thus, the problem reduces to that of a plate capacitor with multiple conductive layers. The electric field in each of the layers is uniform. Furthermore, surface charge densities $\sigma_\pm$ are induced at the interfaces of the liquid layers. Due to charge conservation, $\sigma_- = -\sigma_+$, so that the electric field E_g in both gas layers is the same. The induced free charge on either front moves increases until a steady state is reached.

The analytical solutions for the transient electric field and surface charge densities are given by

$$E_\mathrm{l} = \frac{U}{L}\left[\frac{\kappa_\mathrm{g}}{\kappa_*}\left(1-e^{-\frac{t}{\tau}}\right)+\frac{\varepsilon_\mathrm{g}}{\varepsilon_*}e^{-\frac{t}{\tau}}\right], \tag{4.1}$$

$$E_\mathrm{g} = \frac{U}{L}\left[\frac{\kappa_\mathrm{l}}{\kappa_*}\left(1-e^{-\frac{t}{\tau}}\right)+\frac{\varepsilon_\mathrm{l}}{\varepsilon_*}e^{-\frac{t}{\tau}}\right], \tag{4.2}$$

$$\sigma_\pm = \pm\frac{U}{L}\frac{\varepsilon_\mathrm{g}\kappa_\mathrm{l}-\varepsilon_\mathrm{l}\kappa_\mathrm{g}}{\kappa_*}\left(1-e^{-\frac{t}{\tau}}\right), \tag{4.3}$$

where E_l and E_g are the electric field strengths in the liquid and gas layers, respectively, $\sigma_\pm$ are the two interface charge densities, $L = L_\mathrm{l} + L_\mathrm{g}$ is the total length of the computational domain, $\varepsilon_* = (L_\mathrm{g}\varepsilon_\mathrm{l} + L_\mathrm{l}\varepsilon_\mathrm{g})/L$ and $\kappa_* = (L_\mathrm{g}\kappa_\mathrm{l} + L_\mathrm{l}\kappa_\mathrm{g})/L$ are averaged material properties and $\tau = \varepsilon_*/\kappa_*$ is an effective charge relaxation time.

Figure 4.5 shows the results of numerical simulation compared to the analytical solution. The parameters of the problem are chosen as: $u = 1\,\mathrm{m\,s^{-1}}$, $\varepsilon_l = 4\varepsilon_0$, $\varepsilon_g = \varepsilon_0$, $\kappa_l = 1.5 \times 10^{-8}\,\mathrm{S\,m^{-1}}$, $\kappa_g = 1 \times 10^{-12}\,\mathrm{S\,m^{-1}}$, $L = 8L_g = 4\,\mathrm{cm}$; the mesh parameter is $\Delta x = 0.5\,\mathrm{mm} = L_g/10$. As seen in the figure, a good agreement between the numerical and analytical results is obtained, even considering the relatively low resolution. It should be noted that the electric field discrepancy is limited to the transition region delimited by the diffuse interface. Inside either fluid, the computed electric field agrees nearly perfectly with the analytical solution, as does the total interface charge.

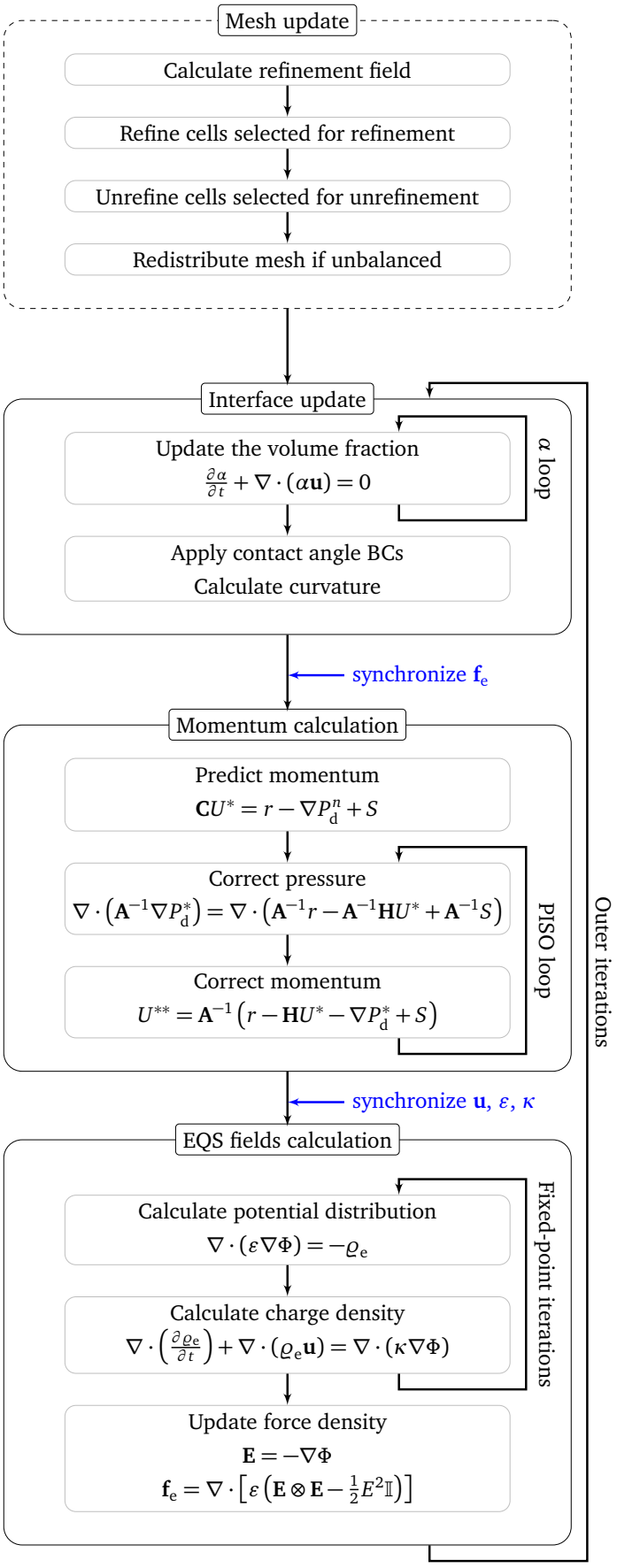

Figure 4.3: Flow chart of the time stepping scheme including the coupling of fluid dynamics and electric field problems.

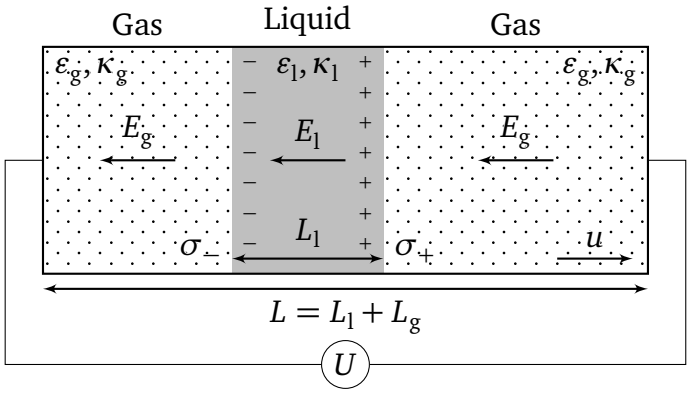

Figure 4.4: Schematic representation of the moving layer problem (adapted from [83]).

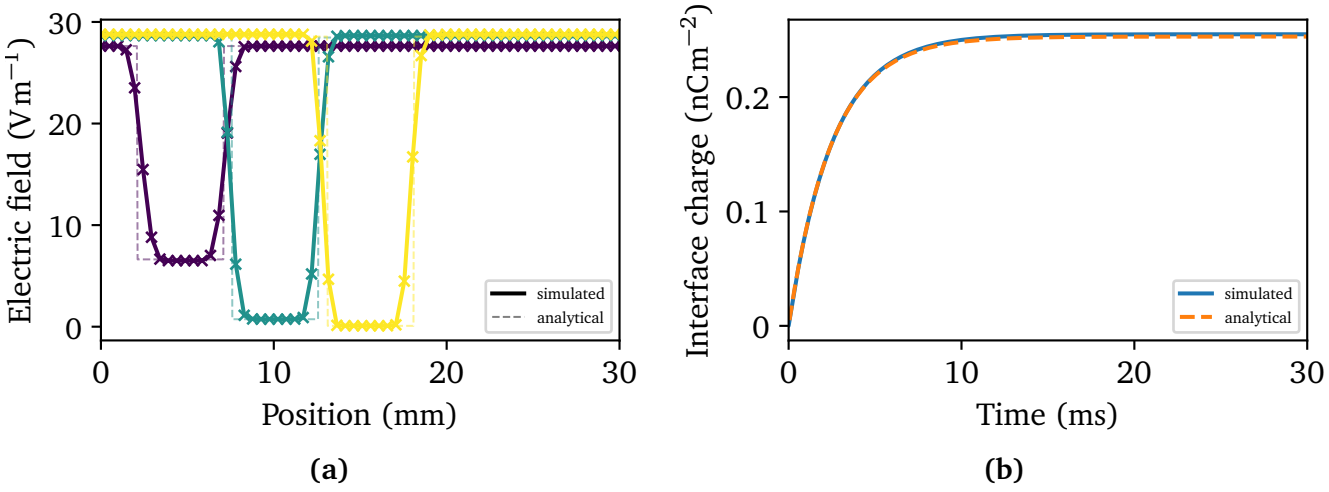

Figure 4.5: Comparison between analytical and numerical results for the moving liquid layer (adapted from [83]). (a) Electric field distribution at three different time instants after the external voltage is switched on. (b) Magnitude of the total charge at either fluid interface as a function of time.

5 Droplet Oscillations on High Voltage Insulators

5.1 Problem Description

On the surface of insulators in high-voltage surge arresters, rain droplets are subjected to strong AC electric fields. The electric forces induced on the liquids drive oscillations of the droplets. Due to the conductivity inherent to water, droplets are essentially equipotential. The curvature of their interface and the sharp corner at their contact line result in increased electric field strength in their vicinity. As a result of the enhanced electric fields, partial discharges occur at the surface of the insulators. These events gradually damage the surface of insulators and therefore reduce their efficiency [46], as shown in Fig. 5.1. In addition to the locally increased electric field strength around single droplets, the presence of multiple droplets can also produce discharges between neighbouring droplets [58, 77]. Examples of such discharges are shown in Fig. 5.2. This effect is strongly affected by the mechanical resonance of droplets oscillations [98]. Electric field asymmetries arising from the interactions between multiple droplets may also lead to droplet merging events [55].

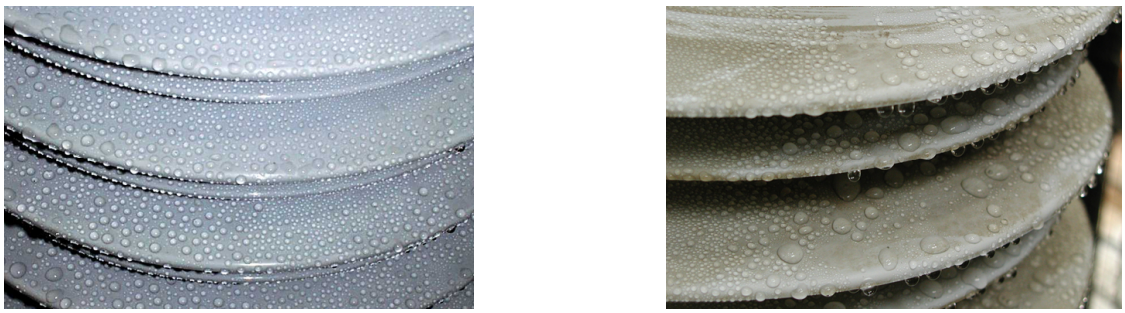

(a) **(b)**

Figure 5.1: Rain droplets on insulators. (a) Undamaged insulator. (b) Insulator damaged by partial discharges. Due to hydrophobicity loss, larger droplets are observed. Pictures courtesy of Prof. Dr.-Ing. V. Hinrichsen, Technische Universität Darmstadt.

Identifying the parameters causing partial discharge is of interest for understanding premature ageing of hydrophobic insulators. Both experimental and numerical studies of the problem have been performed. In [30, 31, 77, 84], Partial Discharge (PD) inception from sessile droplets has been studied experimentally. The presence of multiple droplets, their size, the inclination

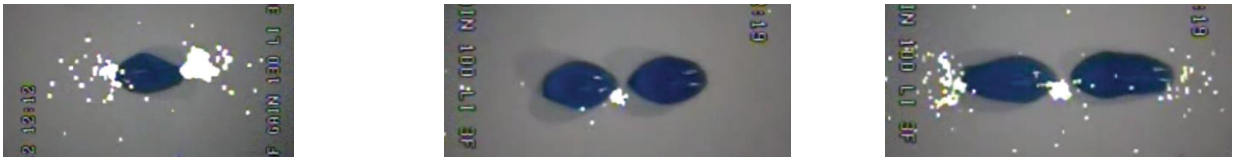

(a) **(b)** **(c)**

Figure 5.2: Location of partial discharges around (a) one sessile droplet and (b, c) two sessile droplets subjected to AC electric fields. Pictures courtesy of Dr.-Ing. M. Nazemi. In (b) partial discharges are observed mostly between the two droplets. At higher voltage in (c), partial discharges are observed on both sides of each droplet.

of the substrate and the applied frequency were shown to be parameters affecting the PD inception voltage. As the droplet oscillations were shown to be essentially modal, some simplified analytical models of the problem have also been derived, e.g. in [36]. Numerical simulations of the electric field distribution around static droplets on insulators have also been performed in [30, 44, 72, 141]. However, only static droplets were considered in these works, under the electrostatic assumption. Furthermore, their analysis considered the enhancement factor of the electric field with respect to the background field as an indicator for the partial discharge risks. Since the electric field is singular at the contact line of water droplets, as shown in Section 2.2.3, this enhancement factor is ill-defined. The dynamics of oscillating droplets were considered in [103] using a fully coupled electrohydrodynamic solver, and validated with experiments.

In this chapter, the EHD solver is used to simulate oscillations of droplets on insulators subjected to AC voltage. In the first part, the modes of oscillations of single droplets are considered, both in the presence and absence of net droplet charge. The effects of field asymmetries arising from charged droplets on the modes of sessile droplets are then discussed. In the second part, the PD inception voltage around static droplets is calculated using numerical simulations and compared to experimental results.

Unless specified otherwise, the experimental data in this chapter is provided by Jens-Michael Löwe (High Voltage Lab, TU Darmstadt).

5.1.1 Simulated Setup

In order to observe the dynamics of oscillating droplets, a simplified setup is used. Two electrodes are embedded in the substrate of interest, as shown in Fig. 5.3. This prevents the apparition of partial discharges from the electrodes themselves. This configuration provides a nearly uniform horizontal electric field in the test region where droplets are placed, as shown in Fig. 5.4.

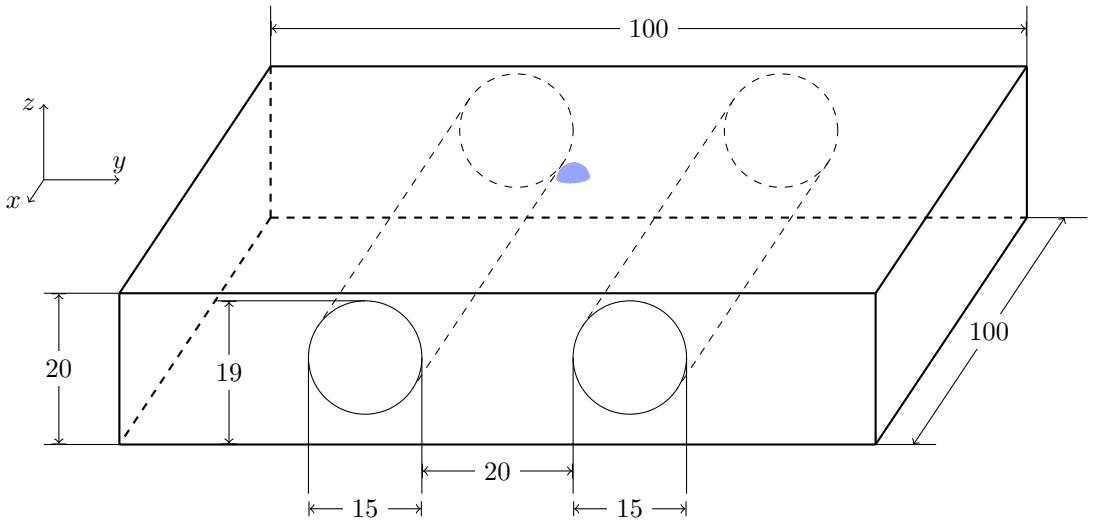

Figure 5.3: Electrode configuration generating the horizontal electric field driving droplet oscillations. The two cylindrical electrodes are embedded in silicone rubber (SiR). Test droplets are placed on top of the SiR surface between the electrodes. Dimensions are indicated in mm.

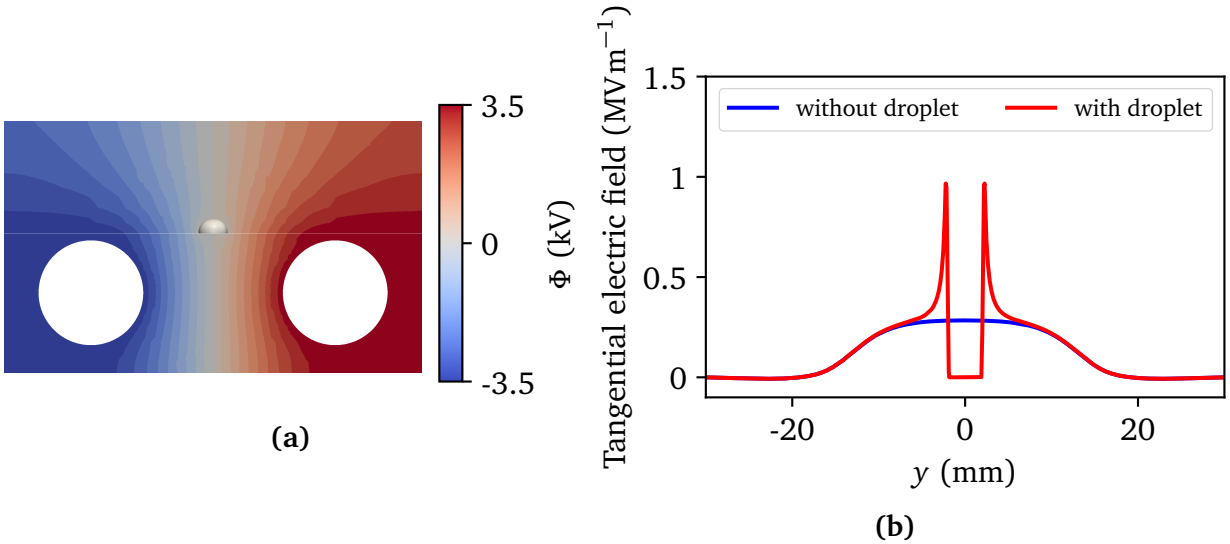

Figure 5.4: Electric potential distribution in the insulator (top) and electric field at the surface of the insulator (bottom) for an applied voltage of 7 kV. The presence of the droplet produces a sharp increase of the electric field in its vicinity.

On the Silicone Rubber (SiR) surface considered in this chapter, water droplets exhibit equilibrium contact angles around 100°, with a hysteresis range of ≈60°–140°. This range of hysteresis was estimated using image processing techniques to reconstruct the droplet shape from experimental high speed images. The minimum and maximum contact angles before contact line motion is observed are identified as the limiting receding and advancing contact angles, respectively. Both changing dynamic contact angle values, described in Section 2.1.1, and image processing inaccuracies may introduce a significant uncertainty on the range of hysteresis. In this section, oscillations of 20 μL droplets are considered for an applied voltage of 7 kV peak at 27 Hz. These choices generate a significant motion of the droplet, while ensuring that no partial discharge occurs, according to the experimental results from [77]. The chosen frequency drives droplet oscillations in the first symmetric and asymmetric modes. Unless specified otherwise, these parameters are used in the simulations presented in the following.

5.1.2 Initialisation Procedure

The initial droplet shape is calculated by integration of the Young-Laplace equation, (2.1), using the method described in Section 2.2.1. Using this droplet shape, the volume fraction field α is initialised in each cell of the computational domain by calculating the volume fraction of water in each cell numerically. This results in a diffuse interface with a thickness of a single cell. The application of the AC voltage is delayed by 0.1 ms in order to let the diffuse interface relax to its equilibrium thickness.

In order to consider the dynamics of droplets carrying a net charge, an additional step in the initialisation procedure produces the initial conditions as follows. First, the initial volume fraction is calculated for each cell of the computational domain. Then, each cell receives an amount of charge proportional to its volume fraction, calculated so that the total charge corresponds to the target net charge. Finally, the net charge distribution is corrected iteratively, by solving only the electroquasistatic equation, assuming no fluid motion. The steady solution, obtained after five charge relaxation times, provides the initial charge distribution for the fully coupled electrohydrodynamic problem. Note that, for moderate charge amounts, equilibrium droplet shapes are not significantly affected by the presence of net charge. Hence, the uncorrected equilibrium droplet shape is taken as initial condition.

5.1.3 Numerical Setup

In order to consider all oscillation modes of the droplets, the simulations are performed in 3D. The initial mesh is generated using the `snappyHexMesh` utility, to conform to the geometry of the problem. This produces a hexahedral mesh, except at the boundaries of the electrodes, where hexahedral cells are replaced by polyhedra conforming to the interface. As dielectric materials

need to be considered in the electroquasistatic field problem, the two mesh procedure described in Section 4.2 is used. The domain where fluid flows are considered is statically refined to have a cell size of 0.1 mm. Further refinement was found not to change significantly the modes of oscillations of the droplets. The dimensions of the domain are $8 \times 8 \times 3.5$mm. This was found to provide sufficient space to prevent boundaries from disturbing the oscillations of the droplets. For reference, the typical droplet radius for 20 μL droplets is 2.1 mm.

5.2 Driving Forces

5.2.1 Frequencies of Electric Forces

Symmetric oscillations have been observed experimentally at a frequency twice that of the applied voltage, while asymmetric oscillations occur at the frequency of the applied voltage [36, 67]. This can be explained by recalling that the total force density exerted by the electric field described by (2.30) contains two terms, $\mathbf{f}_c$ and $\mathbf{f}_p$,

$$\mathbf{f}_c = \varrho_e \mathbf{E}\,, \tag{5.1}$$

$$\mathbf{f}_p = \frac{1}{2}(\varepsilon - \varepsilon_0)\nabla(\mathbf{E}\cdot\mathbf{E})\,. \tag{5.2}$$

where $\mathbf{f}_c$ is the Coulomb force density on the free charge and $\mathbf{f}_p$ the polarisation force density. The magnitude of the respective forces are, in first approximation

$$F_{c,net} \propto QE\,, \tag{5.3}$$

$$F_{c,induced} \propto E^2\,, \tag{5.4}$$

$$F_p \propto E^2\,, \tag{5.5}$$

where Q denotes the total charge of the droplet. Here, the Lorentz force is separated in two components. $F_{c,net}$ corresponds to the effect of the applied electric field on the net charge carried by the droplet. $F_{c,induced}$ arises for conductive liquids, where the charge is redistributed at the interface by the external field. The charge density at the interface is proportional to the magnitude of the electric field, so that the corresponding Lorentz force is proportional to its square.

For a forcing voltage $U = U_0 \sin(\omega t)$, (5.3) to (5.5) become

$$F_{c,net} \propto QE_0 \sin(\omega t)\,, \tag{5.6}$$

$$F_{c,induced} \propto (E_0 \sin(\omega t))^2 = E_0(1-\cos(2\omega t))\,, \tag{5.7}$$

$$F_p \propto (E_0 \sin(\omega t))^2 = E_0(1-\cos(2\omega t))\,. \tag{5.8}$$

Here, E_0 denotes the applied electric field. As seen in (5.6) to (5.8), the three force contributions give rise to forced droplet oscillations at two different angular frequencies, ω and 2ω, respectively.

The conductivity of deionized water is $5.5\,\mu\mathrm{S\,m^{-1}}$. This leads to a charge relaxation time in water of $\approx 0.1\,\mathrm{ms}$, well below the duration of a period of oscillation of the droplet at frequencies of interest, i.e. $f \leq 50\,\mathrm{Hz}$. Thus, the charge redistribution at the surface of the droplet is essentially instantaneous compared to the time scale of fluid motion. For rain droplets, the charge relaxation time is several orders of magnitude smaller, so that the effect is even more pronounced in actual outdoor conditions.

Under these conditions, the electric field in the bulk of the liquid is essentially zero. The electric forces therefore act on water droplets only at the interface. For reference, the surface force distribution acting on a droplet close to its equilibrium shape is shown in Fig. 5.5. The distribution shown here is interpolated on the 0.5 isosurface of the volume fraction. Due to the diffuse nature of the VoF interface, the force density acts in the volume corresponding to the diffuse interface. Nevertheless, this representation approximates the relative magnitude of the forces along the interface well. Due to the antisymmetry of the problem, the force density vanishes along a plane parallel to the electrodes. The force density is largest in the vicinity of the contact line, as expected due to the electric field singularity at the contact line.

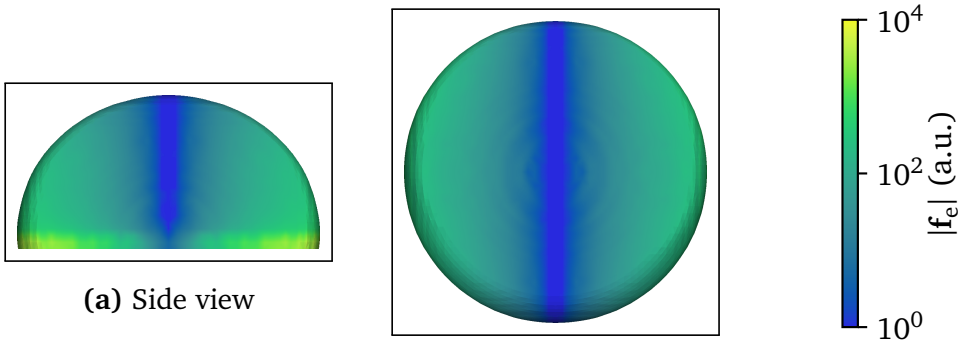

(a) Side view

(b) Top view

Figure 5.5: Electric force distribution acting at the surface of an uncharged droplet. The force distribution is shown using a logarithmic scale for clarity.

Asymmetric force distributions

In the case of single uncharged droplets, the force distribution is clearly symmetrical. However, multiple parameters may lead to asymmetric force distributions. The presence of net charge in droplets is one of them, see Fig. 5.6a. Interactions between multiple droplets can also produce asymmetric force distributions on symmetric droplets, as shown in Fig. 5.6b. Other sources, not considered here, may introduce asymmetries in droplet motion, such as the initial contact line shape, or the tilt of the insulator plate.

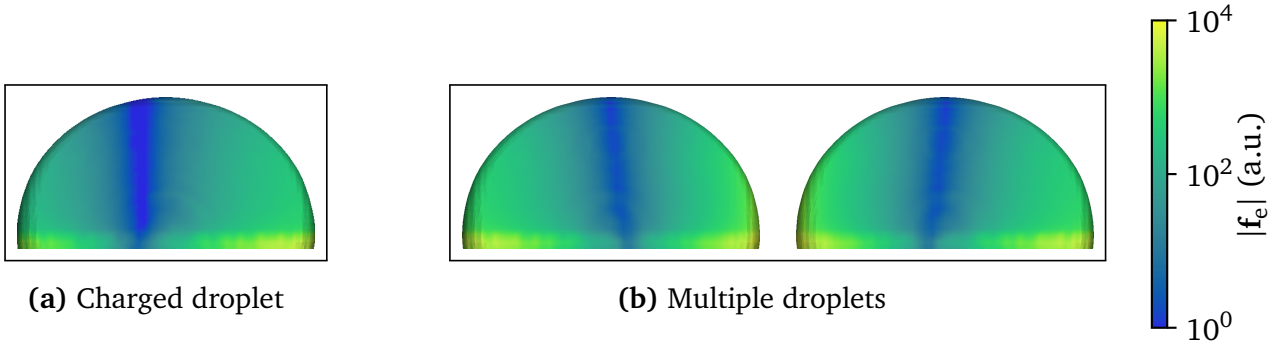

(a) Charged droplet **(b)** Multiple droplets

Figure 5.6: Asymmetric force distributions acting at the surface of droplets. The force distributions are shown using a logarithmic scale for clarity.

5.3 Validation

5.3.1 Oscillations of a Single Droplet

As the voltage is applied, the oscillations of the droplet quickly grow in amplitude. The oscillations approach a steady state after only a few periods of the applied voltage. The simulated dynamics of a single droplet oscillating nearly periodically are shown in Fig. 5.7. The visual comparison show that the simulated dynamics are in good agreement with the experimental dynamics.

The electric forces deform the droplet in the direction of the electrodes, flattening the droplet (see the $t + 9\,\text{ms}$ picture in Fig. 5.7). As the electric magnitude decreases with the applied AC voltage, the surface tension tends to restore the droplet toward its equilibrium shape. The equilibrium shape is overshot, thus producing the vertical elongation observed at t and $t+18\,\text{ms}$. Here, the nearly identical shapes at those time instants highlight the periodicity of the droplet motion over a half-period of the voltage. This indicates that the droplet oscillates at twice the frequency of the applied voltage, as expected in the absence of net charge in the droplet. The oscillation dynamics of single droplets are analysed in more detail in Section 5.4.1.

5.3.2 Electric Field Induced Merging of Droplets

In the presence of multiple droplets, the application of an external electric field may lead to merging events of droplets in close proximity. The effect may promote the creation of long conducting paths on the surface of the insulator, in addition to modifying the size distribution of sessile droplets. In this section, simulation results of the electrically induced merging of two droplets are presented and compared to experimental results.

Two identical droplets are generated at a distance from each other in the absence of electrical fields. At the instant $t = 0$, an external AC field forces the two droplets to merge. A comparison

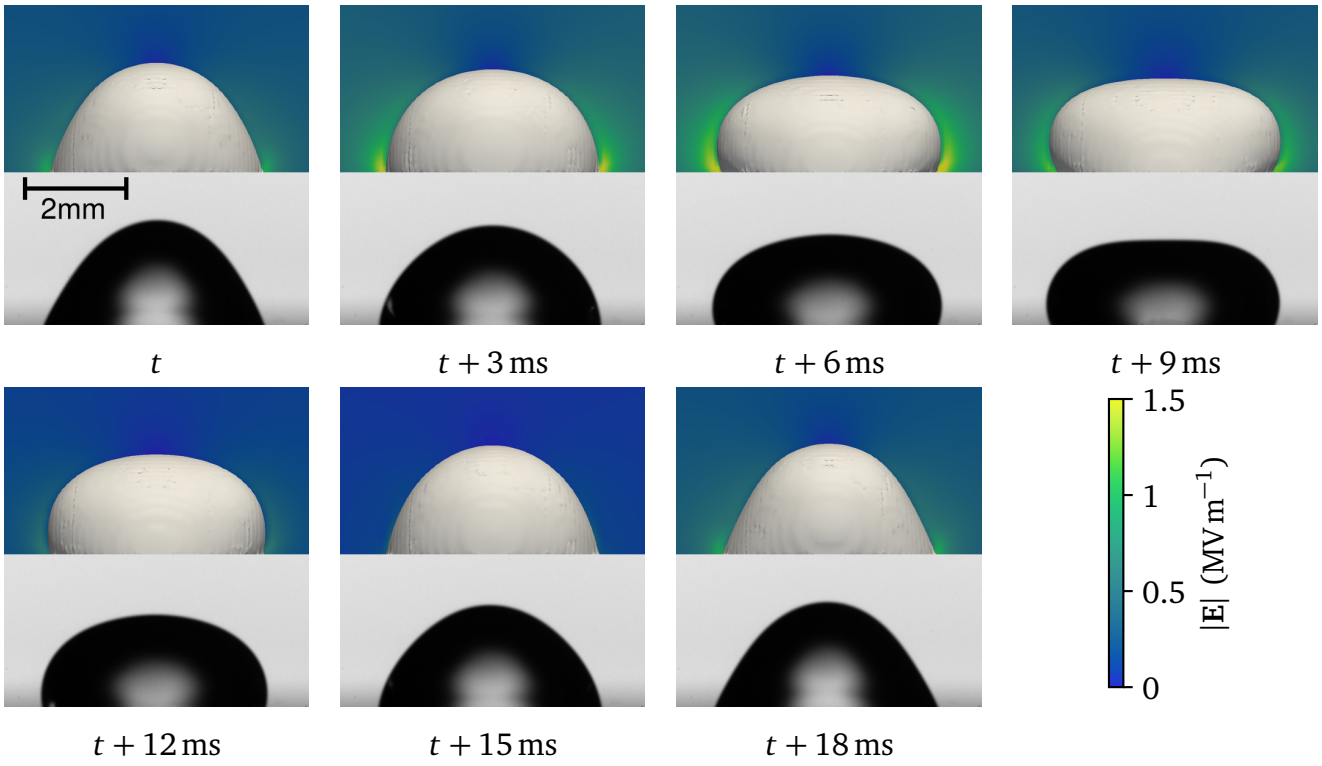

Figure 5.7: Oscillations of a single 20 μl droplet subjected to a 7 kV peak voltage at 27 Hz. One half-period of the voltage is represented. Top: simulation results; Bottom: experimental results.

between the experimental and numerical results is shown in Fig. 5.8. By visual inspection, the results are in good agreement for the shown time range.

In the presence of multiple droplets aligned with the electric field, the electric forces tend to elongate the droplets towards each other. Additionally, as shown in Fig. 5.6b, the presence of multiple droplets redistributes the electric force at the surfaces of the droplets. The larger force density at the interface between the two droplets further promotes a merging of the droplets. When the voltage is switched on, this leads to sudden motion of the contact line and droplet surfaces in the region between the droplets. A liquid bridge is formed between the two droplets, producing two capillary waves travelling along the surface of the droplet. Further oscillations are driven by the external field. The motion of the contact line during the merging event is mostly occurring in the direction of the electrodes. Little motion is observed in the transverse direction. The final shape of the contact line is therefore strongly elongated. This shows the impact of contact line hysteresis in droplet merging events. This enhances the formation of liquid bridges along the surface of insulators.

5.4 Dynamics of the Contact Line

5.4.1 Oscillation Modes of Charged and Uncharged Droplets

In a first step, the oscillations of an uncharged droplet are considered. The oscillations are characterised using the location of its mass centre, calculated from the simulated data. The oscillations of the droplet mass centre in the three different directions (vertical, parallel to the electrodes and in the direction of the electrodes) are shown in Fig. 5.9a. The frequencies of the oscillation modes, calculated by Fourier transform of the deviations of the mass centre coordinates, are shown Fig. 5.9b. As expected for the uncharged droplet, the vertical oscillations of the mass centre occur at double the frequency of the applied voltage, although as a double peak. Horizontal oscillations of small amplitude are observed as well. These asymmetric oscillations occur around the same frequency as the applied voltage. This is consistent with the findings in [13, 14], where azimuthally degenerate modes are found to oscillate with half the frequency of the forcing motion. Thus, the asymmetric mode at the same frequency as the applied voltage can be excited even in the absence of free charge.

The simulation is repeated for a droplet charged with 100 pC. This amount of charge is significant, compared to the charge displacement induced by the external field. It is furthermore consistent with the amount of charge that can be acquired by droplets on contaminated insulator surfaces [68]. The results are shown in Fig. 5.10. Compared to the case of the uncharged droplet, the frequencies of oscillations are essentially unchanged. However, the asymmetric mode oscillates with a much larger amplitude, as highlighted by Fig. 5.11.

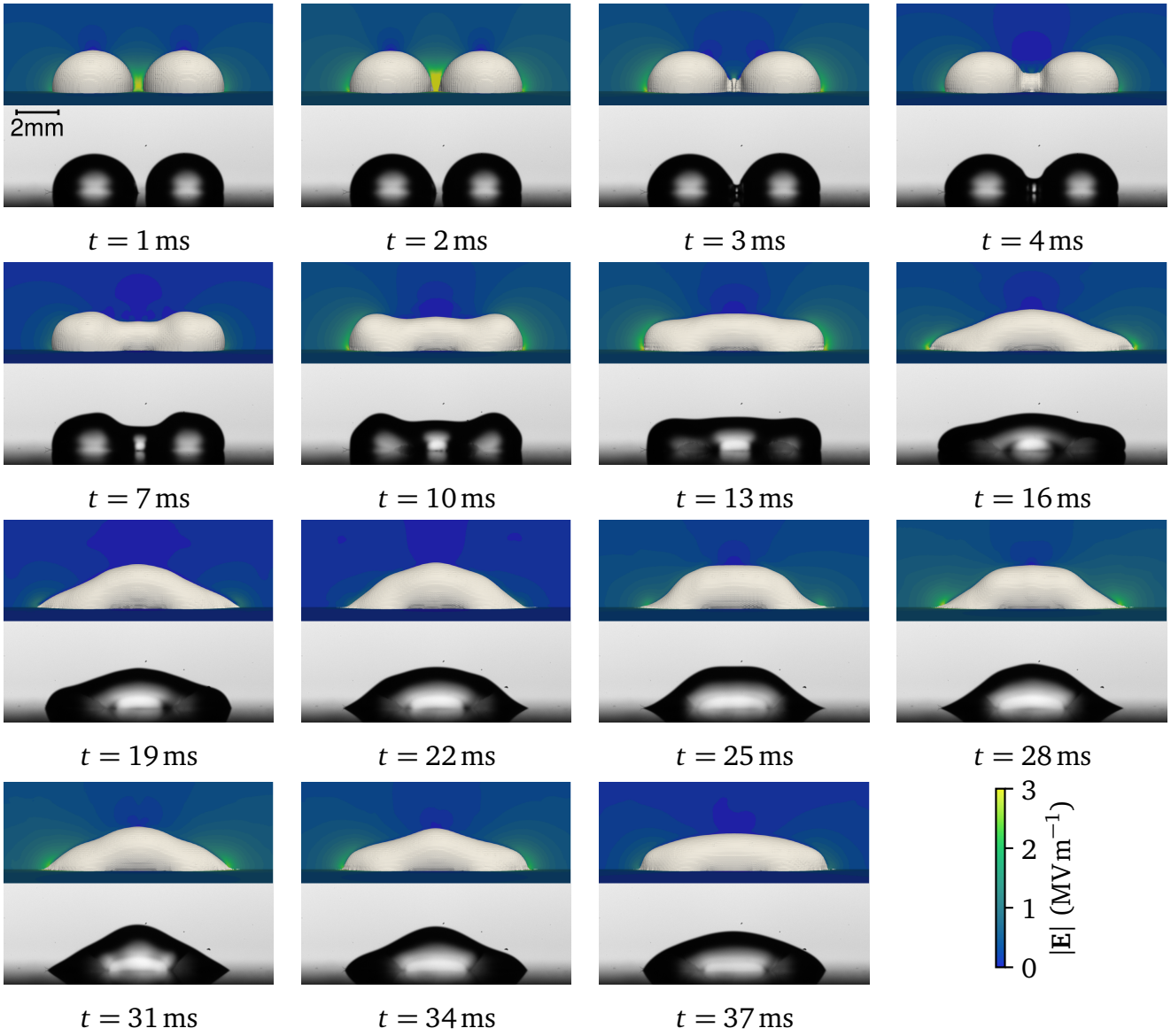

Figure 5.8: Dynamics of electrically induced merging of two 20 μl droplets subjected to an 18 kV peak voltage at 27 Hz. Top: simulation results; Bottom: experimental results.

5.4.2 Dynamics of the Contact Line

In this section, the behaviour of the contact line is analysed for the previously considered cases. The behaviour of the contact angle in the different directions for the uncharged droplet is shown in Fig. 5.12. The symmetry is highlighted by the oscillation profiles of the contact angle being nearly identical on opposing sides of the droplet. A slight discrepancy is visible on the oscillation frequencies, in the directions orthogonal and parallel to the electric field. While in both cases, a double peak around twice the frequency of the applied voltage is observed, in the orthogonal direction, the peak corresponding to twice the frequency of the applied voltage nearly vanishes.

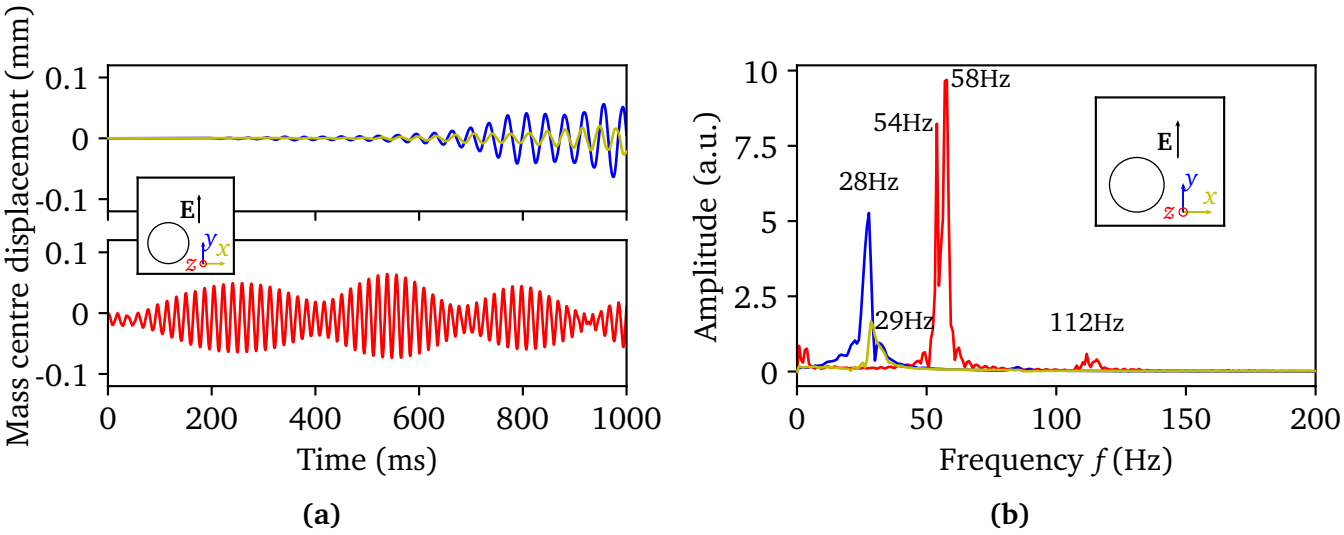

Figure 5.9: Oscillations of a 20 μL uncharged droplet subjected to a 27 Hz voltage. (a) Oscillations of the mass centre. (b) Oscillation frequencies of the mass centre. Red: vertical oscillations; blue: oscillations in the direction of the electrodes; yellow: oscillations parallel to the electrodes (see inset pictures).

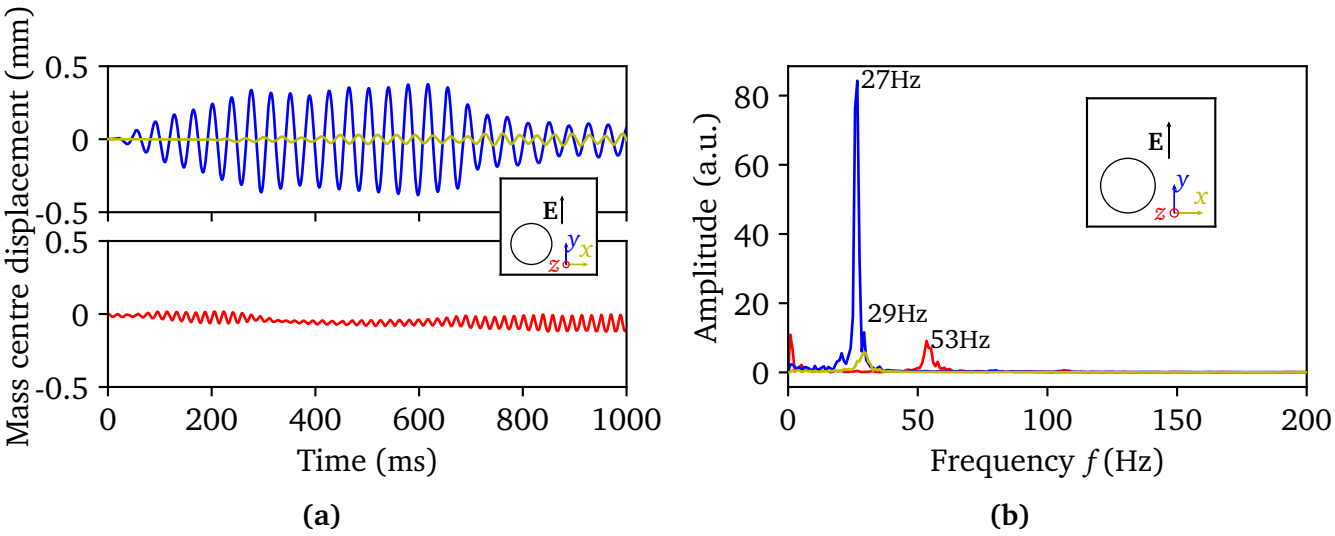

Figure 5.10: Oscillations of a 20 μL droplet charged with 100 pC, subjected to a 27 Hz voltage. (a) Oscillations of the mass centre. (b) Oscillation frequencies of the mass centre. Red: vertical oscillations; blue: oscillations in the direction of the electrodes; yellow: oscillations parallel to the electrodes (see inset pictures).

This is consistent with the modal motion of the droplet, since the force applied in this direction vanishes due to the antisymmetry of the electric field distribution.

In the case of the charged droplet, the behaviour of the contact line orthogonally to the applied electric field is unchanged. In the direction of the electric field, however, the contact angles have essentially opposite phases and a much larger range of oscillation. Thus, the limiting

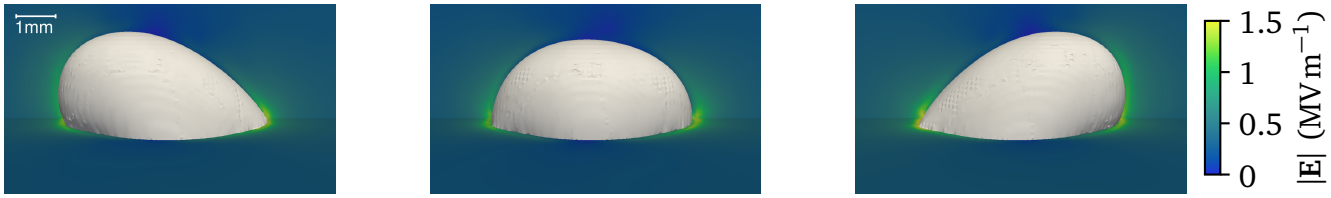

Figure 5.11: Shapes of an oscillating 20 μL droplet charged with 100 pC subjected to a 27 Hz voltage. The extreme shapes of the droplets over a half period are shown.

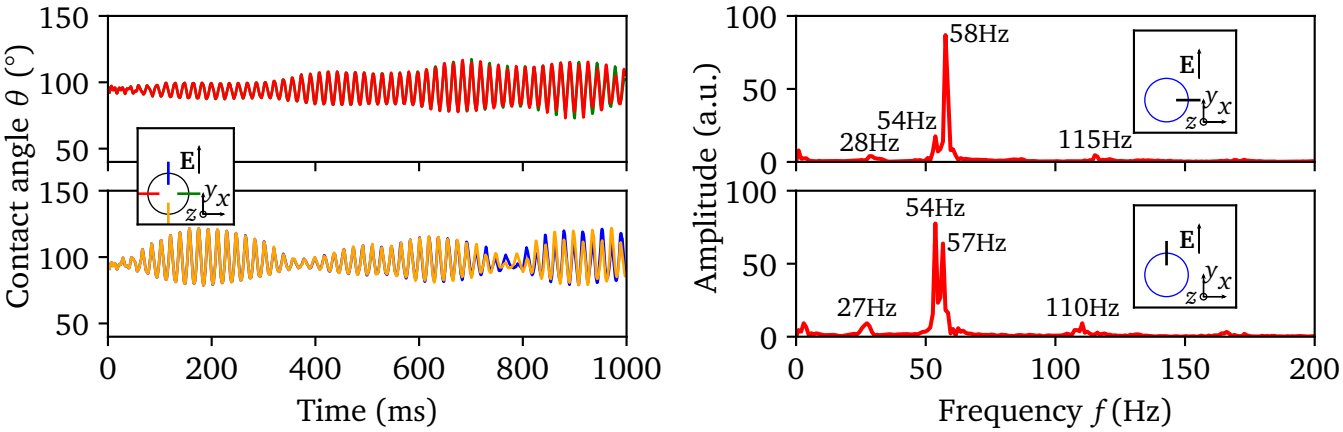

Figure 5.12: Contact line dynamics of a 20 μL uncharged droplet subjected to a 27 Hz voltage. (a) Instantaneous values of the contact angle orthogonally and parallel to the applied electric field. (b) Frequencies of the contact angle oscillations. The inset pictures show the directions of interest in each figure.

contact angles allowing for contact line motion are reached, thus allowing for stretching of the contact line in the direction of the electrodes. This, in turn, influences the modes of oscillation of the droplet. Multiple modes at slightly different frequencies appear, due to the elongation of the droplet [116]. Such a modification of the modes can be seen in the later dynamics ($t > 800$ ms) of the contact angle.

Range of contact angles at peak voltage

During the oscillations of droplets on the substrate, the contact line undergoes complex dynamics. In particular, due to contact angle hysteresis, moving contact lines of oscillating droplets exhibit a stick-slip motion [28]. Furthermore, as seen in Section 2.2.3, the strength of the electric field singularity at the contact line is modulated by the contact angle. The extreme values taken by the contact angles during the oscillations are therefore of interest to evaluate the risks of partial discharge occurring in the vicinity of the contact line.

The instantaneous contact angle values taken by a sessile droplet in function of the instantaneously applied voltage are shown in Fig. 5.14. The contact angle in the direction of the electric

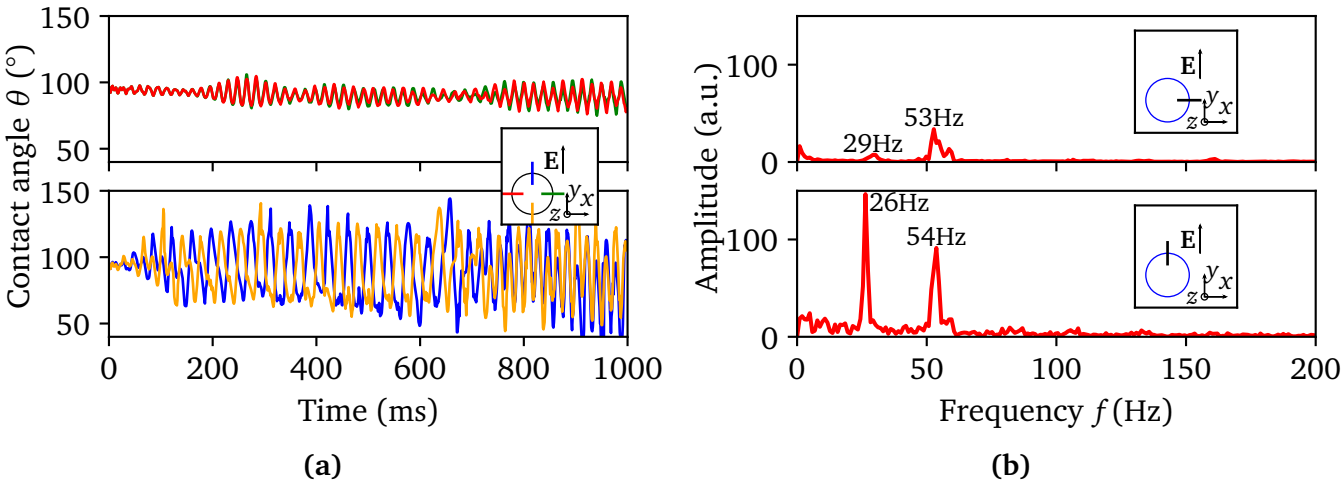

Figure 5.13: Contact line dynamics of a 20 μL droplet charged with 100 pC subjected to a 27 Hz voltage. (a) Instantaneous values of the contact angle orthogonally and parallel to the background electric field. (b) Frequencies of the contact angle oscillations. The inset pictures show the directions of interest in each figure.

field, where the electric field is strongest, is shown. Clearly, the contact angle values tend to be larger at the peak of the electric field (when $|U/U_0| \to 1$). The contact angle value corresponding to the worst-case singularity is attained when the voltage is close to 0. Nevertheless, the contact angle remains consistently significantly larger than the limiting receding angle, so that no recession of the contact line is observed.

In the presence of net charge, however, this observation cannot be made, as asymmetric oscillations introduce lower contact angle values at electric field peaks, as shown in Fig. 5.15. A droplet initially charged with 100 pC is allowed to oscillate in the same conditions as before. The behaviour of the contact angle is significantly different. The contact angle values at the electric field peak now span the whole range of contact line hysteresis. Some motion of the contact line is also observed, as indicated by the presence of contact angle values beyond the limiting static contact angle values.

Since the presence of a large net charge in the droplet is expected to cause oscillations mainly in the axisymmetric mode [67], the simulation is repeated with a net charge of 2 pC. The results are shown in Fig. 5.16. This amount of charge is insufficient to cause oscillation only in the asymmetric mode. Yet, over a number of oscillation periods, the amplitude of the asymmetric oscillations rises until a contact line behaviour similar to that of a droplet charged with 100 pC is observed (see Fig. 5.15). Consequently, due to surface charging appearing in the usual operating conditions [68], the contact angle values of rain droplets could span the whole range of contact line hysteresis. The worst case, i.e. contact angles slightly lower than the limiting receding angle, should thus be considered when estimating PD inception voltages.

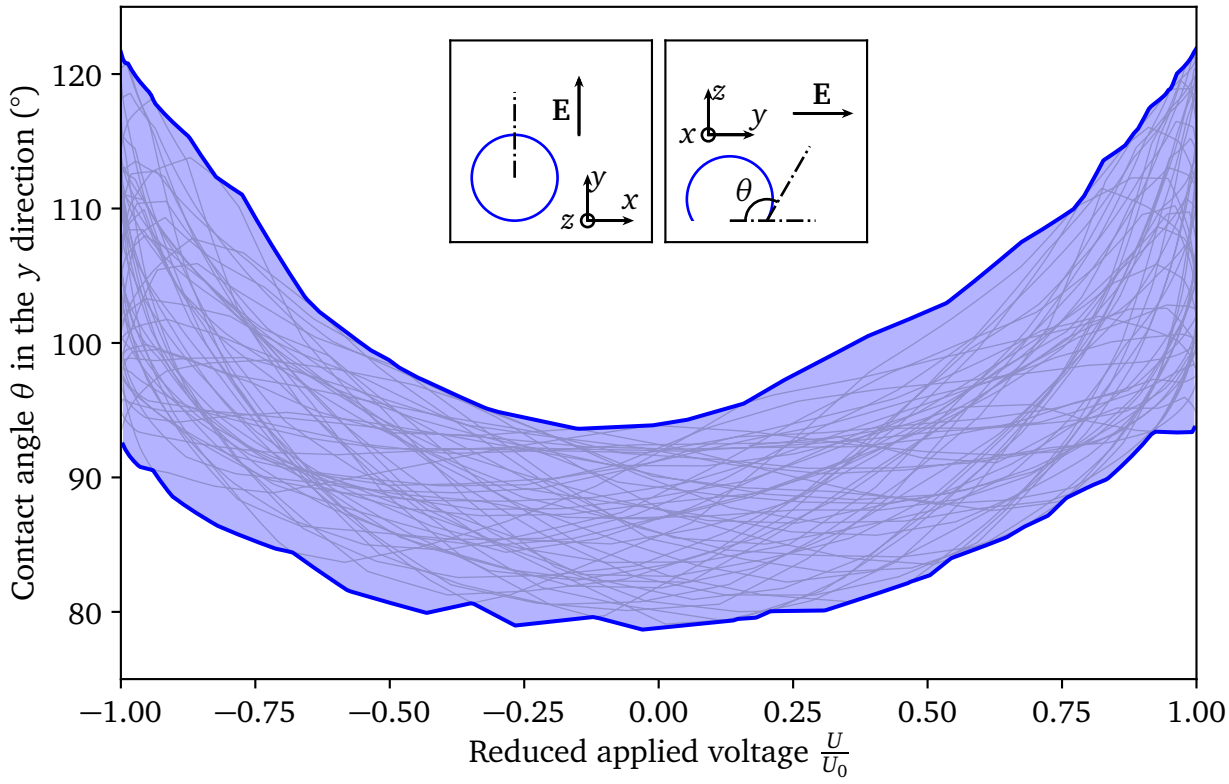

Figure 5.14: Range of contact angles observed in the direction of the electric field as a function of the instantaneous voltage, for a 20 μL uncharged droplet subjected to a 27 Hz voltage. The shaded area denotes the range of contact angle values. The light grey lines represent the instantaneous contact angles.

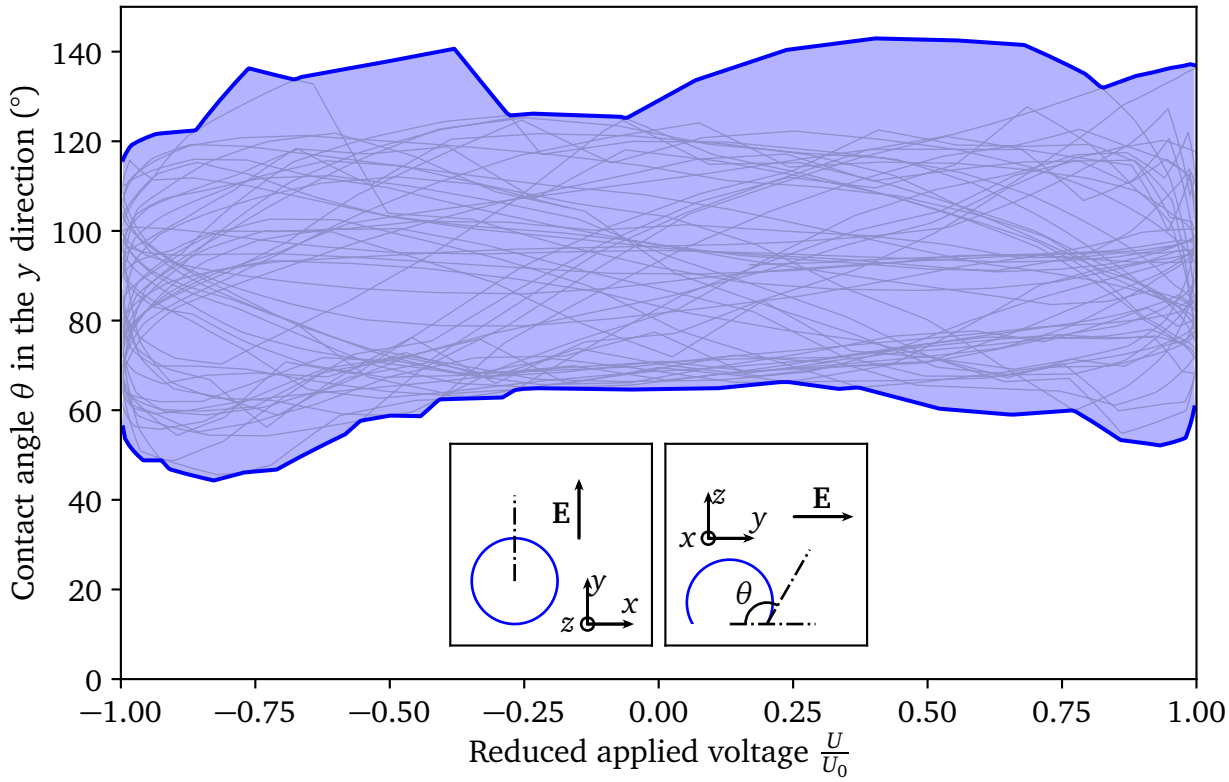

Figure 5.15: Range of contact angles observed in the direction of the electric field as function of the instantaneous voltage, for a droplet charged with 100 pC. The shaded area denotes the range of contact angle values. The light grey lines represent the instantaneous contact angles.

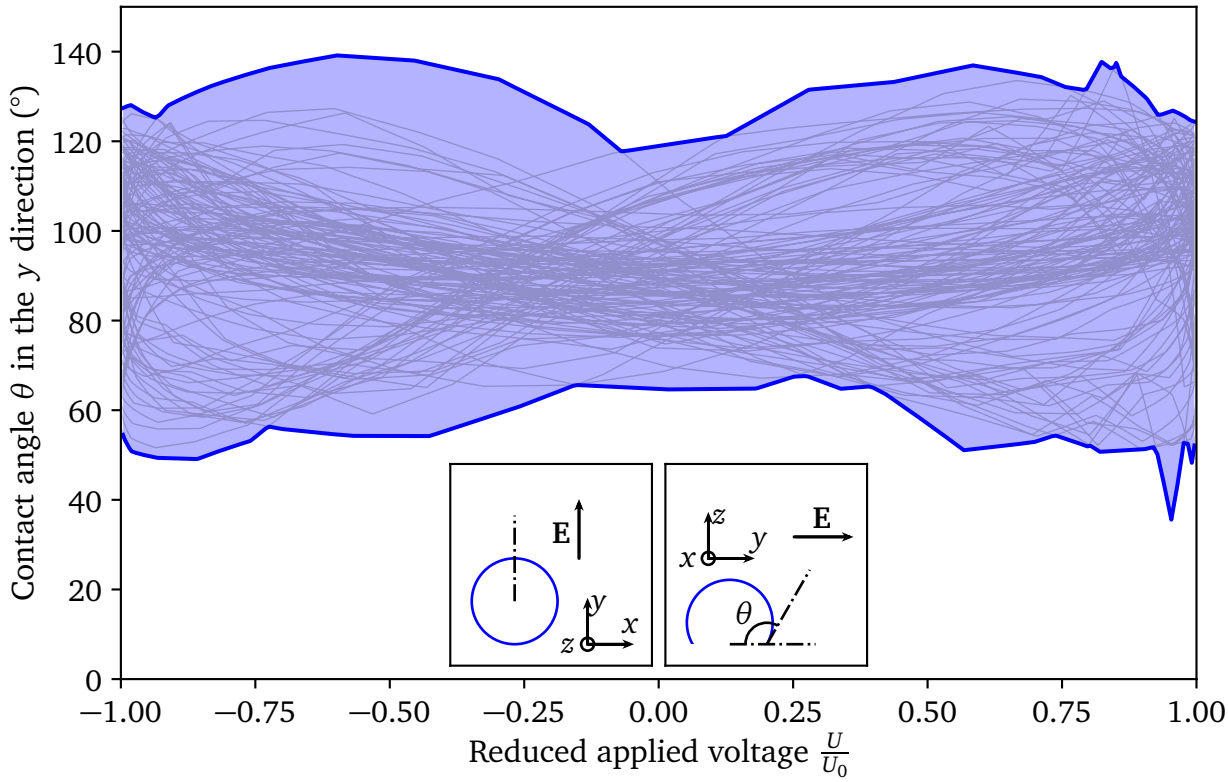

Figure 5.16: Range of contact angles observed in the direction of the electric field as a function of the instantaneous voltage, for a droplet charged with 2 pC. The shaded area denotes the range of contact angle values. The light grey lines represent the instantaneous contact angles.

5.5 Estimation of Partial Discharge Inception Voltage on Insulators

5.5.1 Basics of Corona Breakdown

Partial discharges occur when the electric field magnitude is locally sufficient to produce an electron plasma. The main phenomenon contributing to increasing the free electron density is the ionisation of gas molecules. The ionisation of gas molecules occurs when a free electron colliding with a molecule transfers a sufficiently large energy to unbind one electron, thus ionising the molecule. The presence of electric fields increases the probability of ionising collisions, by transferring energy to the free electrons. The generation of electrons by ionisation can be described, in the absence of other effects affecting the electron density, as [124]

$$\frac{\partial n}{\partial t} = \alpha n \,, \tag{5.9}$$

where n is the free electron density and α is a coefficient representing the rate of ionising collisions. The parameter α depends on the nature and pressure of the gas as well as the magnitude of the electric field.

At low free electron densities, two main effects counteract the accumulation of free electrons by ionisation: diffusion and attachment. Diffusion tends to reduce the gradients in the free electron density. Attachment occurs when free electrons are captured by gas molecules on impact. The continuity equation for the electron density n before the apparition of an avalanche thus reads [104, 124]

$$\frac{\partial n}{\partial t} = (\alpha - \eta) n + \nabla \cdot (D \nabla n) \,, \tag{5.10}$$

where α is the ionisation rate, η is the attachment rate and D the diffusion coefficient. The term αn describes the generation of new electrons by ionising collisions with the ambient air, while the term $-\eta n$ describes the attachment of free electrons to air molecules. The term $\nabla \cdot (D \nabla n)$ describes the diffusion of the free electrons. In general, α depends on the air pressure and magnitude of the local electric field, while η and D depend mainly on the air pressure [57]. In the following, the pressure dependency is dropped, as the pressure is the same for all considered cases. The ionisation coefficient α can thus be taken as depending only on the local electric field magnitude. As α generally grows with the magnitude of the electric field, so does αn in (5.10). As soon as the right hand side of (5.10) becomes positive, the free electron density locally grows: an avalanche can be initiated. The minimal corona discharge breakdown electric field, referred to as PD inception field, is thus obtained when attachment and diffusion effects are in equilibrium with ionisation [57]. Thus, the condition for a corona discharge to initiate reads

$$\frac{\partial n}{\partial t} = (\alpha - \eta) n + \nabla \cdot (D \nabla n) = 0 \,. \tag{5.11}$$

This criterion provides a minimum value for the electric field producing an increase in electron density. It does not guarantee the apparition of a sizeable avalanche, as (5.10) is valid only for low free electron densities. Equation (5.11) can therefore be seen as a conservative estimate of the corona breakdown voltage.

5.5.2 Evaluation of the Corona Breakdown Criterion

(5.11) does not need to be solved for a specific initial distribution of electrons n. Instead, any physical distribution for n which allows the electron density to locally grow is sufficient to fulfil the criterion.

Consider a problem for which the electric field distribution $\mathbf{E}_0$ is obtained numerically for a given input voltage U_0. Assuming a linear problem, the electric field $\mathbf{E}$ for any input voltage can be obtained by scaling the reference solution as $\mathbf{E} = s\mathbf{E}_0$. The free electron density n is considered on the same grid as the computed electric field distribution. The unknown n is expanded into a sum of weighted basis functions $\mathbf{n}$. For a given input electric field $\mathbf{E} = s\mathbf{E}_0$, after discretisation of (5.11), a system of equations of the form

$$\mathbf{M}(s)\mathbf{n} = 0\,, \tag{5.12}$$

is obtained. In (5.12), the coefficients of the matrix $\mathbf{M}(s)$ depend nonlinearly on the scaling factor, due to the nonlinear dependency between the ionisation coefficient and the electric field. A non-trivial solution for (5.12) exists when $\det(\mathbf{M}(s)) = 0$. The scaling factor can be swept until this condition is fulfilled, providing thus the corona breakdown electric field. In general, instead of calculating the determinant of $\mathbf{M}(s)$, a value of the parameter s for which $\mathbf{M}(s)$ has a zero eigenvalue can be searched. Thus, by varying s and tracking the first eigenvalue until a sign change, the corona breakdown field can be found. A search by bisection can thus be used to obtain the breakdown field in a few iterations [57].

Simulation procedure

The results presented in the following are based on the commercial softwares Spark3D 2019 SP1 and CST Studio Suite 2019. The FEM is used to solve the full Maxwell equations in the frequency domain for a frequency of interest, e.g. 50 Hz. Note that, due to the extremely low frequency, the exact frequency value has no impact on the later computations. The obtained solutions for the electric and magnetic fields in free space, are used as input for the Spark3D solver. In a second step, the Spark3D solver calculates the scaling factor on the input power required to fulfil (5.11). Taking the square root of this scaling factor provides the scaling on the input voltage and thus the PD inception voltage.

The simulations were repeated for different mesh resolutions, in particular in the region of the contact line. The PD inception voltages calculated using the coarsest and finest mesh resolutions

differed by only up to a few percent. Typical simulation times in Spark3D ranged from a few seconds to a few hours, depending on the mesh resolution. However, as will be shown in Section 5.5.3, the location of the partial discharges is predictable. The computational costs of the simulations were therefore strongly reduced by restraining the computational domain for Spark3D to small regions of interest. The simulation times were then reduced to a few tens of seconds, while preserving the accuracy of the finer meshes.

5.5.3 Partial Discharge Prediction for Static Droplets

The corona breakdown criterion can be evaluated for linear problems using the procedure described in Section 5.5.2. However, the electric field distribution around oscillating droplets is clearly time-dependent and nonlinear. Since partial discharges around single droplets are expected to originate from the vicinity of the contact line, we reduce the problem to the estimation of PD inception voltage around static droplets.

Validation of results for static droplets

In a first step, the simulation procedure is validated against experimental results. In order to retain the electrical properties of water while keeping the droplets static, a water-gelatin mixture was used. The droplets, once generated, were cooled down to freezing temperature before performing the partial discharge experiments. High speed videos were taken in order to ensure that the droplets remained motionless. In addition, the droplet shapes were extracted, assuming axisymmetry, to generate the geometry in the simulations. The experimental and simulated results are compiled in Table 5.1. The simulated PD inception voltages are in good agreement with the experimental values, with a maximal relative deviation of 7.3%.

Location of partial discharges

The simulation procedure is performed with a number of axisymmetric droplet shapes, calculated using the procedure detailed in Section 2.2.1. The location of the simulated partial discharges is shown in Fig. 5.17, for different contact angle values. In all cases, partial discharges start at the contact line, in the direction of the electrodes. In some cases, a slight deviation of the direction is observed. The hypothesis that the contact line plays a major role in the apparition of partial discharges is thus verified by the numerical simulations. In each case considered in the following, partial discharges were found to start from the contact line of the droplets.

Effect of contact angle and droplet volume

The wettability of the surfaces and the volume of the sessile droplets are known to have a large impact on the PD inception field [31, 44, 77, 84]. Partial discharges from droplets

Volume	Droplet shape	Electric field pattern	Inception voltage (Experiment)	Inception voltage (Simulation)
21.95 μl	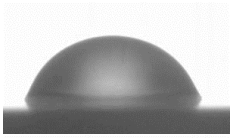	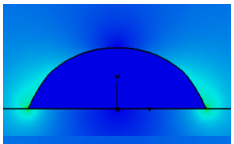	13.52 kV	13.49 kV
12.83 μl	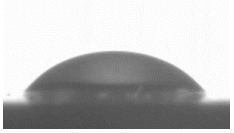	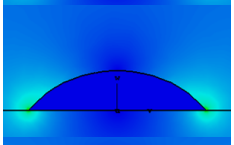	13.32 kV	13.22 kV
19.77 μl	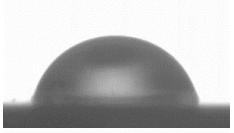	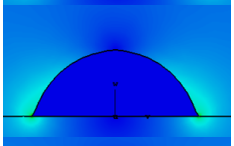	15.41 kV	14.29 kV
20.08 μl	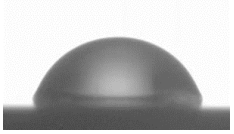	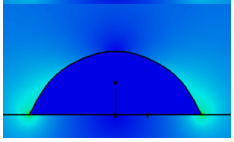	15.27 kV	14.58 kV

Table 5.1: Comparison between experimental and simulated partial discharge inception voltages for a few static droplets (water+gelatin mixture).

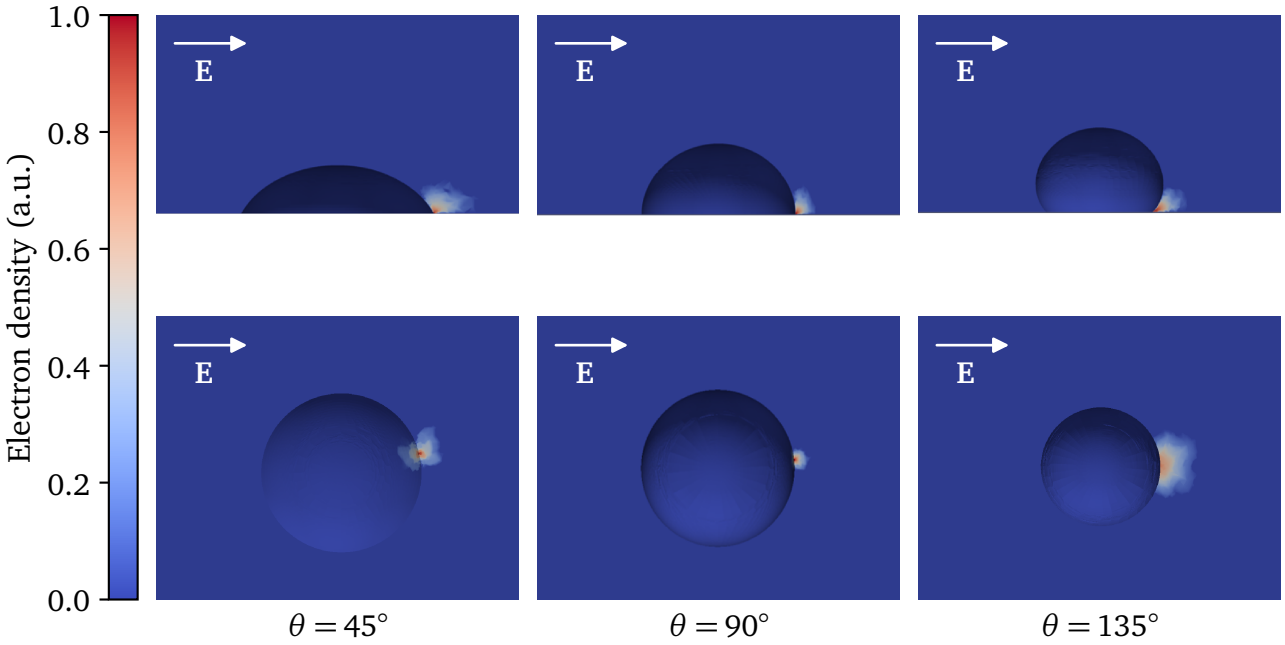

Figure 5.17: Location of partial discharges for 40 μl static droplets with different contact angles.

of various sizes and contact angles are therefore considered in a second step. The results, shown in Fig. 5.18, indicate that the PD inception voltage decreases both with increasing droplet volume and decreasing contact angle. Over the range of volumes considered, the contact angle plays a large role, decreasing the inception voltage by more than a factor 2 from $\theta = 150°$ to $\theta = 30°$. The dependency on the volume is observed mostly for smaller droplets. For rather large droplets ($\geq 40\,\mu$l), the variation with the volume is modest ($\leq 20\%$). The major role played by hydrophobicity is thus confirmed, as hydrophobic surfaces result in smaller droplets with larger contact angles, and hence largest inception voltages.

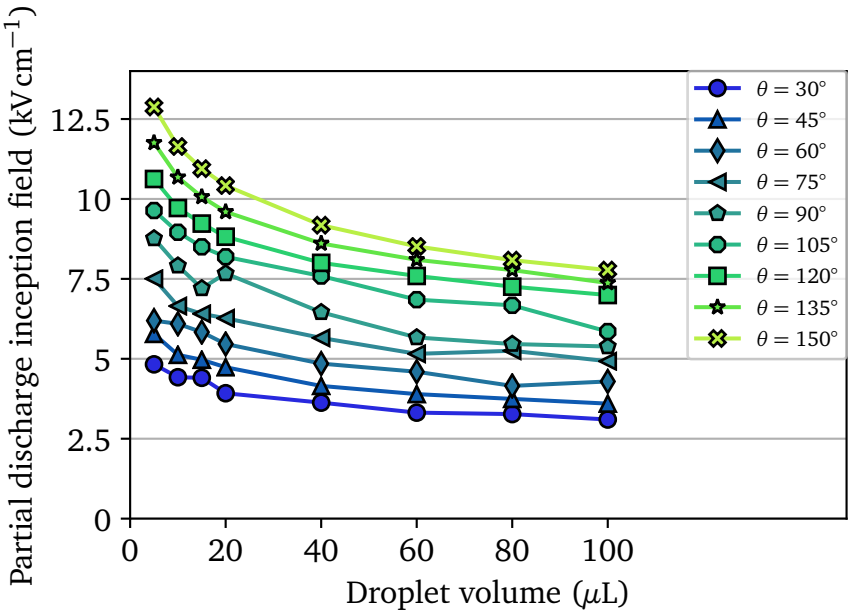

Figure 5.18: Partial discharge inception voltage for a number of droplet volumes (5 to 100 μl) and equilibrium contact angles (30 to 150°).

For reference, the results for contact angles between 75 and 105° are compared with experimental results from Dr.-Ing. M. Nazemi [77] in Fig. 5.19. Although the experimental data is obtained for oscillating droplets, the simulated values are close to the experimental breakdown voltage values. These values are, thus, consistent with the results shown in Fig. 5.14, where contact angles values close to 90° are obtained at the applied voltage peak.

The inception field can also be related to the singularity indices calculated in Section 2.2.3. The results, shown in Fig. 5.20, indicate that the inception field correlates positively with the singularity index, as expected. With this representation, the volume of the droplets seem to act as a geometric parameter acting multiplicatively on the inception field.

Effect of substrate permittivity

The effect of the permittivity can be evaluated numerically by changing the material properties of the substrate. The PD inception voltage for different substrate permittivities is shown exemplarily in Fig. 5.21, for a 20 μl droplet with different contact angle values. The influence

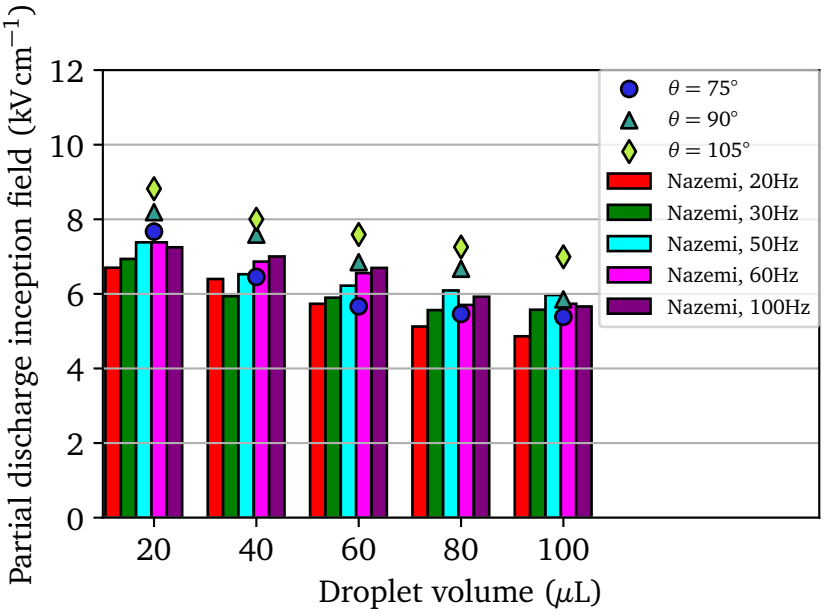

Figure 5.19: Partial discharge inception voltage for a number of droplet sizes and equilibrium contact angles. The markers correspond to the simulated results. The experimental results from Dr.-Ing. M. Nazemi [77] for different voltage frequencies are shown for comparison.

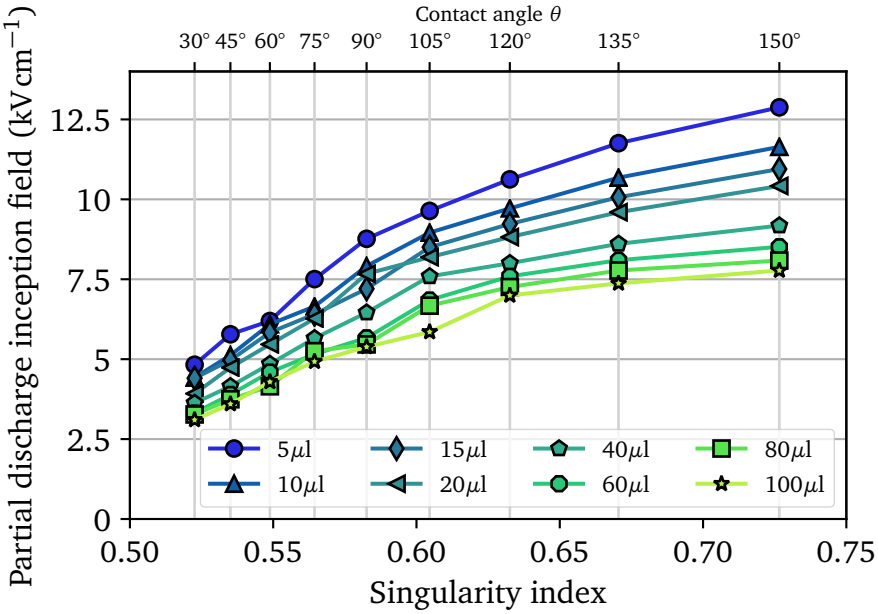

Figure 5.20: Partial discharge inception voltage for a number of droplet volumes (5 to 100 μl) and equilibrium contact angles (30 to 150°), as a function of the singularity index.

of the permittivity strongly depends on the contact angle. For the lowest contact angle value, increasing the permittivity only reduces the inception voltage by $\approx 10\%$. For the highest contact angle value, the inception voltage is halved over the same range of permittivities. The observation is consistent with the results shown in Fig. 2.7 concerning the singularity index. For low contact angles, the range of variation of the singularity index for varying permittivities is small. However, it quickly grows with the contact angle value.

Partial discharges between two droplets

In presence of multiple droplets, the modified electric field patterns influence the inception voltage. The PD inception voltage as a function of the distance for two identical droplets is shown in Fig. 5.22. The asymmetry resulting from the presence of an additional droplet leads to further enhancement of the electric field between the two droplets. As a result, the PD inception voltage reduced drastically when the distance between the contact lines goes to zero. However, for a distance of a few millimetres, the PD inception voltage of the single droplet case is recovered.

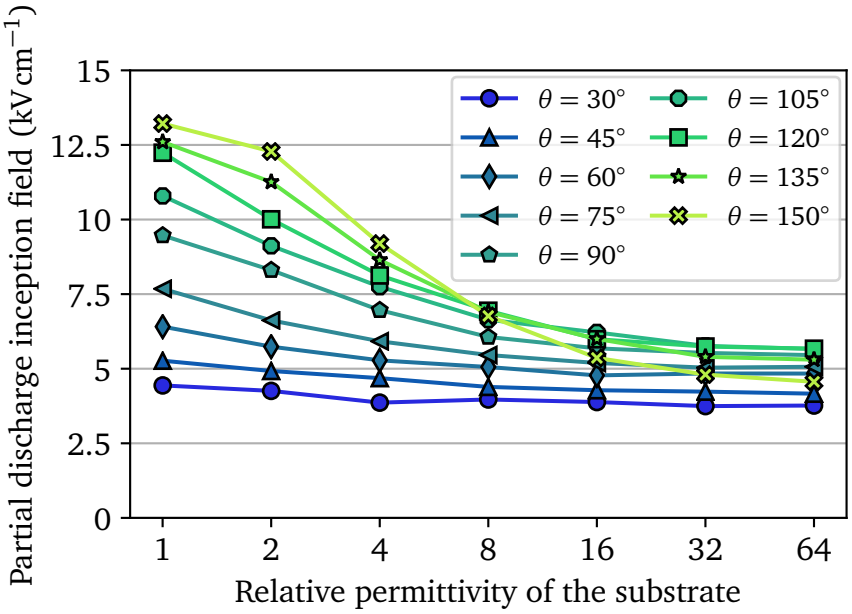

Figure 5.21: Partial discharge inception voltage in function of the substrate permittivity, for a 20 μl droplet with different contact angles.

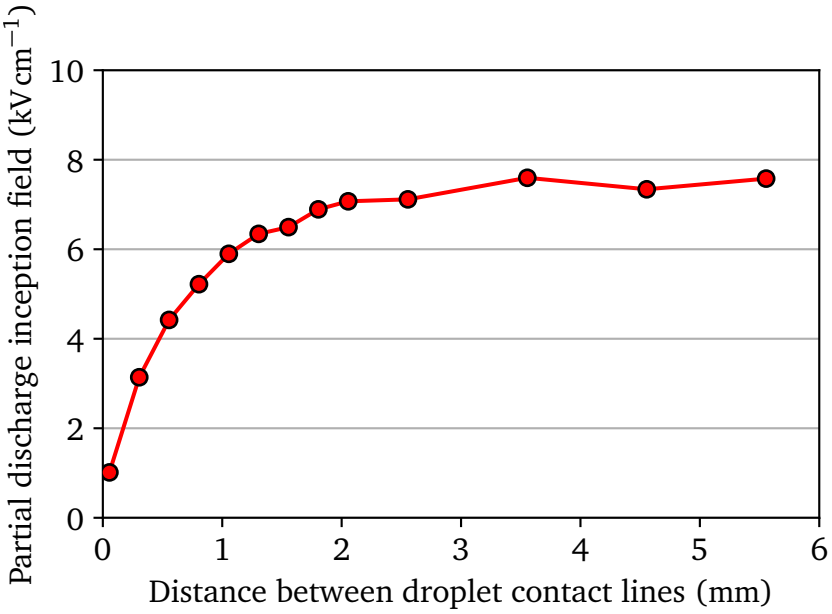

Figure 5.22: Partial discharge inception voltage in function of the distance between the contact lines of two droplets with volume 20 μl and contact angle 90°.

6 Electrically Forced Droplet Generation

6.1 Problem Description

In combustion processes, liquid fuels and oxidisers are introduced into combustion chambers as sprays of droplets. The different fluids mix in the chamber after vaporisation, allowing for the ignition and combustion processes to take place. Due to the high pressures involved, liquids may be introduced above supercritical conditions in the combustion chamber [135]. The study of the mixing behaviour of liquids in supercritical conditions is therefore of interest for the characterisation of combustion in these conditions. Experimental investigations of the mixing behaviour at the scale of a single droplet are required to characterise the mixing properties. The mere presence of a suspending apparatus during experiments is sufficient to affect evaporation rates at the surface of droplets [100, 128]. Studying free falling droplets avoids the issue of suspension and of stagnation of the gas phase around droplets. An example of the mixing behaviour of free falling n-pentane droplets at near critical conditions is shown in Fig. 6.1, along with the experimental chamber. Differences in the density of the surrounding gas as the droplet evaporates are highlighted by the shadowgraphy images. This mixing behaviour needs to be characterised statistically, by performing a large number of experiments. The reproducibility of the droplet generation then becomes a major concern for the study of the mixing behaviour. However, the vanishing surface tension at near critical conditions results in droplet instability, impacting the reproducibility negatively. This instability can be alleviated by forcing the detachment of the droplet by an external cause, e.g. mechanical disturbance created by motion of the capillary supporting the droplet (see [106]) or electric forces (see [129]).

An electrically induced droplet detachment was shown to produce good droplet generation reproducibility, even near critical conditions, in the case of acetone droplets. However, the detachment dynamics of lower conductivity liquids, such a n-pentane, differed significantly. Those detachment dynamics were not understood at the time. In addition, unexpected behaviour of free falling droplets in the pressure chamber hinted at the presence of net charge in some detached droplets. A characterisation of the droplet generation dynamics by numerical simulation is thus required to prevent the generation process from spoiling experiments in the pressure chamber.

In the following, the characterisation of an on-demand droplet generator (see [105, 129]) where single droplet detachment is forced by external electric fields is presented. The behaviour of two test liquids, acetone and n-pentane, subjected to the external electric field is

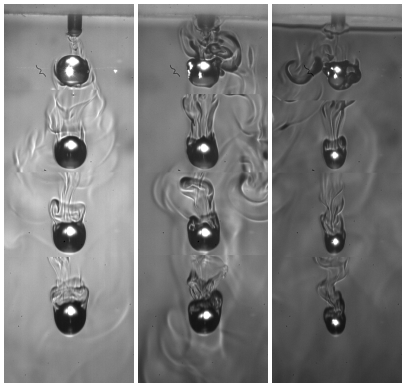

(a)

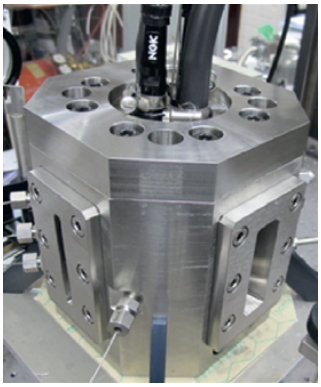

(b)

Figure 6.1: (a) Shadowgraphs of free falling n-pentane droplets at supercritical pressure and different temperatures [105]. (b) Experimental pressure chamber for the study of the mixing behaviour [129]. Pictures courtesy of C. Steinhausen.

investigated and compared with experimental results. These two liquids represent, respectively, the case of high and low conductivity liquids, which are shown to present a completely different detachment behaviour [83]. Then, some of the characteristics of droplet detachment originating from the electrically controlled detachment are investigated. These include the presence of net charge in the detached droplet, the amplitude of droplet oscillations and the dynamics of satellite droplets.

6.1.1 Generator Description

The droplet generator is composed of a metallic capillary located between two electrodes on its sides. The two electrodes are connected to the same voltage supply, while the metallic capillary is grounded. In order to prevent electric breakdown, the two electrodes are embedded in two large insulating blocks. The capillary and electrodes are installed in a pressure chamber able to sustain high pressures and temperatures. A model of the pressure chamber is shown in Fig. 6.3a. Injection of the test liquids can be performed under pressure and temperature conditions close to their critical pressure and temperature. The gaseous phase in the pressure chamber is typically composed of nitrogen in order to prevent ignition of the fluid mixture by spurious sparks.

Initially, the capillary feeds liquid into the pressure chamber with a constant mass flow rate, typically $2\,\mathrm{g\,h^{-1}}$ to $10\,\mathrm{g\,h^{-1}}$, until a pendant droplet is formed, as indicated in Fig. 6.3b. As a reference, for acetone at 20 °C under 1 bar, the corresponding mean inlet velocity is $2.2\,\mathrm{cm\,s^{-1}}$ to $11\,\mathrm{cm\,s^{-1}}$. Typical droplet filling times are 1.5 s to 8 s. The maximal droplet volume obtained with this capillary depends on the temperature and pressure conditions, and varies between $2\,\mu$l to $5\,\mu$l. The volume of the droplets is evaluated a posteriori using high speed (4000 fps) footage of the detachment process. The presence of a droplet on the capillary is monitored by an optical

device, which provides a trigger signal for the detachment process. The optical setup can be adjusted to force the detachment of droplets at specific heights below the capillary.

As soon as a droplet is detected by the optical setup, a short voltage pulse, lasting 10 ms to 50 ms is applied via the electrodes. The induced electric force destabilises the droplet, thus forcing droplet detachment. The typical voltage required for the pulse is 1.5 kV to 5 kV. The amplitude and duration of the voltage pulses are chosen to avoid detachment of the droplets in electric fields, which would produce charged droplets. Since surface tension tends to restore the pendant droplet, the imparted impulse needs to be sufficient to ensure detachment.

Observations show that the droplet detachment time, charging behaviour and flow dynamics after detachment depend strongly on the electrical properties of the liquid phase. This is due to the modification of the local electric field pattern by the droplet. For reference, the conductivity of acetone is $20\,\mu\mathrm{S\,m^{-1}}$, resulting in a charge relaxation time of approximately $10\,\mu s$. This is well below the time scale of droplet motion on the capillary. The conductivity of n-pentane is $20\,\mathrm{pS\,m^{-1}}$, resulting in a charge relaxation time in the order of a second. This is, on the contrary, well above the time scale of droplet motion on the capillary. Thus, charge redistribution at the surface of the droplets is essentially instantaneous in the case of acetone, but negligible in the case of n-pentane. This results in different electric field distributions. This is illustrated in Fig. 6.2, where the electric field distribution is shown for a highly conductive acetone and a low conductivity n-pentane droplet, respectively, 1 ms after the beginning of the voltage pulse. In the low conductivity case, the electric field strength within the droplet is significant, featuring a clear singularity at the tip of the capillary. In the high conductivity case, however, the electric field within the liquid vanishes. Thus, the electric force distribution for the two liquids differs significantly. In the case of acetone, the net force points away from the capillary. On the contrary, for n-pentane, the net force points towards the capillary. In the following, in order to emphasise the different droplet detachment characteristics and charging behaviour, the two liquids are analysed separately.

6.1.2 Numerical Setup

In order to allow for optical access to the capillary, the electrodes do not surround the capillary entirely, so that the geometry of the generator is not axisymmetric. However, the electric field distribution around the droplet is nearly so. Furthermore, experimental data on the detachment of droplets shows no signs of transverse oscillations. Therefore, the generator is modelled assuming axisymmetry in order to reduce computational costs.

The mesh resolution is chosen as $\Delta x = 2.5 \times 10^{-2}\,\mathrm{mm}$, corresponding to approximately 35 control points per primary droplet radius, resulting in total mesh size of 50 200 cells. The time step size is adaptive as described in Section 3.1.2, but limited from above to $3\,\mu s$, according to the stability limit for surface tension driven flow [37]. These values are chosen so that further

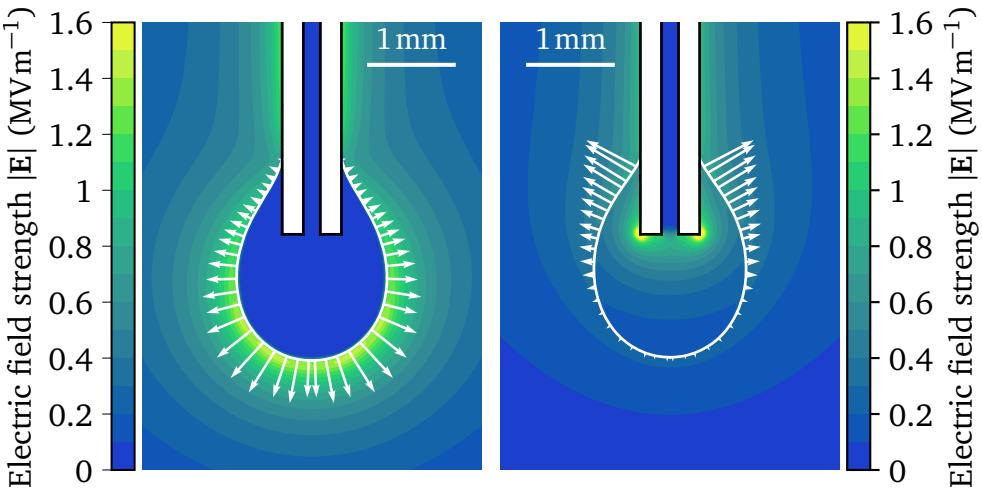

Figure 6.2: Electric field and surface force distributions for pendant droplets assuming different electric properties for the liquids (adapted from [83]). Left: acetone (high conductivity) droplet. Right: n-pentane (low conductivity) droplet.

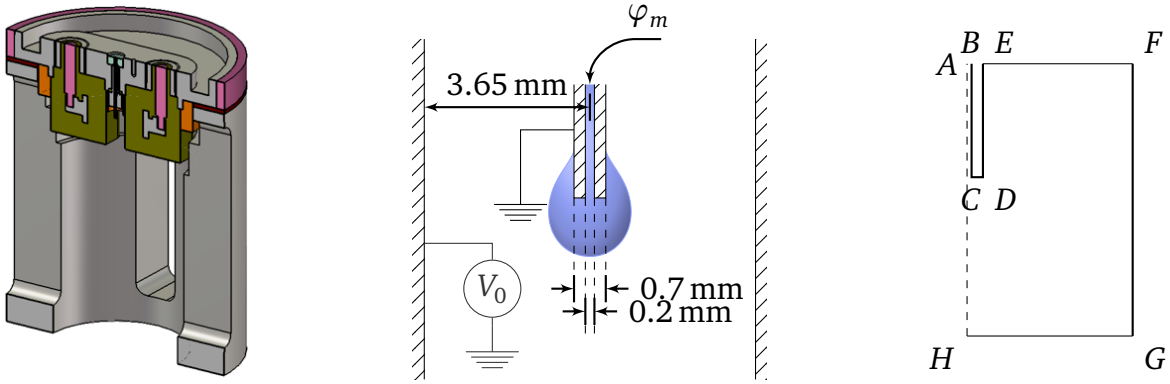

(a) **(b)** **(c)**

Figure 6.3: (a) Full model of the on-demand droplet generator. (b) Schematic view and main parameters of the simulation domain. (c) Notations for boundary conditions applied on the computational domain (see Table 6.1).

refinement does not influence the accuracy of results on the primary droplet. This resolution is furthermore sufficient to resolve the qualitative behaviour of the liquid thread and the satellite droplets appearing after detachment of the primary droplet.

6.1.3 Initial Conditions

In order to ensure that large electric fields are generated at the tip of the capillary, the capillary itself must be grounded. The choice of a metallic capillary is therefore natural. For the two test liquids considered here, acetone and n-pentane, this implies rather high wettability, with experimentally observed contact angles below 30°. As a result, pendant droplets wet the sides

Boundary	Variable				
	p_d	$\mathbf{u}$	α	Φ	ϱ_e
Inlet (AB)	$\nabla_n p_\mathrm{d} = 0$	$\mathbf{u}\cdot\mathbf{n} = \frac{\varphi_\mathrm{m}}{\rho\pi r_\mathrm{inlet}^2}$	$\alpha = 1$	$\nabla_n \Phi = 0$	$\nabla_n \varrho_\mathrm{e} = 0$
Capillary surface (BCDE)	$\nabla_n p_\mathrm{d} = 0$	$\mathbf{u} = 0$	$\nabla_n \alpha = \cos(\theta)$ * or $\alpha = \text{const.}$	$\Phi = 0$	$\nabla_n \varrho_\mathrm{e} = 0$
Free stream surface (EF)	$p_0 - \frac{1}{2}\lvert\mathbf{u}\rvert^2$	$\nabla_n \mathbf{u} = 0$	$\nabla_n \alpha = 0$ if $\mathbf{u}\cdot\mathbf{n} \le 0$ 0 otherwise	$\nabla_n \Phi = 0$	$\nabla_n \varrho_\mathrm{e} = 0$
Electrode surface (FG)	$\nabla_n p_\mathrm{d} = 0$	$\mathbf{u} = 0$	$\nabla_n \alpha = \cos(\theta)$ * or $\alpha = \text{const.}$	$\Phi = V(t)$	$\nabla_n \varrho_\mathrm{e} = 0$
Free stream surface (GH)	$p_0 - \frac{1}{2}\lvert\mathbf{u}\rvert^2$	$\nabla_n \mathbf{u} = 0$	$\nabla_n \alpha = 0$ if $\mathbf{u}\cdot\mathbf{n} \le 0$ 0 otherwise	$\Phi = 0$	$\nabla_n \varrho_\mathrm{e} = 0$

Table 6.1: Boundary conditions used for the numerical simulations of the droplet generator. The boundary conditions indicated with * indicate the contact angle boundary condition described in Section 3.3.3.

of the capillary. Droplet formation from a wettable capillary is a seldom studied problem [11]. A few words on the droplet formation are therefore in order.

For the mass flows and the capillary geometry considered here, the low capillary number $\mathrm{Ca} \approx 10^{-5}$ indicates that surface tension dominates over inertial effects. The pendant droplet growth is slow, so that it can be considered to be in static equilibrium at all times. Initially, the liquid wets only the bottom part of the capillary. The contact line is pinned at the edge of the capillary [12, 88]. As the droplet grows, the contact angle configuration allows the contact line to unpin and rise on the sides of the capillary. While initially small, the ratio of droplet weight to surface tension force increases until it reaches unity. At this time, the droplet, pinned to the tip of the capillary by surface tension, starts migrating down the capillary. During this process, since the contact angle and capillary radius are unchanged, the shape of the droplet remains essentially the same.

Droplet detachment is triggered for droplets during this regime of droplet filling. Thus, initial conditions for the droplet shape can be calculated directly using the Young-Laplace equation, as described in Section 2.2.1. This avoids simulating numerically the whole droplet filling process, which is a computationally expensive task due to constraints on the time step.

6.2 Detachment Dynamics of Pendant Droplets

The initial instant of electrically controlled detachment is chosen so that the tip of the primary droplet is located at the same distance from the capillary in the experiment and in the simulation. At that time instant, the mass flow is interrupted and the electrical pulse is triggered to destabilise the pendant droplet and force its detachment. The duration of the pulse is con-

strained by the requirement of charge-free droplet detachment. This can only be ensured if the voltage pulse is interrupted before the end of the detachment process, so that charge accumulated at the interface of the liquid may vanish. An example of experimentally measured voltage pulse is shown in Fig. 6.4. If the electric field within the droplet has not fully decayed at detachment time, the droplet will carry a net electric charge. Such a case is considered in Section 6.2.1.

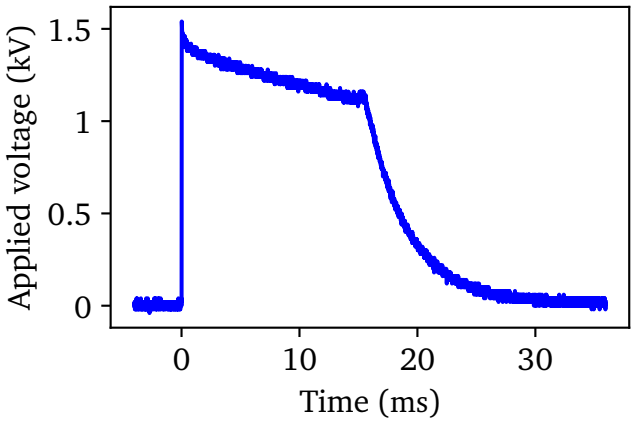

Figure 6.4: Measured profile of a 15 ms voltage pulse. The target voltage is 4 kV for a duration of 15 ms.

The detachment dynamics of different test liquids may significantly differ. For this reason, the dynamics of detachment of different test liquids are treated in separate sections. Section 6.2.1 illustrates the dynamics of a high-conductivity liquid, acetone, for which $\tau_e \approx 10\mu s \ll \tau_m$. Section 6.2.2 illustrates the dynamics of a low-conductivity liquid, n-pentane, for which $\tau_e \approx 1\,s \gg \tau_m$.

6.2.1 Acetone Droplet Detachment

As shown in Fig. 6.2, the electric force results in a single downwards kick to the droplet. Typical detachment dynamics are shown in Fig. 6.5. Once it reaches the tip of the capillary, the contact line is pinned at the edge of the capillary. When the surface tension is insufficient to restore the droplet into its pendant configuration, a neck forms and the droplet detaches from the capillary. The velocity of the droplet determines the location of neck formation, and therefore affects the amount of liquid left over. It should be noted that electric forces are typically insufficient to force large deformations of the droplets, but rather induce a uniform motion of the liquid bulk.

Simulation results for acetone droplet detachment in a nitrogen atmosphere at 20 °C, 1 bar, shown in Fig. 6.6, are in very good agreement with experimental results. The initial configuration, $t = 0$, corresponds to the beginning of the voltage pulse, driving the droplets downwards. The voltage pulse accelerates the droplet only for a short instant. It is interrupted long before the contact line reaches the tip of the capillary, at $t = 35$ ms. Although the contact line remains

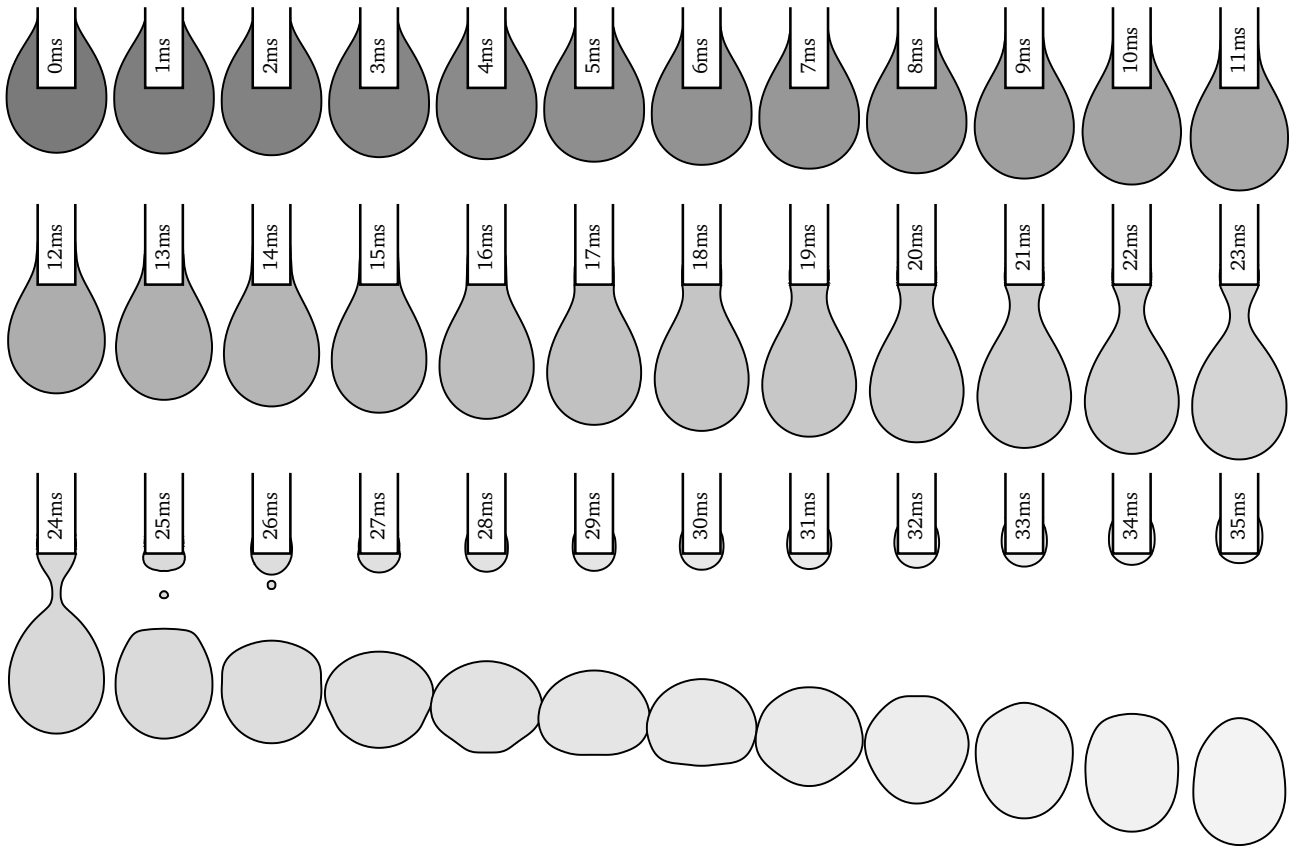

Figure 6.5: Detachment of a 3.8 μl acetone subjected to a 3 kV peak voltage pulse of duration 11.5 ms. Time instants are annotated with respect to the beginning of the voltage pulse. The satellite droplet visible at $t = 25$ ms and $t = 26$ ms merges into the pendant liquid before $t = 27$ ms.

pinned, the bulk of the droplet continues its downwards motion. The droplet elongates, eventually forming a neck around $t = 45\,\text{ms}$. Detachment occurs shortly after the formation of the neck and the droplet undergoes oscillations as it falls within the pressure chamber.

In the experimental footage only, a satellite droplet can be observed after detachment, falling after the primary droplet. A close inspection of the numerical results shows that a satellite droplet is formed, but it nearly instantly merges back with the remaining liquid at the tip of the capillary. In the experiment, the satellite droplet does collide with the remaining liquid, but bounces on its surface instead of merging. The absence of bouncing in the simulated dynamics is directly due to the use of the VoF method, which forces coalescence of liquids bodies as they make contact [78].

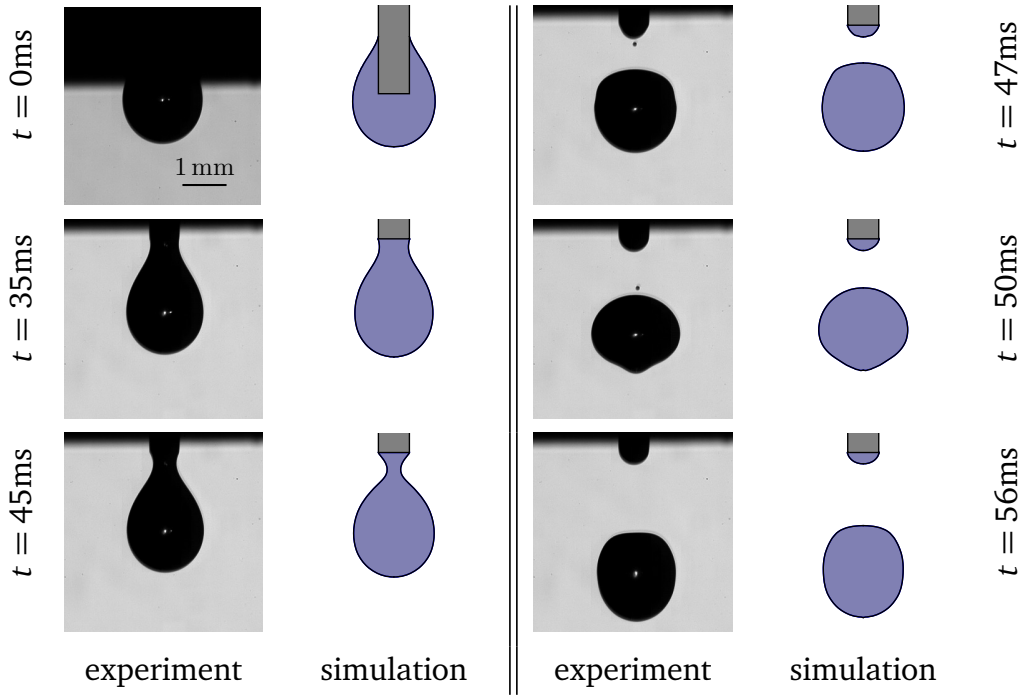

Figure 6.6: Detachment of a 3.7 μl acetone droplet subjected to a 11.5 ms, 2.1 kV peak voltage pulse [83]. The voltage pulse is interrupted before the detachment of the primary droplet. Experimental results courtesy of F. Weckenmann [129].

Detachment time and primary droplet volume

Test liquids are introduced through the capillary via a tube of significant length. Interruption of the mass flow to the capillary is therefore slightly delayed in the experiments. For completeness, two scenarios are considered for the detachment process: with continued mass flow and with instantly interrupted mass flow. The detachment times and detached volumes of acetone droplets as a function of the applied voltage are shown in Fig. 6.7a. At low voltages, the detachment time is quite sensitive to the applied voltage, but the dependency becomes nearly linear at higher voltages. The presence of the mass flow has a negligible effect on the detachment time

of the droplets for nearly all voltage values. For $\Phi = 2\,\mathrm{kV}$, however, detachment occurs only for nonzero mass flow. Unlike detachment time, the droplet volume, shown in Fig. 6.7b, differs depending on the mass flow scenario. As shown in Fig. 6.8, the reduced form of the volume difference to the detachment time hints that the volume difference may originate principally from the additionally introduced liquid in the continuous mass flow case. Due to the nearly identical trends in droplet detachment, the case of instantly interrupted mass flow is considered for the rest of this section.

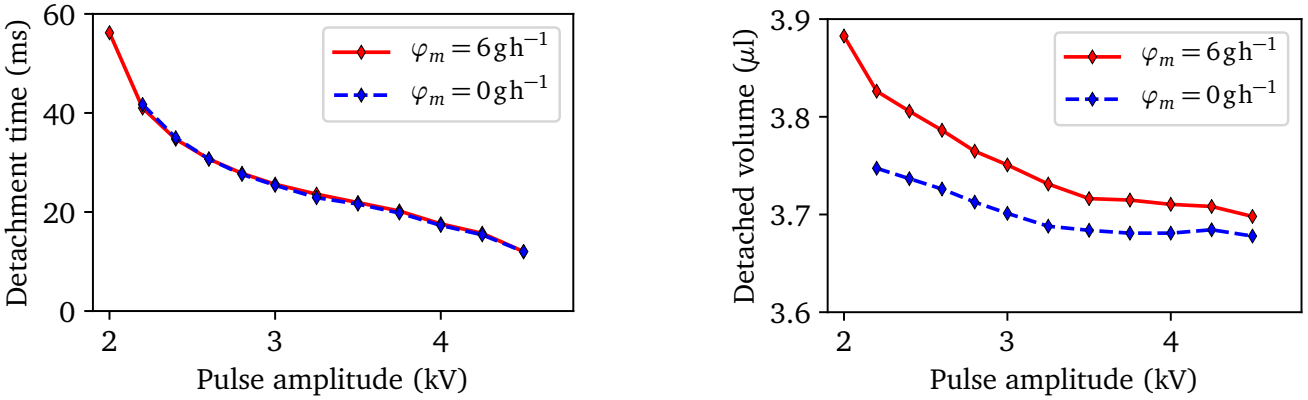

(a) Detachment time

(b) Primary droplet volume

Figure 6.7: Effect of pulse voltage on the detachment characteristics of the primary droplet for a $3.8\,\mu\mathrm{l}$ acetone droplet at 20 °C and 1 bar.

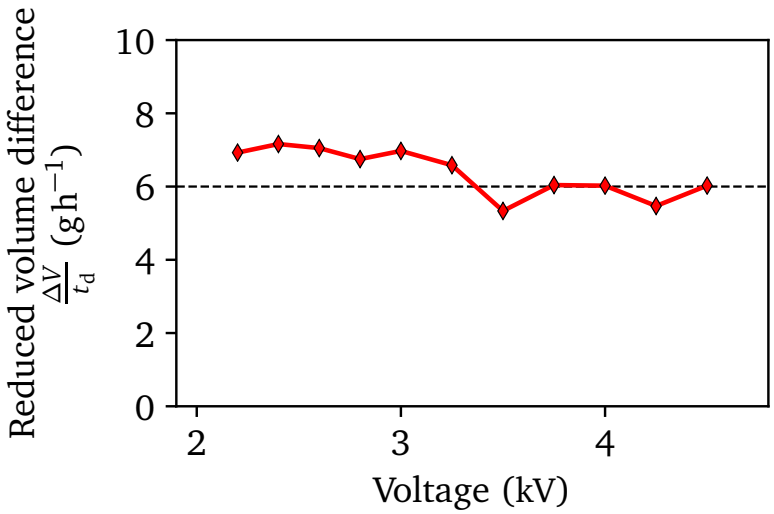

Figure 6.8: Volume difference introduced by the uninterrupted mass flow normalised by the detachment time.

Net droplet charge and induced forces

For the control of the droplet detachment process, the droplet charging dynamics and the magnitude of electrically applied forces are of interest. Due to the relatively high conductivity

of acetone, charge relaxation occurs nearly instantaneously. Thus, as illustrated in Fig. 6.9, the amount of free charge accumulating at the interface of the droplet follows the voltage profile exactly. As a result, the interruption of the voltage pulse, even shortly before detachment, is sufficient to ensure that the detached droplet is free of net charge. The presence of a tail in the voltage pulse profile due to capacitive effects in the voltage amplification apparatus could therefore be one of the main mechanisms resulting in the generation of charged droplets. The magnitude of the electric force driving the detachment also follows the voltage profile instantly regardless of the location on the capillary.

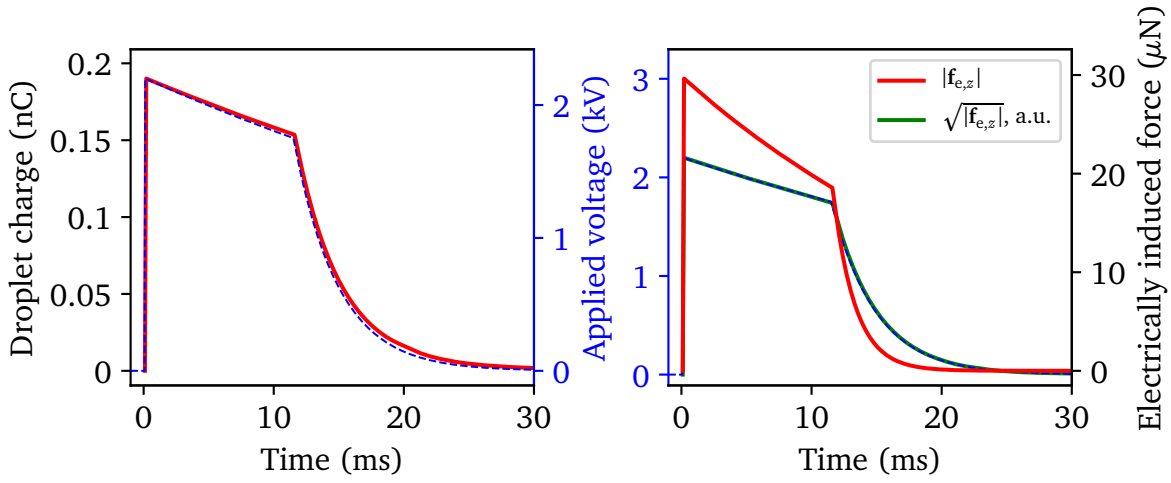

Figure 6.9: Net charge and electric force induced on the acetone droplet during the voltage pulse.

Oscillations of freely falling droplets

A second quantity of interest is the amplitude of droplet oscillations during droplet free fall. Since on-demand droplets are used for studies of phase transition, the magnitude of oscillations of the phase boundary should be kept as small as possible to prevent influence on experiments during the free fall. The transverse radius of droplets, corresponding to the maximal value of the radial coordinate of the droplet surface in the cylindrical coordinate system, is shown in Fig. 6.10. For the lower voltages, the radius of the droplet does not vary significantly during the voltage pulse. After the end of the voltage pulse, once the contact line is pinned, the droplet elongates, until the pinching of the neck causes the droplet to detach. After detachment, free falling droplets experience oscillations, originating from the propagation of capillary waves from the pinching point on the liquid thread. As shown in Fig. 6.10, the amplitude of oscillations depends on the applied voltage. The peak to peak amplitude of the first period of oscillation nearly doubles over the voltage range considered. Thus, the lowest voltage sufficient for detachment must be used in order to minimise droplet oscillations. Nevertheless, the amplitude of these oscillations is significant even at lower pulse voltages.

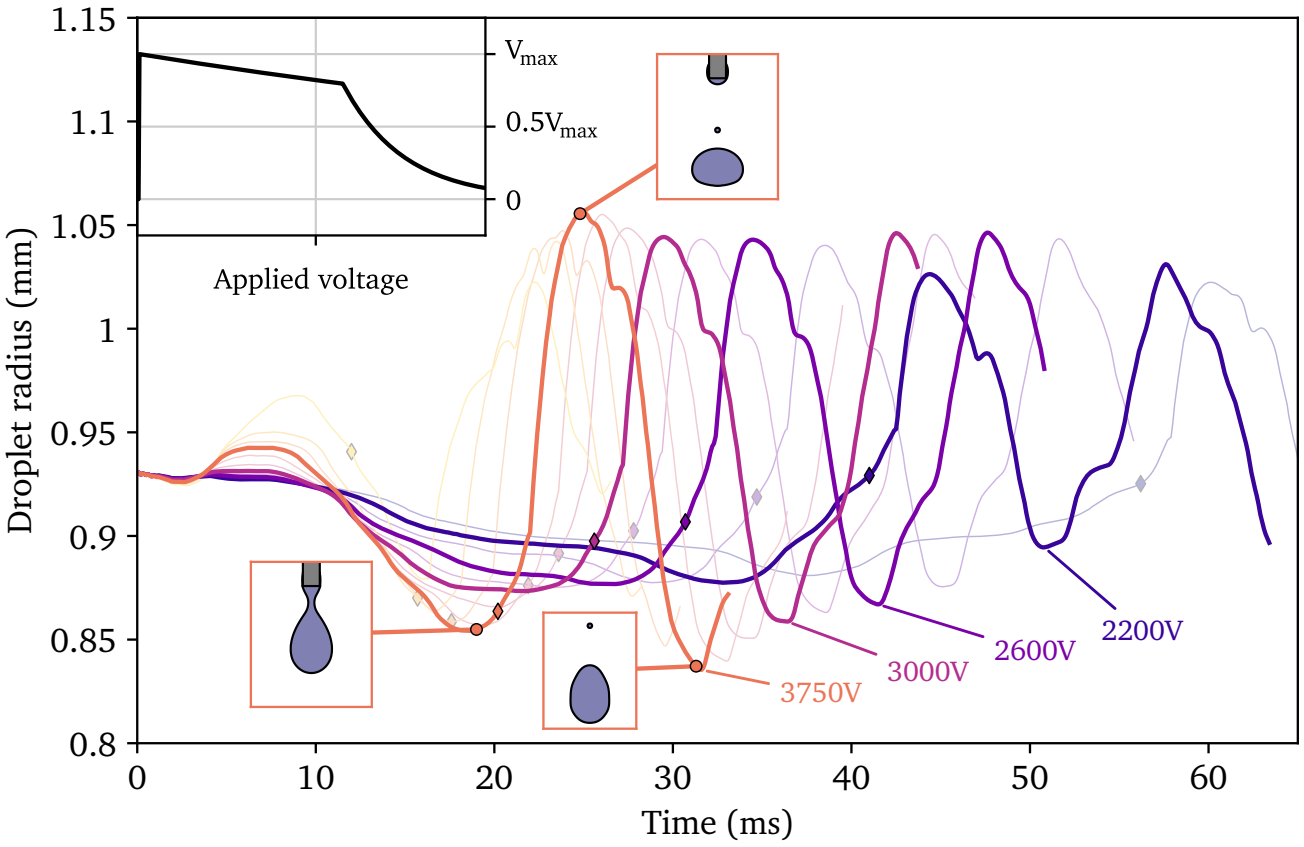

Figure 6.10: Transverse radius of droplet during detachment process. Markers indicate the detachment time for each curve. For better readability, only a few voltage cases are represented with solid lines. The voltage values are the same as in Fig. 6.7.

Dynamics of the liquid thread

The dynamical behaviour of the liquid thread at detachment time can be studied as a function of the electrode voltage, which correlates with the instantaneous pressure and velocity distribution at the tip of the capillary. The shape of droplets shortly before droplet detachment is shown in Fig. 6.11. The liquid thread formed between the primary droplet and the remaining pendant liquid exhibits two necks breaking successively. For lower voltages, the lower neck breaks first. The remaining liquid thread is accelerated upwards before the break up of the second neck. As a result, the satellite droplet formed from the liquid thread moves upwards, towards the pendant liquid. In case of collision, the satellite droplet may either merge with the pendant liquid or bounce on it. Conversely, at higher voltages, the top neck breaks first, so that the resulting satellite droplet follows the primary droplet in its fall. It may eventually catch up with it [139, 140]. The maximum applied voltage for which no falling satellite droplet generation is expected can be identified from simulations as about 3 kV.

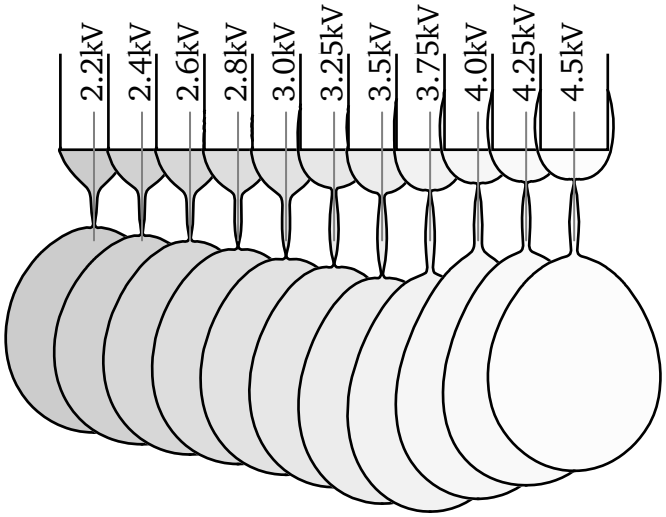

Figure 6.11: Dynamics of the liquid thread at the time of detachment [83].

Generation of charged droplets

As shown in Fig. 6.9, the amount of net charge induced at the surface of the acetone droplet by external electric fields is nearly proportional to the instantaneous voltage. The case of an electrical pulse interrupted after the detachment of the droplet is considered in the following. For this purpose, a flat voltage pulse of duration 26 ms is applied, leading to the detachment of the pendant droplet at $t = 21.8$ ms, i.e. before the end of the voltage pulse. The total induced charge in the liquid is shown in Fig. 6.12. As the droplet nears detachment, the free surface area of the liquid increases. Thus, the amount of surface charge increases until detachment. At the end of the voltage pulse, the free charge in the liquid remaining at the tip of the capillary vanishes quickly. It is replaced by a charge of opposite sign, mirroring the net charge of the

free falling droplets. The net charge in the detached droplets, primary and satellite, remains constant during the fall since the nitrogen atmosphere electrically insulates the droplets. The charge in the pendant liquid vanishes as the distance from the detached droplet to the capillary increases. Figure 6.13 illustrates the apparition of the mirror charge at the capillary. The net charge in the pendant liquid takes the opposite sign of the detached droplet charge. The net charge of both the primary and satellite droplets remain constant.

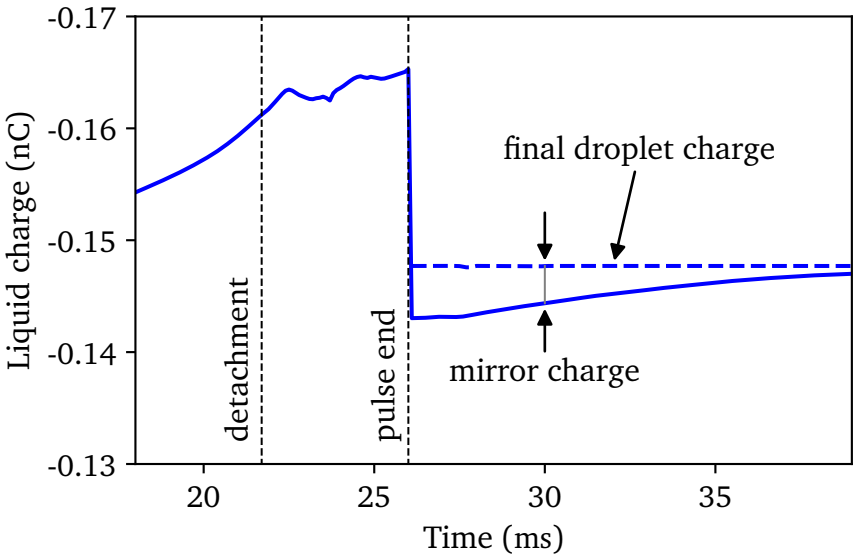

Figure 6.12: Total free charged induced in the liquid during the detachment of a charged droplet (adapted from [83]).

6.2.2 N-Pentane Droplet Detachment

Unlike acetone, n-pentane is a liquid with relatively low polarity, $\varepsilon_r = 1.83$, and low conductivity, $\kappa = 20\,\mathrm{pS\,m^{-1}}$. The different electrical properties lead to strongly different electric field and forces distributions in the droplet compared to the case of acetone, as shown in Fig. 6.2. Since both the amount of net charge and bound charge at the interface induced by a given voltage are lower than in the case of acetone, the magnitude of induced electric forces by a given voltage is expected to be much lower. This is observed experimentally, as the voltage required for the detachment of n-pentane is much larger than in the case of acetone. The simulated dynamics of a n-pentane droplet are shown in Fig. 6.14. The behaviour of the droplet on the capillary during the applied voltage pulse is clearly different from that of an acetone droplet. Instead of being accelerated downwards, the droplet is accelerated towards the capillary by the electric forces. After the interruption of the voltage pulse, the surface tension acting on the droplet is insufficient to compensate for its weight. The droplet is therefore accelerated downwards by its own weight, triggering the detachment. The simulation is in good qualitative agreement with

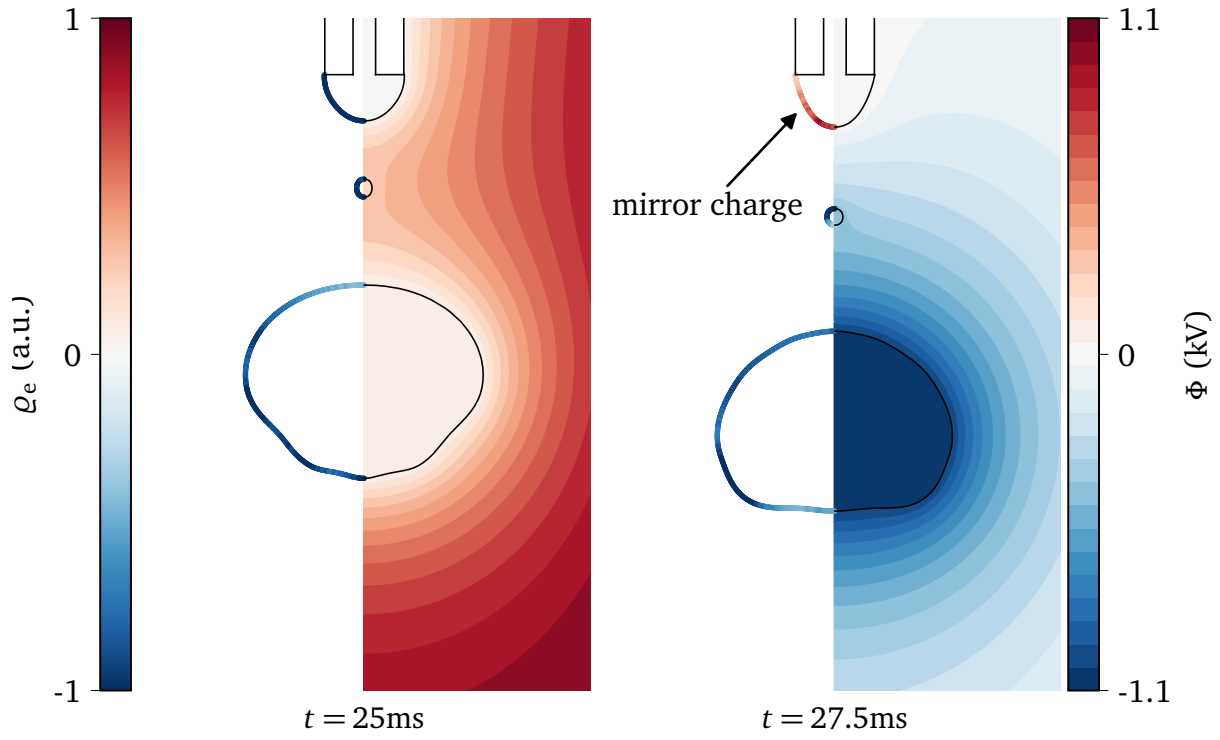

Figure 6.13: Electric charge (left half of each picture) and potential distribution (right half of each picture) of a charged acetone droplet before and after voltage switch off (adapted from [83]). The electric charge density is represented here as a surface density at the surface of the liquid (thin coloured lines). After voltage switch off, the charge in the pendant liquid is replaced by a charge mirroring that of the droplets.

experiments, as shown in Fig. 6.15. The discrepancy in the detachment times is likely due to the lack of wettability data for the capillary surface.

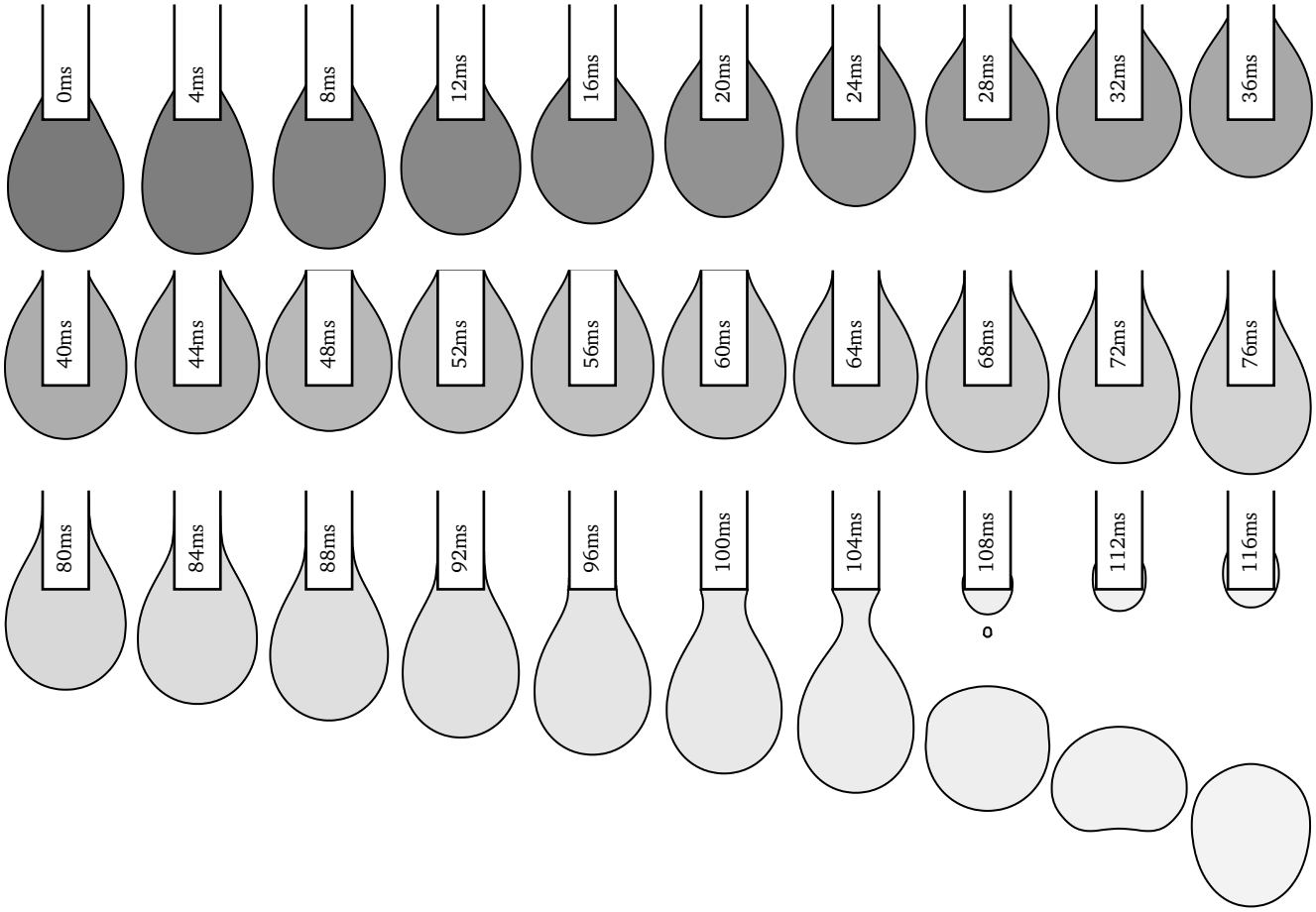

Figure 6.14: Detachment of a 3.73 μl n-pentane droplet subjected to a 3.5 kV peak voltage pulse of duration 26.5 ms. Time instants are annotated with respect to the beginning of the voltage pulse. The satellite droplet visible at $t = 108$ ms merges into the pendant liquid.

The difference in the dynamics of droplet detachment is related to the field pattern around the capillary. The electric field inside of the droplet is not screened away by surface charge (as in the case of acetone), so that the field singularity at the capillary edge remains. The electric force distribution acting on the droplet is therefore skewed towards repelling the contact line away from the tip of the capillary. Since the effect originates from the singular fields at the tip of the capillary, it depends on droplet position. The dependency of the net force on the position on the capillary is illustrated in Fig. 6.16 for static pendant droplet shapes. For pendant droplets at low positions on the capillary, the net force drives the droplet towards the capillary. A maximal value is obtained shortly before the contact line reaches the tip of the capillary. For droplets higher on the capillary, the net force reverses direction, so that droplets are forced downwards by electric forces, similarly to conductive liquids. Yet, this method of detachment

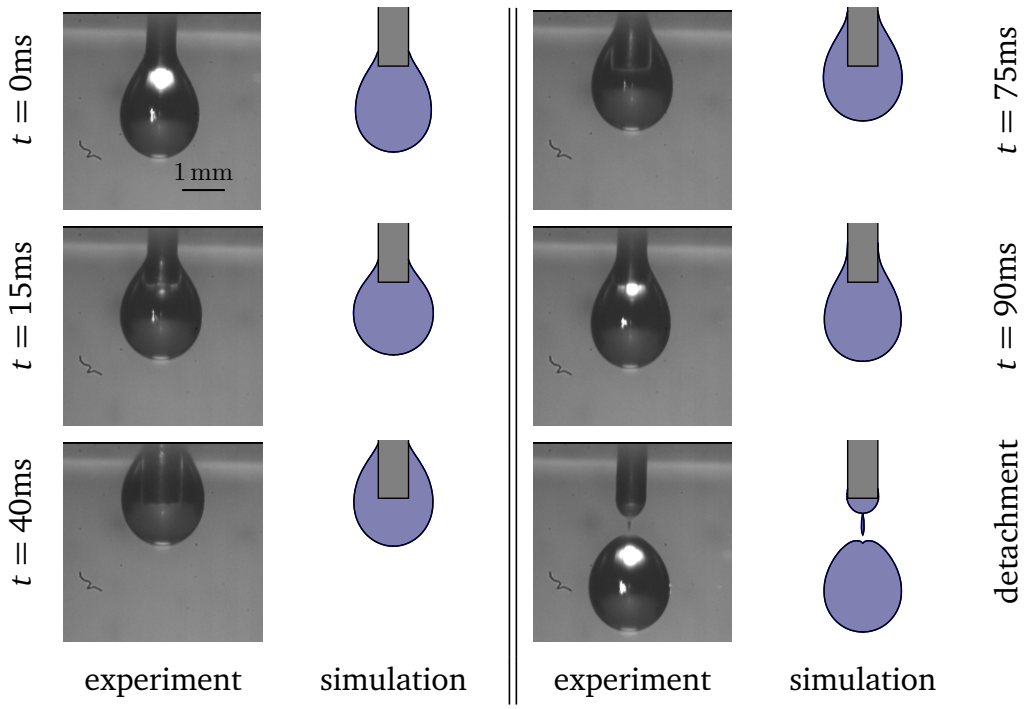

Figure 6.15: Comparison of the simulated n-pentane dynamics with experiments [83]. Experimental results courtesy of C. Steinhausen.

for low conductivity liquids is impractical as the net force vanishes quickly as the droplet starts moving down the capillary.

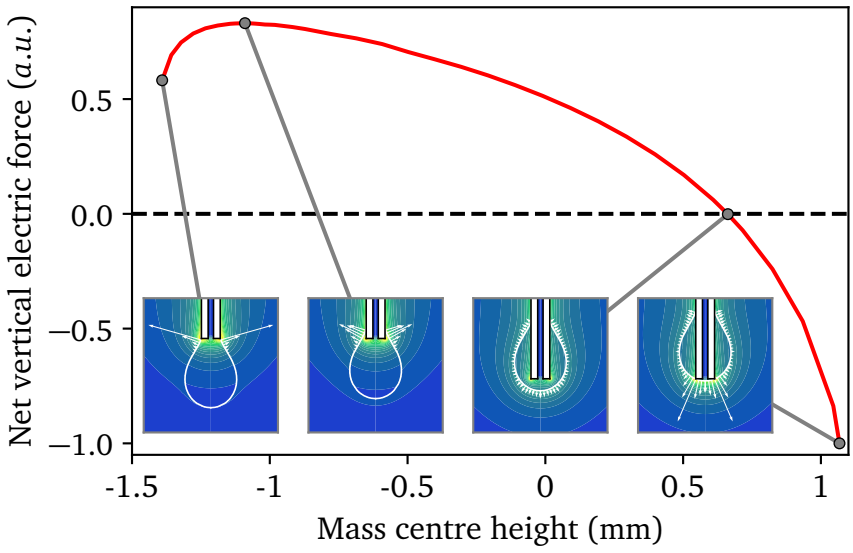

Figure 6.16: Net force acting vertically on an n-pentane droplet in function of the height of its mass centre on the capillary. The inset pictures show the field and force patterns around the droplets at specific locations on the capillary.

Detachment times are significantly longer than for the case of acetone due to the two step detachment process. Their dependency on the applied voltage is shown in Fig. 6.17a. While

the detachment time decreases nearly linearly with increasing voltage, the range of variation is relatively small. Figure 6.17b shows the motion of the mass centre of the droplet over time. Larger impulses result in faster motion downwards, but the effect is counterbalanced by the larger travel distance of the droplet on the capillary.

Due to the low conductivity of n-pentane, charge accumulates at the surface of the droplet slowly during the voltage pulse. However, charge dissipates also slowly before detachment, so that, while of small magnitude, detached droplets carry some net charge, no matter how short the voltage pulse is. Since the rate of charge accumulation is proportional to the electric field, the net charge of droplet scales nearly linearly with the applied voltage, see Fig. 6.17c.

The oscillations of droplets during and after the voltage pulse are shown in Fig. 6.17d. The voltage pulse induces oscillations of the droplets as they ascend on the capillary. However, these disappear quickly as droplets descend the capillary. The amplitude of oscillations after the detachment is therefore nearly independent from the applied voltage.

Due to the low dependency of detached n-pentane droplet dynamics on the applied voltage at the exception of net droplet charge, similarly as for acetone, the lowest voltage producing detachment should be used in experiments.

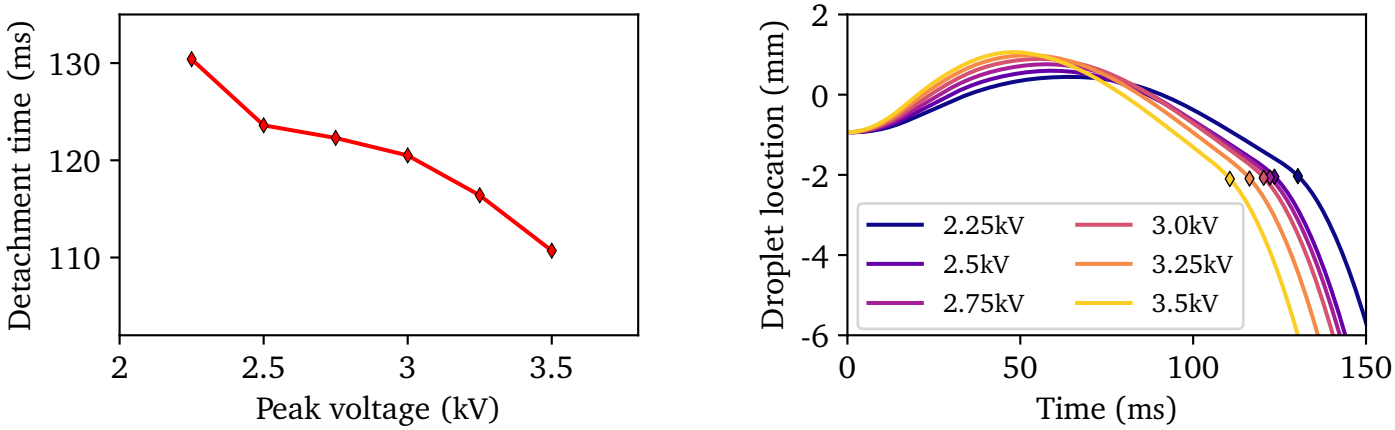

(a) Detachment time

(b) Droplet location

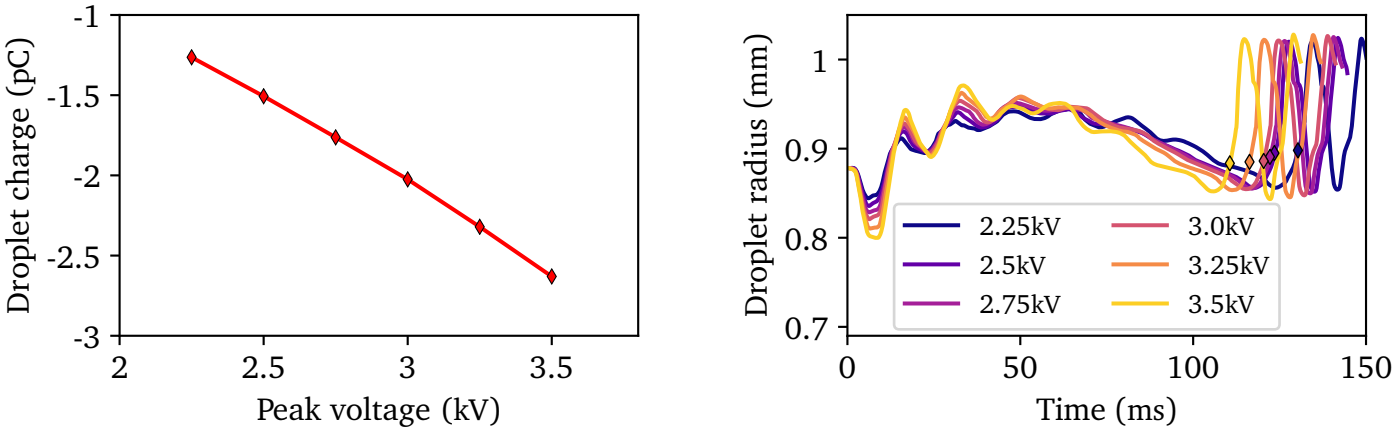

(c) Net droplet charge

(d) Droplet radius

Figure 6.17: Droplet detachment characteristics for single droplets subjected to a 26.5 ms voltage pulse. Markers indicate the time of detachment for the different applied voltages.

7 Transient Electrosprays

7.1 Problem Description

Electrospray atomisation refers to the electrically induced detachment of droplets from conductive liquids. Different modes of electrospraying can be observed depending on experimental parameters, such as applied voltage, electrode geometry and liquid flow rate [17, 54, 123]. In the dripping mode, the application of electric fields results in an apparent reduction of the surface tension of the liquids. For liquid continuously introduced from a capillary, this produces periodic detachment of droplets whose size may exceed that of the capillary [17]. For larger applied electric fields, thick jets are formed instead. Fragments of these jets may detach, in the form of liquid spindles [54], which may later break down into a number of droplets. In the cone-jet mode, the liquid interface locally approaches a conical shape, from the tip of which a thin continuous jet streams. This jet may remain simple and break down due to varicose or kink instabilities. Ramified jets may also be formed, spraying droplets in random directions around the main jet [54]. In the case of the spindle mode and cone-jet mode, emission of jets may also occur simultaneously from different regions of the same meniscus.

The cone-jet mode of electrospray is of particular interest for many technical applications. In biomedical applications, electrohydrodynamic atomisation is utilised for powder production [5], micro encapsulation [26], micro mixing [4] and nanostructured particles [138]. The technique is also used for the production of monodisperse nanoparticles [62], and as an ionisation technique for mass spectrometry [32, 45]. In space propulsion applications, electrosprays are used for the production of charged droplets in efficient colloid thrusters [39, 122]. One of the main advantages of the electrospraying technique is the possibility of producing particles with specific properties (charge, size).

Depending on the experimental parameters, the size of generated microdroplets can be modulated over a large range of droplet sizes, down to submicron sizes [17, 113]. Furthermore, the cone-jet mode allows to produce sprays with narrow size distributions [22, 41, 110, 111, 112, 113] for primary droplets. In the presence of satellite droplets, a bimodal distribution may be obtained instead [111]. The different characteristics (size, charge to mass ratio) [38, 40] of the primary and satellite droplets lead to significantly different off axis downstream behaviour, eventually separating satellite and primary droplets [23, 111].

Under the assumption of perfect conductivity of the liquid, Taylor [114] calculated that a conical shape with half-angle 49.3° can balance electric stresses and capillary forces. This conical

shape forms a limit past which a thin axial jet is formed. In the presence of the jet, a conical shape is preserved sufficiently far from the tip. However, the cone half-angle deviates from the static case considered by Taylor [23, 90, 107].

Significant research has been performed on the scaling of stable cone-jet electrosprays [22, 15, 23, 24, 41, 130], to produce scaling laws relating the electrospray current with the flow rate. Scaling laws have been proposed for the droplet size. However, the accuracy of the reported measurements is insufficient to distinguish between different scaling laws proposed to characterise the same electrosprays [2]. More recently, significant advances on the scaling of initial ejections rather than steady electrosprays have been made [18, 42, 85]. Of interest is particularly the scaling law derived in [18], which relates the diameter and charge of the initial ejection with a universal law depending only on liquid properties. This scaling law is verified by numerical simulation means. In [42], different scaling laws are derived and verified with experiments and numerical simulations. The difference between the scaling laws is attributed in [42] to the use of different models for free charge in the jet. A similar conclusion is draw in [85], where a Poisson-Nernst-Planck model is used for the electrokinetics, producing another set of scaling laws over a larger range of material parameters than in [18].

A number of numerical studies of electrosprays in the cone-jet mode have been performed [21, 63, 96, 131, 133]. Many of the numerical models predict droplet diameters in agreement with experimental results. However, simplified models for the dynamics of free charge in the jet have been used in [63, 131, 133]. In [18, 96], only surface charge was considered, which was shown in [42] to improperly represent free charge in the jet. In these works, only either the first droplet or the steady state of the electrospray have been studied.

The goal of this chapter is to extend previous work on the onset of electrosprays, by considering the dynamics of transient electrosprays, and to verify some existing scaling laws. The chapter is divided into two parts. In the first part, electrosprays from sessile drops are considered and characterised for a number of test liquids. This configuration reduces the number of experimental parameters, by removing the influence of liquid flow rate in particular. Additionally, the characteristics of the electrosprays thus formed are found to be nearly independent from the applied voltage [42, 82] In the second part, electrosprays from dripping heptane at various flow rates are considered and compared to experimental data from [113].

7.2 Electrosprays from Sessile Droplets

7.2.1 Numerical Setup

In this section, the onset of electrospray from sessile droplets is considered, as shown in Fig. 7.1. This configuration allows for the generation of cone-jets from sessile droplets by applying a

constant voltage between the two plate electrodes. The numerical simulations are performed for different test liquids at different voltages.

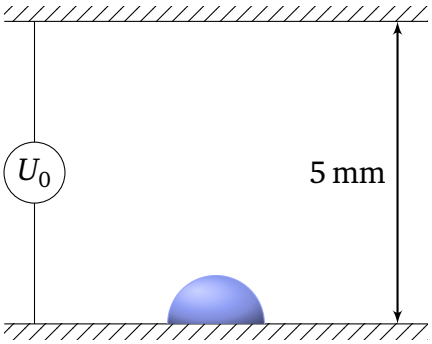

Figure 7.1: Configuration of the simulations of transient electrosprays from sessile drops. The typical sessile drop volume used in simulations is $1\,\mu$l. Typical applied voltages resulting in cone-jet electrosprays are U_0 =5–6kV.

As, in the proper range of experimental parameters, the cone-jet mode is axisymmetric [17], the numerical simulations are performed assuming axisymmetry. This simplification greatly reduces the computational costs of electrospray simulations. One limitation is that off axis dynamics of the atomised droplets cannot be simulated. Nevertheless, the simplification is not expected to affect the dynamics of the jet nor droplets right after atomisation, since the droplets are typically thrown off axis only at some distance downstream from the jet [111].

Typical electrospray apparatus have millimetric to centimetric size, but produce microdroplets in the micrometer range. In addition, the length of the jet formed at the onset of the electrospray may reach multiple millimetres before the first atomisation. Thus, the numerical simulation of electrosprays must be performed over a large region compared to the atomised droplet size. Sufficient spatial resolution can be obtained by means of adaptive mesh refinement, as described in Section 4.1. Load balancing capabilities are particularly beneficial, as refined regions travel through the domain along with the jet and atomised droplets.

The region of interest for mesh refinement is chosen as the interface between the test liquid and surrounding air. This choice minimises errors arising from the diffuse nature of the VoF interface, while ensuring that all microdroplets as well as the jet are spatially resolved. Interface cells are identified as cells with at least one neighbour whose volume fraction α differs by 0.1 in absolute value. The refined region corresponds to cells at a distance up to $n = 6$ cells from an interface cell. A buffer of $n = 6$ cells at each level is utilised to ensure gradual coarsening of the mesh away from the interface.

In the following, the base mesh (level 0) is chosen with a mesh parameter $\Delta\rho = \Delta z = 25\,\mu$m. Up to 7 levels of refinement are used for adaptation, so that $\Delta\rho = \Delta z = 0.195\,\mu$m at the finest level.

Adaptive mesh refinement provides an adequate spatial resolution while maintaining the number of degrees of freedom low ($<$ 0.5 million) compared to static refinement ($\approx$ 10 mil-

lion). However, as the largest observed velocities occur in the vicinity of the interface, the CFL condition still restrains the time step to small values. As the simulation of the initial transients does not require a particularly fine mesh, the simulation is initialised with 3 levels of refinement. Then, the number of levels of refinement is slowly increased to its maximal value before the onset. The maximal refinement level is controlled by the maximum electric field magnitude observed in the domain. As initial deformations of droplets are slow compared to the charge relaxation time, this criterion ensures that a sufficient refinement of the interface is obtained before electrospray onset, independently of the initial conditions and test liquid.

The mesh grid used in the simulation of a methanol electrospray is depicted in Fig. 7.2. Due to the extreme aspect ratio of the jet, refinement along the jet only occurs in a thin region around the symmetry axis. The refinement around single droplets is visible on the top part of the jet. Figure 7.2b reveals the size of cells at the finest level, which corresponds to approximately 40 cells per primary droplet radius.

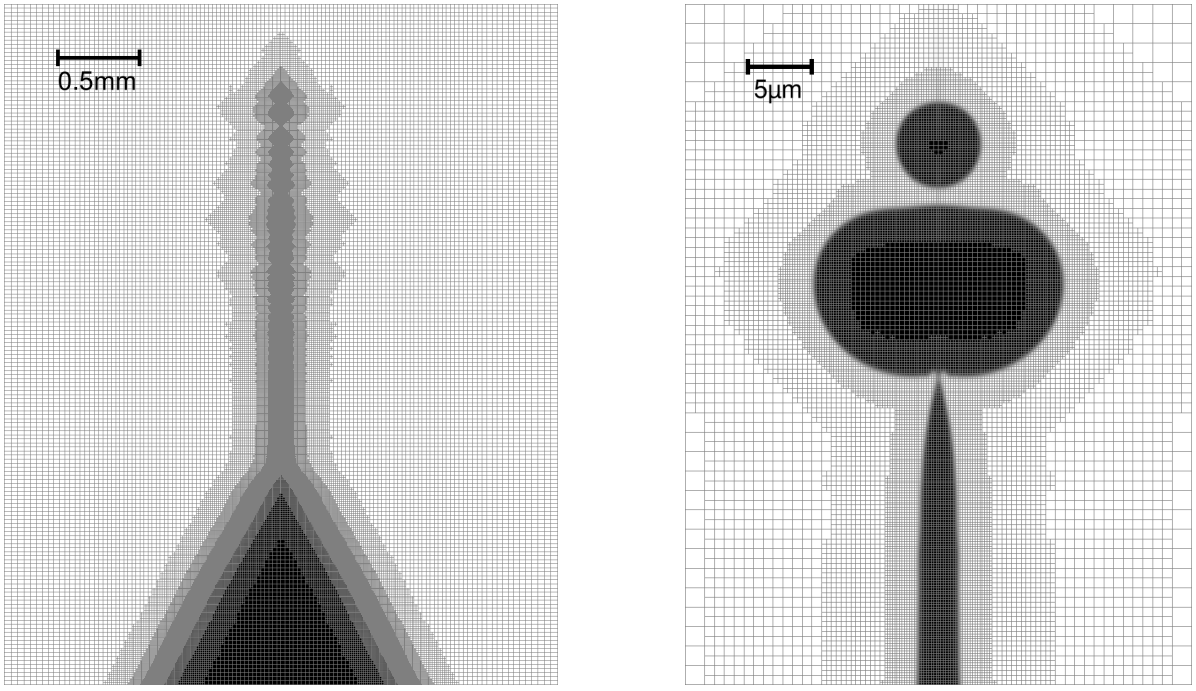

(a) **(b)**

Figure 7.2: Mesh refinement at the fluid-fluid interface in the case of a methanol cone-jet. The meshes are mirrored with respect to the symmetry axis only for the visualisation. (a) Refinement around the whole droplet and jet. (b) Close view at the tip of the jet.

Simulations were performed on a high-performance cluster with MPI parallelisation. Each simulation was performed on 2 nodes equipped with “Intel Xeon x5650 2.66GHz” processors, using 12 cores per simulation. Even with the optimisations applied to reduce computational costs, the simulation times are considerable. The typical simulation time until the first ejection

is 24 h. However, as the jet elongates, the number of degrees of freedom quickly increases. In addition, the CFL condition imposes an increasingly strict constraint on the maximal time step, as the initial droplet in particular is accelerated to high velocities by the electric field after detachment. Thus, depending on the number of following droplet ejections considered, the simulation times may reach several weeks. In the following, numerical simulations were interrupted when either the initial ejection reached the opposite electrode, or after $\approx$ 14 days of computation.

7.2.2 Electrospray Onset

When the voltage is applied, the vertical electric field drives elongation of the sessile drop towards the opposite electrode. The increased curvature of the drop leads to an local electric field enhancement at its tip. Thus, both the magnitude of the surface tension forces and electric forces are increased at the tip of the droplet. When the applied voltage is insufficient, the surface tension forces eventually compensate the electric forces. The sessile drop then undergoes oscillations damping towards its equilibrium shape in the applied electric field [33]. For a sufficiently large voltage, however, the local electric field reaches a critical value. The bulk of the droplet undergoes the initial elongation towards the electrode. The electrospray onset occurs when the droplet approaches a conical shape. A thin jet then streams from the tip of the drop with a velocity much larger than that of the bulk of the drop. The initial transients leading the onset of the electrospray are illustrated in Fig. 7.3 for the case of a methanol electrospray. In this specific case, the elongation of the droplet does not introduce any motion of the contact line. The whole droplet approaches a conical shape before the jet streams from the tip of the droplet. Here, the jet streams before the droplet as a whole takes a perfect conical shape.

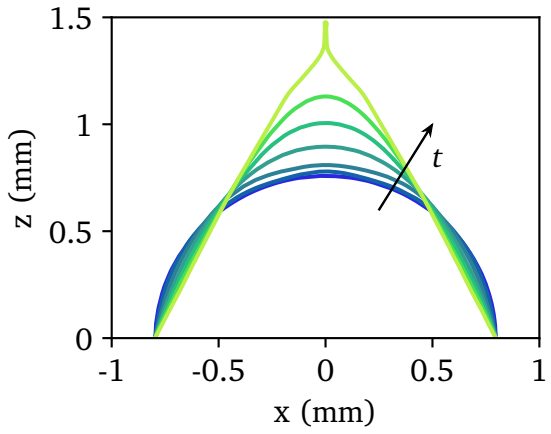

Figure 7.3: Simulated deformations of a 1 μL methanol droplet subjected to $U_0 = 5$ kV with an electrode spacing of 5 mm. Different, equally spaced, time instants are shown, before the emission of the first electrospray droplet.

Simulation results for two different test liquids subjected to 5 kV with an electrode spacing of 5 mm are shown exemplarily in Figs. 7.4 and 7.5. There, the liquid air interface and the distribution of electric fields at different time instants as the electrospray develops are depicted. By visual inspection, the droplet sizes and rate of ejection differ substantially. The first ejection differs in radius by a factor of three. In addition, in the case of heptane, the size of the following ejections increases significantly over time.

7.2.2.1 Dynamics of Droplet Atomisation

For both the heptane and the methanol jet shown in Figs. 7.4 and 7.5, the bulk of the droplet is free of electric fields. However, due to the finite liquid conductivity, charge migration effects cannot compensate the external field in the jet. The nonzero tangential electric fields acting on the charged surface of the jet drive the streaming of the jet [18, 24]. As the jet elongates, varicose instabilities are the main mechanism producing the atomisation of the microdroplets. Two types of droplets are atomised. The detachment of the large primary droplets often produces smaller satellite droplets. This is illustrated in Fig. 7.6. The liquid threads connecting primary droplets to the jet pinch on either end, leading to different satellite droplets dynamics. Thus, some satellite droplets immediately merge with neighbouring primary droplets while others remain.

Due to the complex dynamics of the jet, the successive ejections of primary droplets are not equally spaced. In some cases, a segment of the jet is detached before breaking up into multiple droplets. Such an event is illustrated in Fig. 7.7, where two primary droplets are produced from a single ejection from the jet. In the following, due to the complex interactions between atomised droplets and the jet, the successive ejections are characterised only from their state at the time of detachment from the cone-jet. For simplicity, downstream splitting and merging of droplets is not considered during the post processing step.

7.2.3 Scaling of the First Ejection

In order to validate the simulation approach, the size and charge of the first ejection for a number of test liquids is compared to the universal scaling law derived in [18]. Given the characteristic viscous length $l_\mu = \mu^2/\rho\gamma$, the charge q and radius r of the first ejected droplet, the dimensionless parameters $q^* = q/\sqrt{\varepsilon_g \gamma l_\mu^3}$ and $r^* = r/l_\mu$ are defined. With these parameters, the scaling law resulting from dimensional analysis reads $q^* \propto (r^*)^{\frac{3}{2}}$, where the associated proportionality constant is independent from the liquid material properties. Simulations for 21 different liquids corresponding to a broad range of electromechanical properties, summarised in Table 7.1, are performed. This choice is motivated by their use in experiments reported in the relevant literature. In each simulation, the dimensionless charge and radius parameters for

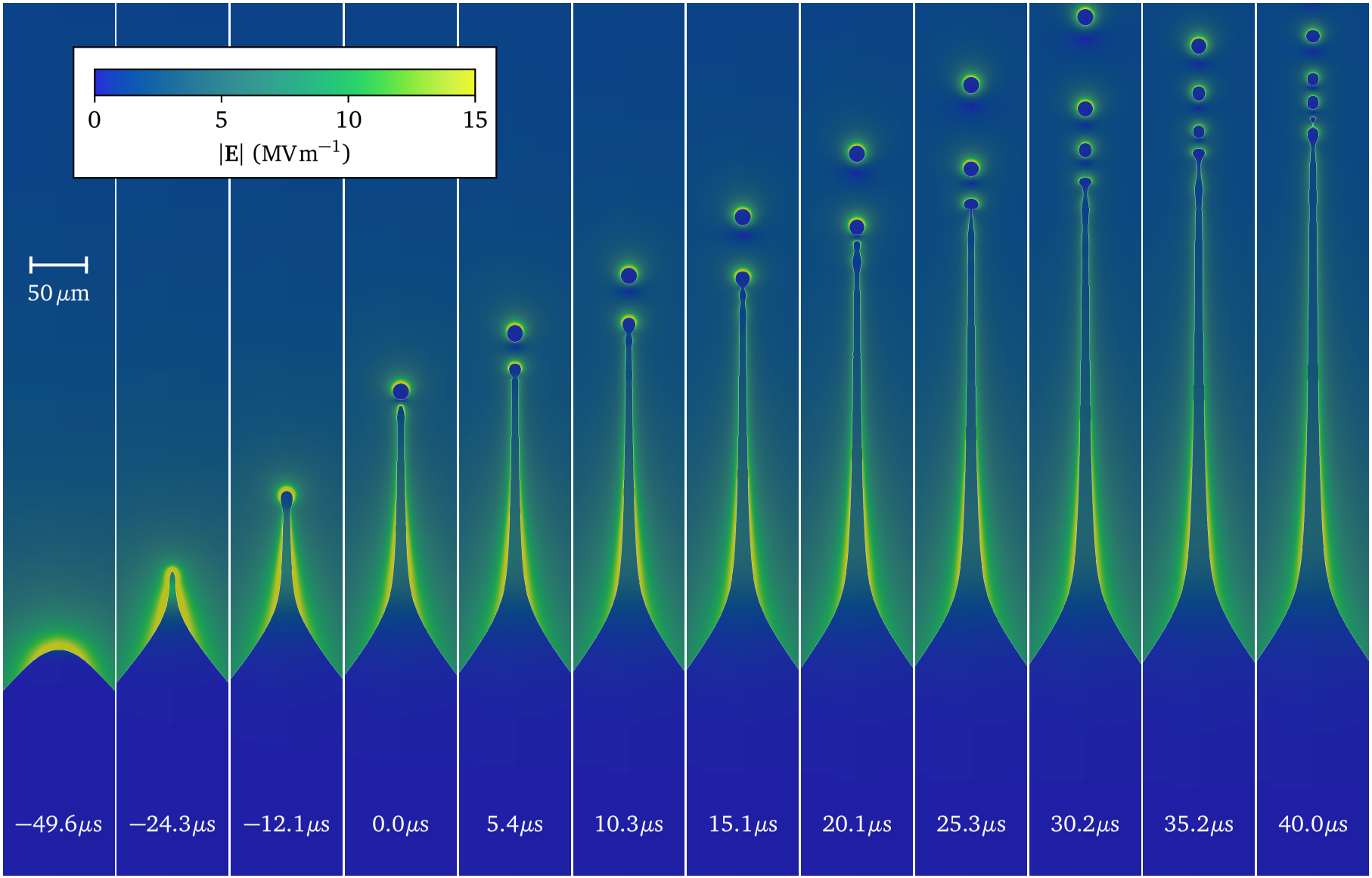

Figure 7.4: Onset and first ejections of a methanol (see Table 7.1) electrospray ($U_0 = 5\,\mathrm{kV}$, $V = 1\,\mu\mathrm{L}$). The electric field distribution is depicted. In order to facilitate the identification of satellite droplets, the interface is highlighted with thin white lines.

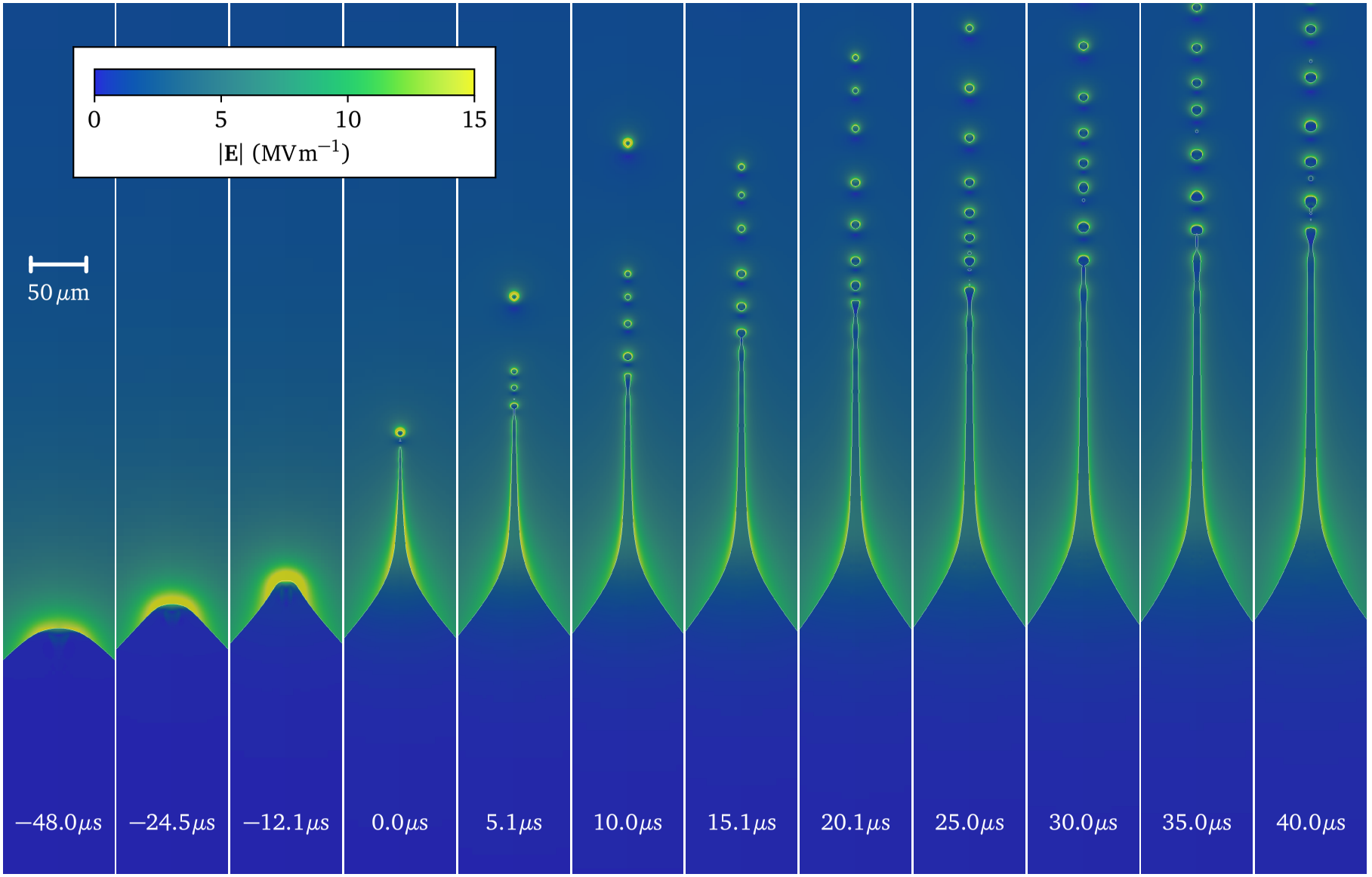

Figure 7.5: Onset and first ejections of a heptane2 (see Table 7.1) electrospray ($U_0 = 5\,\mathrm{kV}$, $V = 1\,\mu\mathrm{L}$). The electric field distribution is depicted. In order to facilitate the identification of satellite droplets, the interface is highlighted with thin white lines.

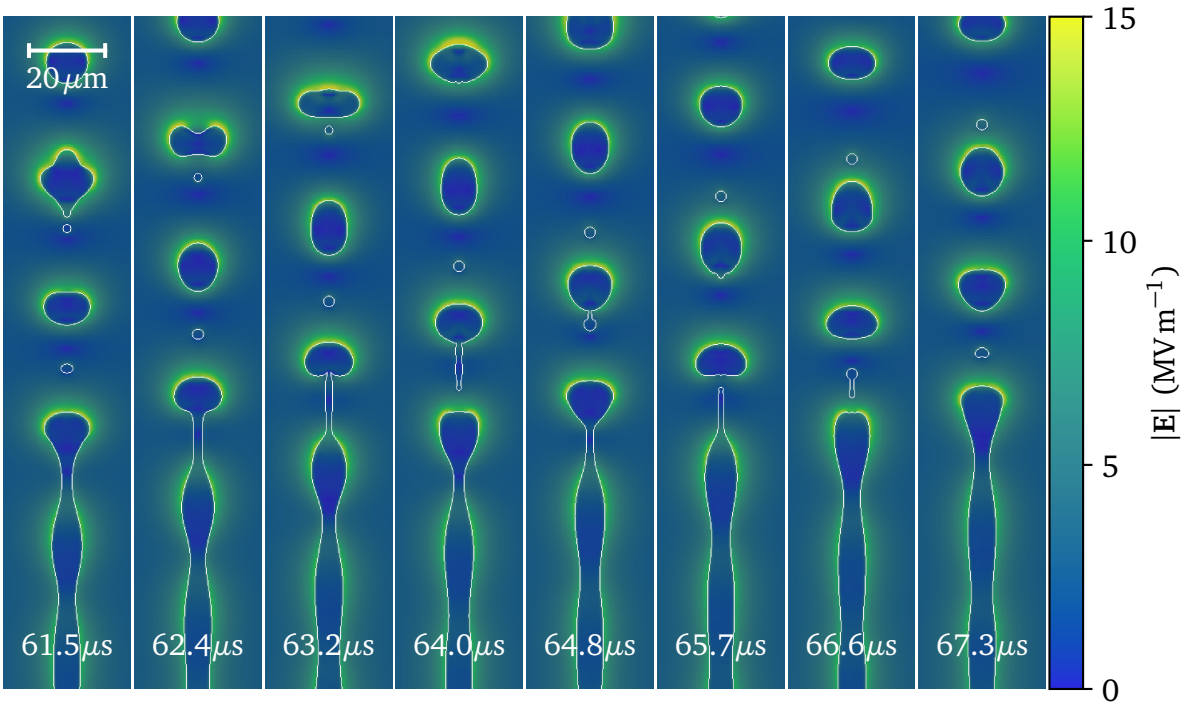

Figure 7.6: Successive ejections of a heptane2 (see Table 7.1) electrospray. The satellite droplet formed at $t = 64.8\,\mu s$ immediately merges with the preceding primary droplets. The satellite droplet formed at $t = 66.6\,\mu s$ remains.

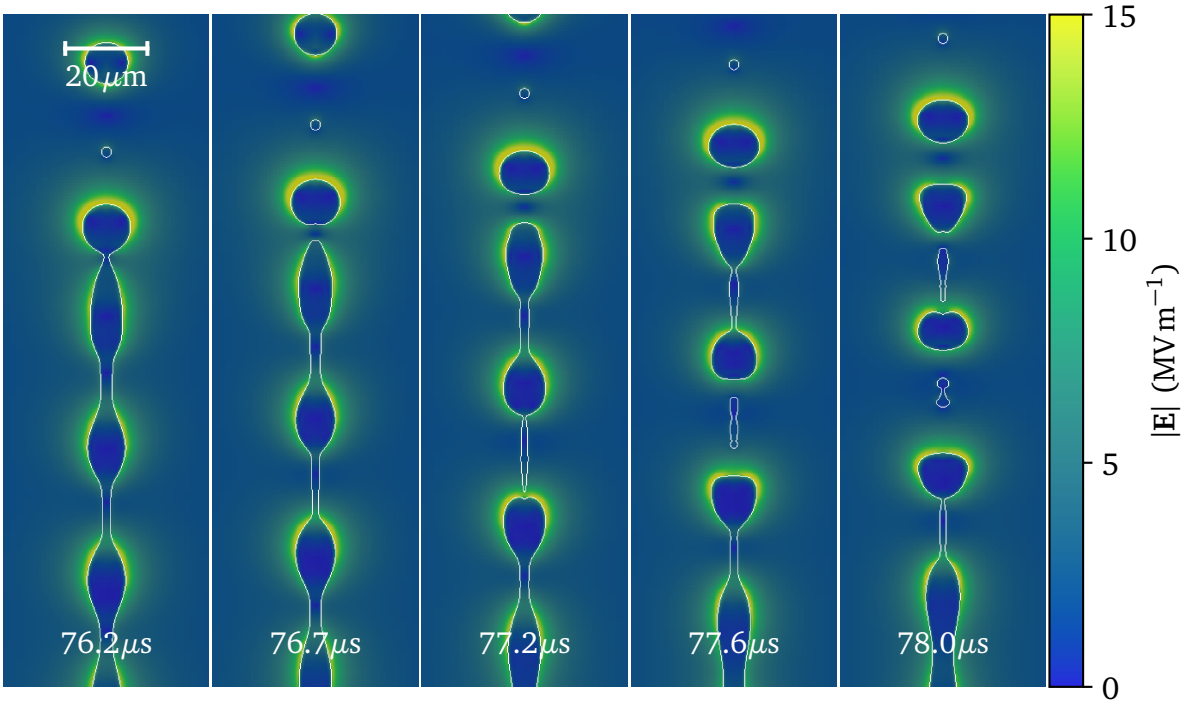

Figure 7.7: Multiple ejections for a heptane3 (see Table 7.1) electrospray. A segment of the jet is ejected at $t = 77.2\,\mu s$, before immediately breaking into two pairs of primary and satellite droplets.

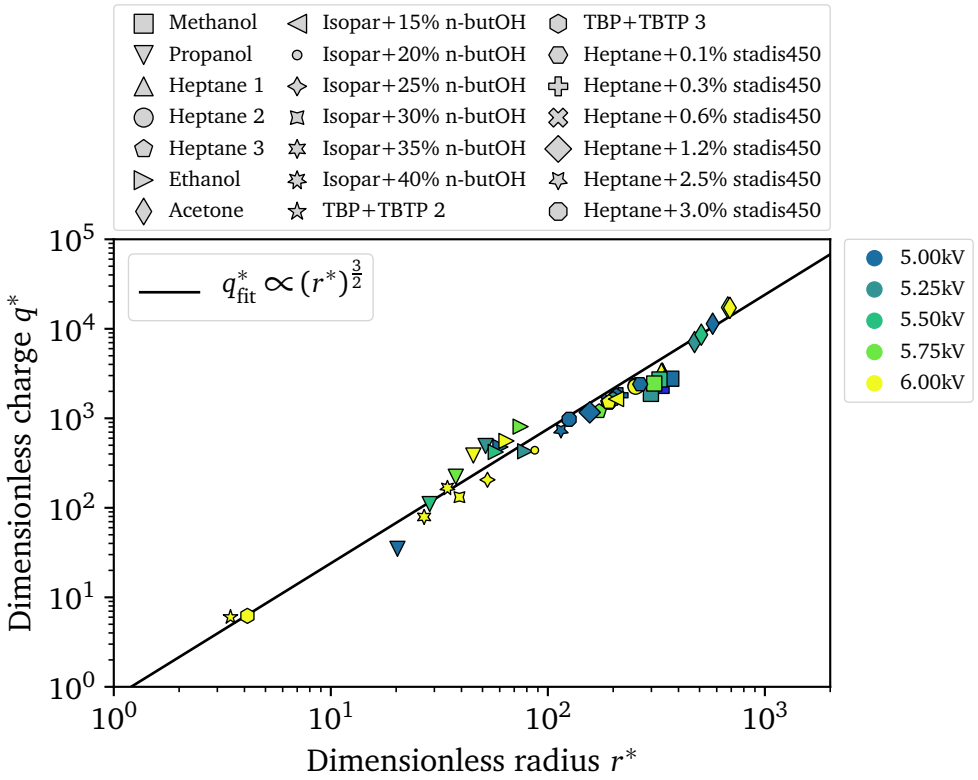

Figure 7.8: Comparison of simulation results with the universal scaling law derived in [18] (adapted from [82]). The material properties for the test liquids are summarised in Table 7.1.

the first ejected droplet are evaluated. The results are summarised in Fig. 7.8, showing a good agreement with the analytical law.

7.2.4 Characterisation of Subsequent Droplet Ejections

In the following, longer time transient behaviour of electrosprays is investigated. Differently from Section 7.2.3, not just the first ejected droplet but, rather, the properties of a number of subsequently ejected droplets are considered. For clarity, graphs in this section use the same markers for each liquid as in Fig. 7.8.

As the electrospray develops, the space-charge field of already ejected droplets builds up, thus, affecting the ongoing atomisation process [131]. Furthermore, the shape and velocity of the jet changes. It is therefore expected that the size and charge of subsequently ejected droplets will differ from that of the first ejection. The applicability of a scaling law similar to that presented in Section 7.2.3 to the successive atomisation is thus unclear. The liquids investigated in this section are methanol, ethanol, acetone, and the liquids denominated as heptane1, heptane2 and heptane3 in Table 7.1.

Table 7.1: Material properties of test liquids for transient electrospray simulations.

Liquid	Source	$\rho(\mathrm{kg\,m^{-3}})$	$\gamma(\mathrm{N\,m^{-1}})$	$\mu(\mathrm{Pa\,s})$	ε_r	$\kappa(\mathrm{S\,m^{-1}})$	τ_e (s)
TBP+TBTP 2	[43]	976	0.028	0.00359	8.91	1.64×10^{-3}	4.81×10^{-8}
TBP+TBTP 3	[43]	976	0.028	0.00359	8.91	5.34×10^{-4}	1.48×10^{-7}
Heptane+3.0% stadis450	[113]	670	0.0186	0.000441	1.90	9.8×10^{-6}	1.72×10^{-6}
Heptane+2.5% stadis450	[113]	670	0.0185	0.000437	1.91	8.3×10^{-6}	2.04×10^{-6}
Heptane+2.0% stadis450	[113]	670	0.0187	0.000434	1.91	6.7×10^{-6}	2.52×10^{-6}
Acetone	[43]	790	0.023	0.00032	20.7	5.3×10^{-5}	3.46×10^{-6}
Heptane3	[43]	684	0.021	0.00039	1.9	4.50×10^{-6}	3.74×10^{-6}
Heptane+1.2% stadis450	[113]	670	0.0186	0.000428	1.92	4.1×10^{-6}	4.15×10^{-6}
Ethanol	[43]	795	0.0226	0.00120	24.55	3.5×10^{-5}	6.21×10^{-6}
Heptane+0.6% stadis450	[113]	670	0.0186	0.000425	1.93	2.3×10^{-6}	7.43×10^{-6}
Heptane2	[43]	684	0.021	0.00039	1.9	1.90×10^{-6}	8.85×10^{-6}
Heptane+0.3% stadis450	[113]	670	0.0186	0.000427	1.93	1.4×10^{-6}	1.22×10^{-5}
1-Propanol	[42]	803	0.0237	0.00194	20.33	9.0×10^{-6}	2.00×10^{-5}
Heptane1	[43]	684	0.021	0.00039	1.9	7.72×10^{-7}	2.18×10^{-5}
Heptane+0.1% stadis450	[113]	670	0.0186	0.000425	1.94	7.3×10^{-7}	2.35×10^{-5}
Isopar+40% n-butOH	[43]	771	0.024	0.0021	10	2.22×10^{-6}	3.99×10^{-5}
Methanol	[42]	795	0.021	0.00059	33.6	7.0×10^{-6}	4.25×10^{-5}
Isopar+35% n-butOH	[43]	767.75	0.024	0.00203	7	1.25×10^{-6}	4.96×10^{-5}
Isopar+30% n-butOH	[43]	764.5	0.024	0.00195	5.2	4.00×10^{-7}	1.15×10^{-4}
Isopar+25% n-butOH	[43]	761.25	0.024	0.00188	3.56	1.33×10^{-7}	2.37×10^{-4}
Isopar+20% n-butOH	[43]	758	0.024	0.0018	3.06	3.85×10^{-8}	7.04×10^{-4}
Isopar+15% n-butOH	[43]	754.75	0.024	0.00173	2.64	7.14×10^{-9}	3.27×10^{-3}

7.2.4.1 Characterisation of heptane2 spray

Size of ejected droplets

Figure 7.9 shows the radius of electrospray droplets vs. detachment time for heptane2 for different applied voltages. A few observations can be made regarding the size of the successive ejections. In each electrospray, the droplet size provides a simple criterion for discriminating between the primary droplets ($r > 2.5\,\mu$m) and the smaller satellite droplets. The droplets sizes follow the same trend for the different applied voltages. For almost all applied voltages, the radius of the first ejection is slightly larger than that of the few primary ejections following it. The radius of primary droplets then steadily increases beyond that of the initial ejection.

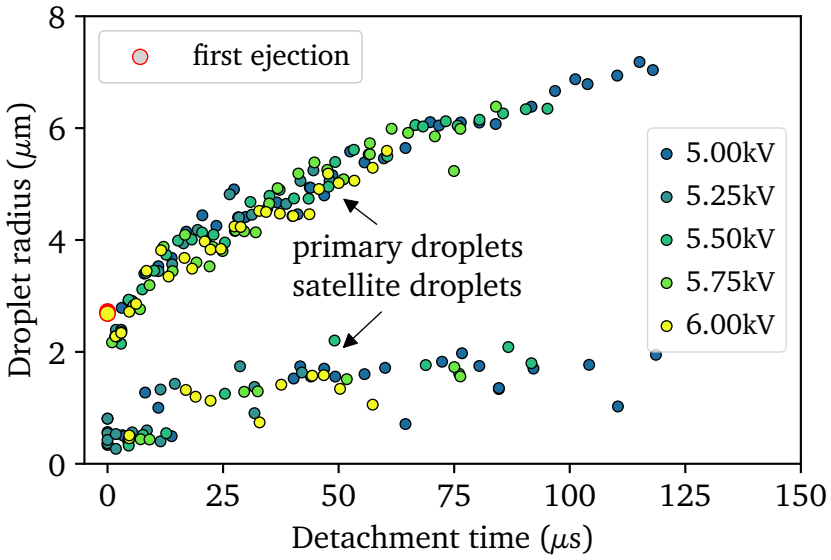

Figure 7.9: Size of successive ejections in function of time in the case of heptane2 electrosprays (adapted from [82]). The time instants are given with respect to respective first ejections. Here, the first ejections are nearly identical; the corresponding markers overlap.

Charge of ejected droplets

The charge of the successive ejections is shown in Fig. 7.10. Similar observations can be made for the net charge carried by droplets as for their size, indicating that the charge and droplet size are strongly correlated. These observations can be explained by the correlation between droplet charge and size, depicted in Fig. 7.11 Two scaling trends can be observed corresponding to primary and satellite droplets, respectively. As satellite droplets carry little charge compared to primary droplets, only the charge-radius characteristic of the latter is considered. Clearly, this characteristic fits well to a power law. The scaling exponent is, however, different from that of the first ejected droplet. For comparison, the charge of the first ejected droplets for each applied

voltage indicates that this droplet always carries a higher net charge than that of droplets of the same size ejected later.

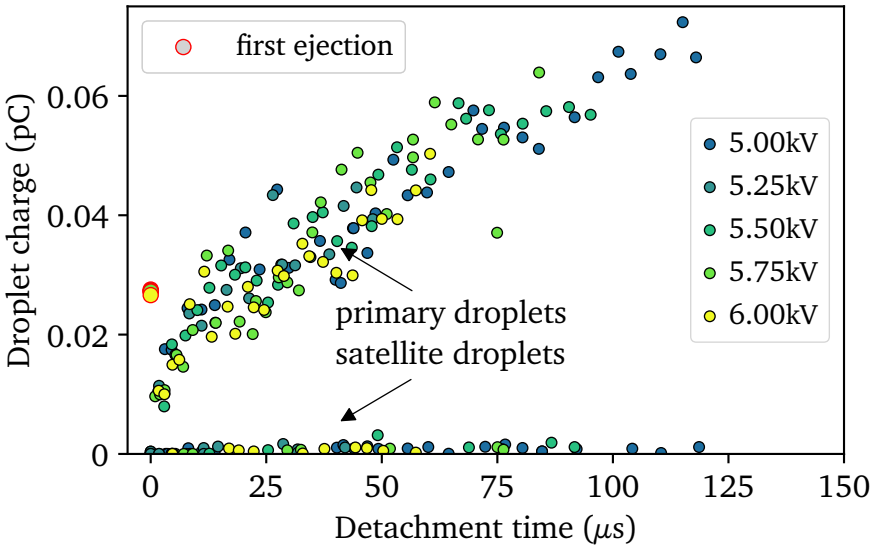

Figure 7.10: Charge of successive ejections in function of time in the case of heptane2 electrosprays. The time instants are given with respect to respective first ejections. Here, the first ejections are nearly identical; the corresponding markers overlap.

Impact of sessile drop volume

The simulated charge-radius characteristics of heptane are nearly identical for different applied voltages. One question of interest is to what extent observed electrospray characteristics are independent from experimental parameters. Since the other main input parameter is the sessile drop volume, we now investigate the transient dynamics of heptane2 electrosprays for different initial sessile drop volumes. The transient dynamics of the electrospray for different sessile drop volumes are shown in Fig. 7.12. There, it is clear that the characteristics of neither the first nor the successive ejections are impacted significantly by the volume of the initial sessile drop. A small discrepancy is observed only for the lowest volume, 0.2 μl, where multiple larger droplets are observed. This is due to multiple primary ejections occurring at the same time, similarly to the case shown Fig. 7.7.

7.2.4.2 Characterisation of other liquids

Numerical simulations for other liquids show similar trends. The charge-radius characteristic for acetone, methanol and heptane electrosprays are depicted in Figs. 7.13 to 7.17. In all cases, a clear separation between primary and satellite droplets is observed. However, the relative size spread of the successive primary droplets ejections is larger for acetone, ethanol

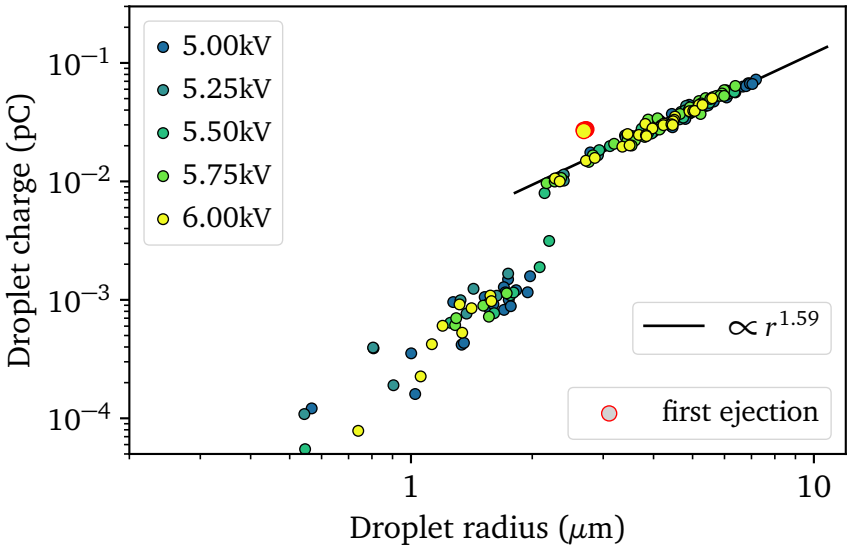

Figure 7.11: Charge-radius characteristic of atomised droplets in the case of heptane2 electrosprays. Solid line: best fit for primary droplets (r >2.5 μm) with a power law. Here, the initial ejections for the different voltages are nearly identical.

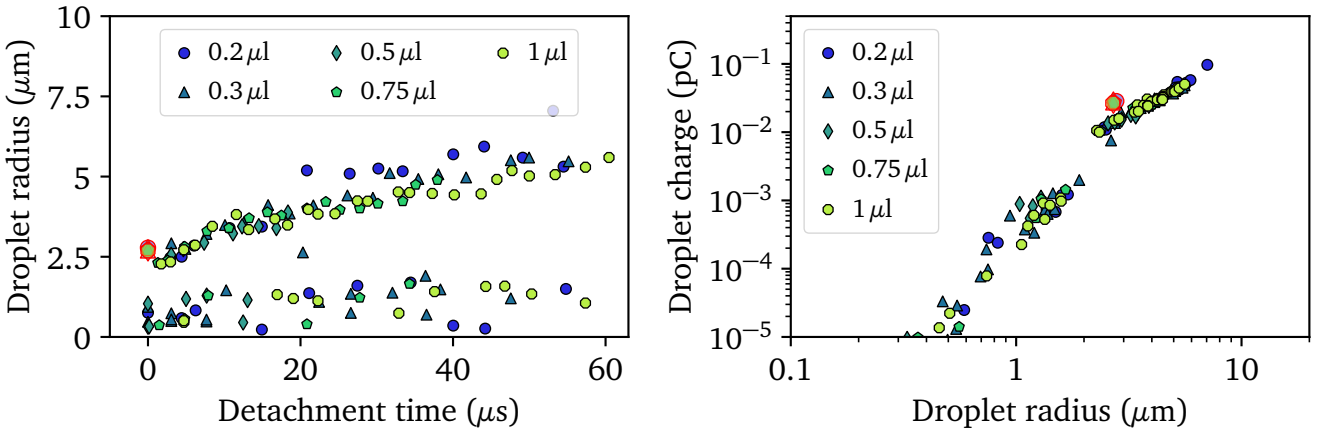

(a) **(b)**

Figure 7.12: Characteristic of ejections for different initial sessile drop volumes in the case of heptane2 electrosprays subjected to 6 kV. (a) Size of successive ejections in function of time. The time instants are given with respect to the respective first ejections. (b) Charge-radius characteristic of atomised droplets. Here, the initial ejections for the different sessile drop volumes are nearly identical.

and methanol, compared to heptane. Although the number of simulated ejections is insufficient to estimate the time-dependent standard deviation, the observations for methanol and heptane qualitatively agree with results from [41], where methanol sprays are found to have a relative standard deviation three times larger than heptane sprays. Regardless of the relative standard deviation, the primary droplet characteristics are still well represented by power laws. Table 7.2

Table 7.2: Fitted power law relation between charge and radius of primary droplets for various liquids.

Test liquid	Fitted power law
Heptane1	$q \propto r^{1.57}$
Heptane2	$q \propto r^{1.59}$
Heptane3	$q \propto r^{1.75}$
Methanol	$q \propto r^{2.19}$
Ethanol	$q \propto r^{2.34}$
Acetone	$q \propto r^{2.37}$

summarises the scaling law exponents obtained by multiple simulations for different liquids and applied voltages. The main observation resulting from the simulations is that the charge-radius correlation for a droplet ejected later in the electrospray may be described by a simple power law similar to the one obtained in [18] for the first ejection. The scaling exponent, however, is different and depends on liquid properties.

7.2.4.3 Current voltage characteristics

Another quantity of interest for characterising electrosprays is the electric current associated with the charged droplet flow. The average current vs. applied voltage is shown in Fig. 7.18, for a few test liquids. The average electrospray current is almost independent from the applied voltage. It depends mainly on the electromechanical properties of the liquid. This result is consistent with the experimental findings in [41]. Note, however, that due to the long computation times, only a limited number of ejections was considered in each set of simulations. Thus, the current curves in Fig. 7.18 do not exactly reflect the steady state IV-characteristics of the respective electrosprays. This may explains the somewhat larger spread of the simulated current points in the acetone case.

7.3 Convergence Study of Electrospray Simulation Results

In this section, numerical convergence issues for the simulation of transient electrosprays from sessile droplets are discussed. The case of a heptane ($\kappa = 1.9\,\mu\mathrm{S\,m^{-1}}$) spray from a $1\,\mu$L sessile droplet subjected to 5.5 kV is considered here. The initial refinement level is chosen as $l_{\mathrm{init}} = 3$ in all simulations. The procedure described in Section 7.2.1 is used to gradually increase the maximal refinement level l_{max}. The size of detached droplets and charge-radius characteristics of the simulated electrosprays for different values of l_{max} are shown in Fig. 7.19.

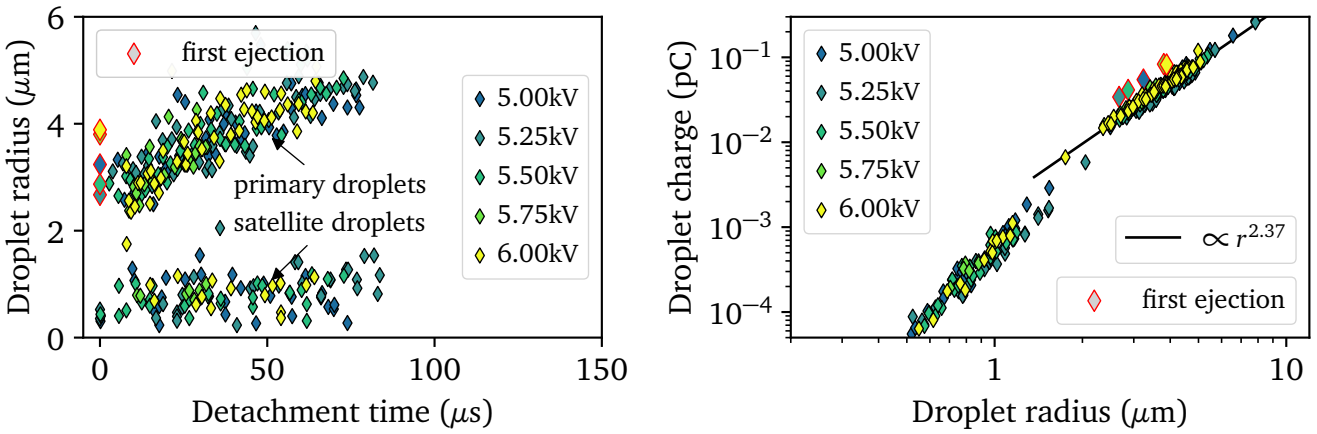

(a) **(b)**

Figure 7.13: Characteristic of ejections for different voltages in the case of acetone electrosprays. (a) Size of successive ejections in function of time. The time instants are given with respect to the respective first ejections. (b) Charge-radius characteristic of atomised droplets. Solid line: best fit for primary droplets ($r > 2\,\mu$m) with a power law.

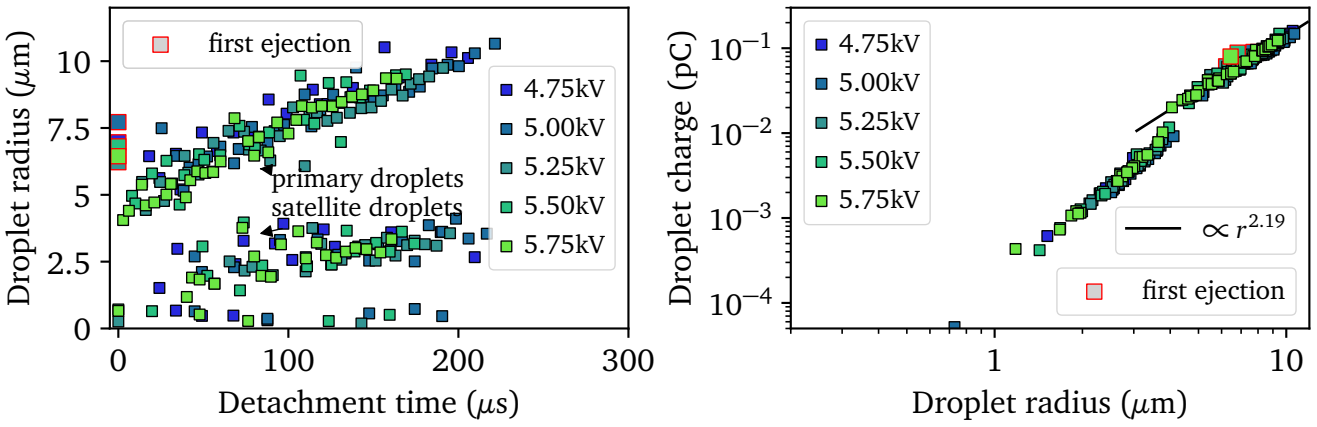

(a) **(b)**

Figure 7.14: Characteristic of ejections for different voltages in the case of methanol electrosprays. (a) Size of successive ejections in function of time. The time instants are given with respect to the respective first ejections. (b) Charge-radius characteristic of atomised droplets. Solid line: best fit for primary droplets ($r > 4.5\,\mu$m) with a power law.

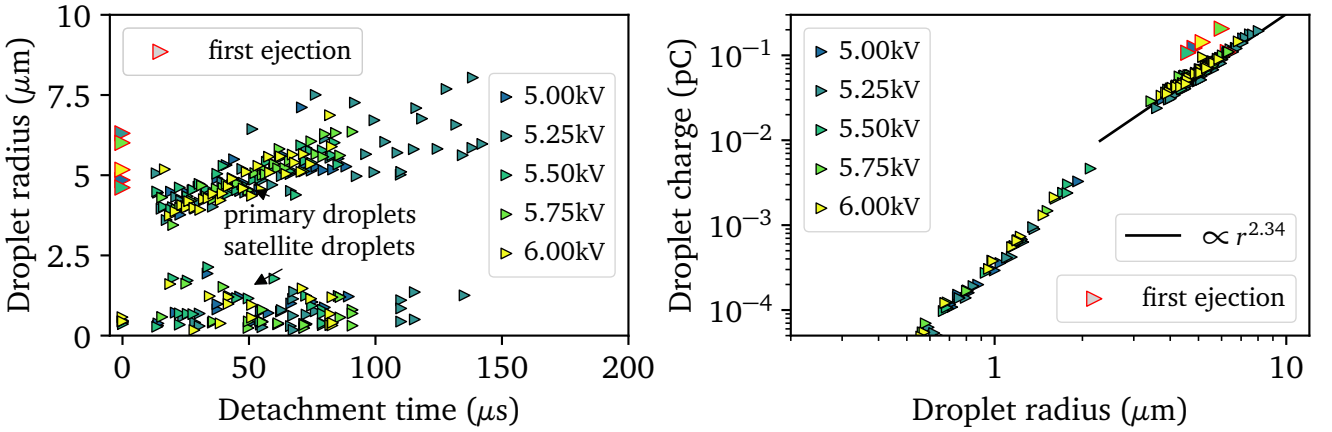

(a) (b)

Figure 7.15: Characteristic of ejections for different voltages in the case of ethanol electrosprays. (a) Size of successive ejections in function of time. The time instants are given with respect to the respective first ejections. (b) Charge-radius characteristic of atomised droplets. Solid line: best fit for primary droplets ($r > 3.0\,\mu$m) with a power law.

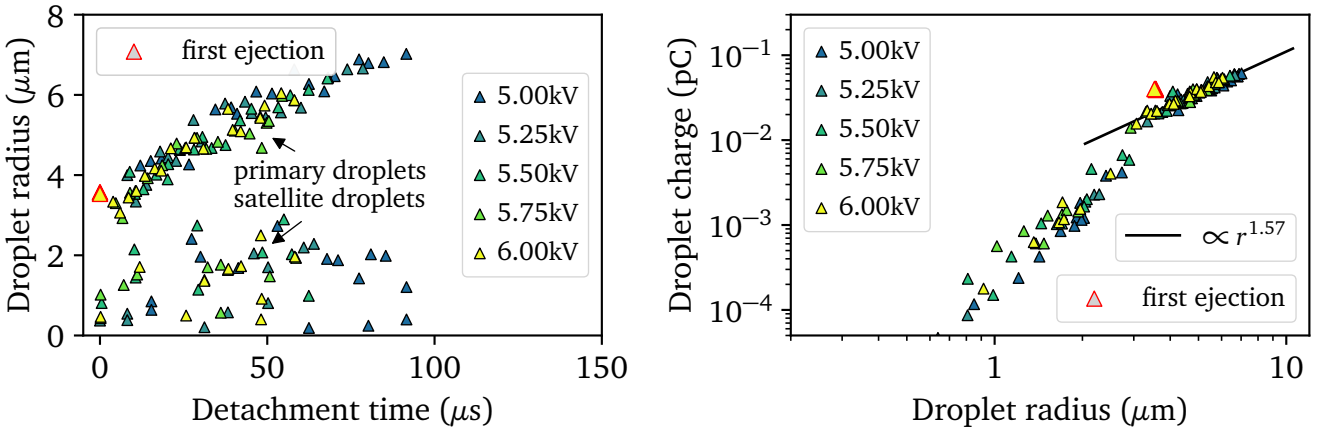

(a) (b)

Figure 7.16: Characteristic of ejections for different voltages in the case of heptane1 electrosprays. (a) Size of successive ejections in function of time. The time instants are given with respect to the respective first ejections. (b) Charge-radius characteristic of atomised droplets. Solid line: best fit for primary droplets ($r > 3.0\,\mu$m) with a power law. Here, the initial ejections for the different voltages are nearly identical.

At lower levels of interface refinement, the size of primary droplets is overestimated and the ejection rate underestimated compared to the finer levels. The qualitative behaviour of primary ejections remains, however, the same as for the finest levels. At the two finest levels of refinement, $l_{\max} = 7$ and $l_{\max} = 8$, the size of primary droplets follows the exact same trend. In addition, the presence of satellite droplets is properly resolved only for $l_{\max} \geq 7$. Figure 7.19b illustrates the convergence of the net charge in detached droplets via the charge-radius characteristic. The power-law correlation for the charge of primary droplets observed in Section 7.2.4 is valid regardless of the level of refinement of the interface.

7.4 Electrosprays from Dripping Liquid

In the previous section, electrosprays are forced from sessile droplets. This configuration does not allow for direct control of the flow rate of the electrospray. In the following, electrosprays formed from liquid dripping from a capillary are considered. The numerical results are compared with experimental data from the literature [113].

The test liquid, heptane enriched by stadis 450 in order to modify the conductivity, drips from a grounded capillary. A volumetric flow of liquid is imposed, up to $28\,\mathrm{ml\,h^{-1}}$. Electrodes located at a distance below the capillary are held at a constant voltage of a few kilovolts. An electrospray in the cone-jet mode is formed nearly immediately after the liquid starts dripping from the capillary. Since the fluid is continuously replaced, in the proper range of mass flow rate and applied voltage, a steady cone-jet electrospray is eventually obtained. In this configuration, the flow rate is a dominant parameter controlling the electrospray, especially at low flow rates [113]. The generated droplet size can be increased by one order of magnitude, by increasing the flow rate.

7.4.1 Numerical Setup

In the following, simulation results for electrospray atomisation of heptane+0.3% statis 450 (see Table 7.1) with $U_0 = 4\,\mathrm{kV}$ and $\varphi \in [0.39\,\mathrm{ml\,h^{-1}}, 28\,\mathrm{ml\,h^{-1}}]$ are presented. The numerical setup, corresponding to the experimental setup whose results are reported in Fig. 2.a in [113], is detailed in Fig. 7.20 and Table 7.3. The simulations were run assuming axisymmetry, with a maximal level of refinement $l_{\max} = 5$ for flow rates $\varphi \leq 12\,\mathrm{ml\,h^{-1}}$ and $l_{\max} = 4$ for $\varphi > 12\,\mathrm{ml\,h^{-1}}$, with a base mesh (level 0) parameter $\Delta\rho = \Delta z = 15\,\mu\mathrm{m}$. The simulations took ≈ 8 weeks of computational time, in order for primary droplets sizes to reach a steady state in all simulations.

7.4.2 Results

Simulation results are shown exemplarily in Fig. 7.21, for a flow rate of $6.2\,\mathrm{ml\,h^{-1}}$. The dynamics of the jet and atomised droplets are very similar to those obtained from a heptane2 sessile

Boundary	Variable				
	p_d	$\mathbf{u}$	α	Φ	ϱ_e
Inlet (AB)	$\nabla_n p_\mathrm{d} = 0$	$\mathbf{u}\cdot\mathbf{n} = \frac{\varphi}{\pi r_\mathrm{inlet}^2}$	$\alpha = 1$	$\nabla_n \Phi = 0$	$\nabla_n \varrho_\mathrm{e} = 0$
Capillary surface (BCDE)	$\nabla_n p_\mathrm{d} = 0$	$\mathbf{u} = 0$	$\nabla_n \alpha = 0$	$\Phi = 0$	$\nabla_n \varrho_\mathrm{e} = 0$
Free stream surface (EFG)	$p_0 - \frac{1}{2}\lvert\mathbf{u}\rvert^2$	$\nabla_n \mathbf{u} = 0$	$\nabla_n \alpha = 0$ if $\mathbf{u}\cdot\mathbf{n} \leq 0$ 0 otherwise	$\nabla_n \Phi = 0$	$\nabla_n \varrho_\mathrm{e} = 0$
Electrode surface (GH)	$\nabla_n p_\mathrm{d} = 0$	$\mathbf{u} = 0$	$\nabla_n \alpha = \cos(\theta)$ * or $\alpha = \text{const.}$	$\Phi = U_0$	$\nabla_n \varrho_\mathrm{e} = 0$

Table 7.3: Boundary conditions used for the numerical simulations of the electrosprays from dripping liquid. The boundary conditions indicated with * indicate the contact angle boundary condition described in Section 3.3.3.

drop (see Fig. 7.5). This is expected, since the properties of the two test liquids are similar. It should be noted, however, that the size of atomised droplets from the capillary in the steady state is larger by a factor three than observed from the sessile drop. This is due to the larger flow rate producing in a thicker jet from which the droplets atomise.

Comparison with experimental data

The simulated mean droplet sizes are compared with experimental results from [113] for different flow rates in Fig. 7.22. The simulated droplet sizes are in good agreement with the experimental results, both qualitatively and quantitatively. The mean relative deviation of the simulated mean diameters is 12%. The validity of the simulation results and numerical model is thus confirmed.

Size distribution of droplets

The size of the successive ejections for a few flow rates are shown in Fig. 7.23. Similarly to electrosprays from sessile drops, the size of successive ejections increases with time, until a steady state is obtained. For each flow rate, primary and satellite droplets are clearly identifiable, as satellite droplets are much smaller than the corresponding primary droplets. However, the size of satellite droplets differs for the different flow rates, following the trend of primary droplets.

The size distributions of the droplets at the last simulated time step for a few flow rates are shown in Fig. 7.24. For each flow rate, the size distribution of primary droplets is asymmetric. The relative frequency of droplets smaller than the most likely size drops quickly, while size deviations up to 30% larger are observed more frequently.

Charge radius characteristics

The charge-radius characteristic of atomised droplets is shown for a few flow rates in Fig. 7.25. Again, similar trends as in electrosprays from sessile drops are observed. The power law correlation for primary droplets is observed for droplet sizes varying over more than one order of magnitude. Satellite droplets also hold a significantly lower charge than primary droplets. However, flow rate dependent correlations are observed for satellite droplets. These correlations seem to obey a power law with an exponent close to 3. This indicates a nearly constant charge density in satellite droplets for each electrospray. This charge density decreases with the flow rate, so that satellite droplets at higher flow rate hold less charge than satellite droplets of similar size generated at a lower flow rate.

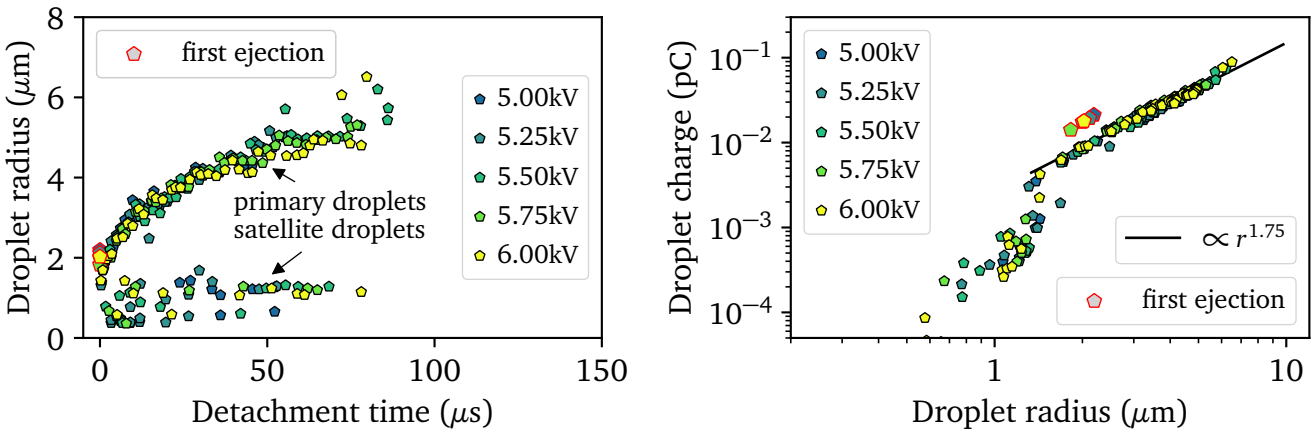

(a) (b)

Figure 7.17: Characteristic of ejections for different voltages in the case of heptane3 electrosprays. (a) Size of successive ejections in function of time. The time instants are given with respect to the respective first ejections. (b) Charge-radius characteristic of atomised droplets. Solid line: best fit for primary droplets ($r > 2.0\,\mu$m) with a power law.

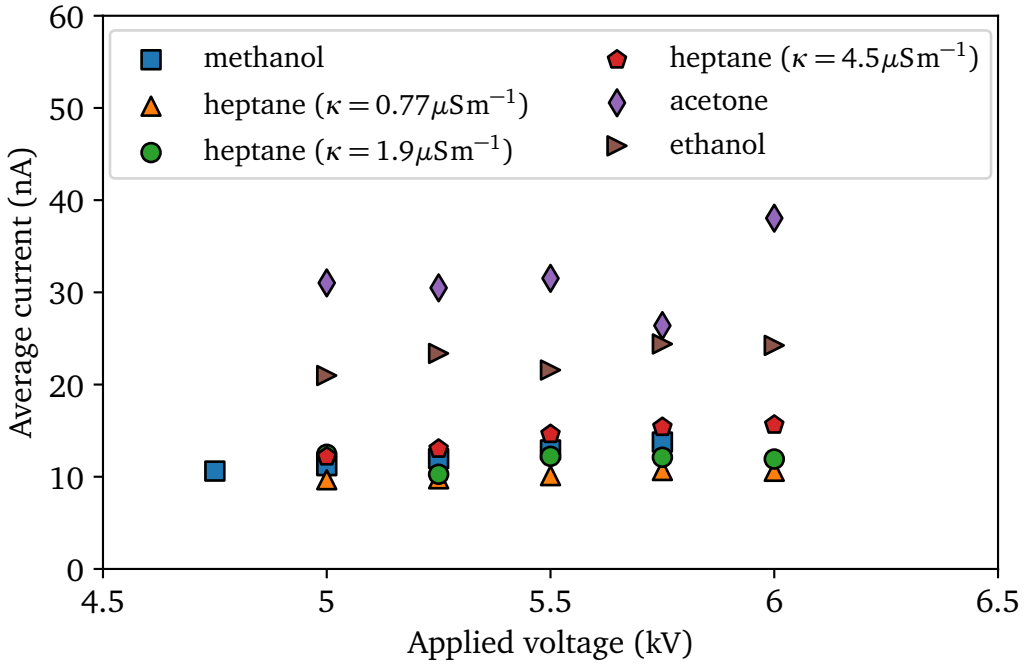

Figure 7.18: IV-characteristics of electrospray computed for different liquids, for 1 μl droplets with a 5 mm electrode distance.

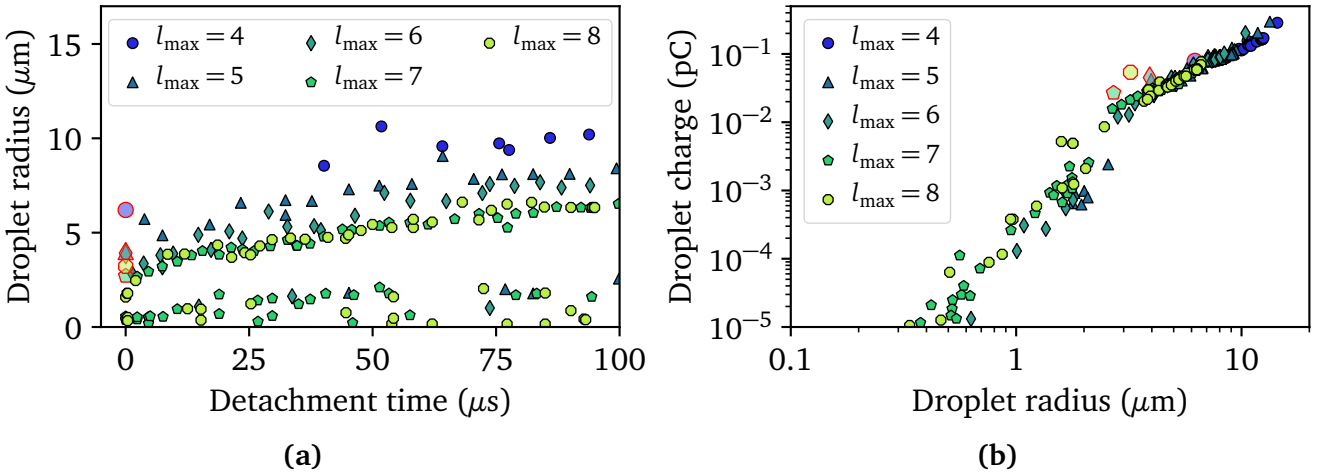

(a) **(b)**

Figure 7.19: Simulated ejections for different levels of mesh refinement in the case of heptane2 electrosprays. (a) Size of successive ejections in function of time. The time instants are given with respect to the respective first ejections. (b) Charge-radius characteristic of atomized droplets.

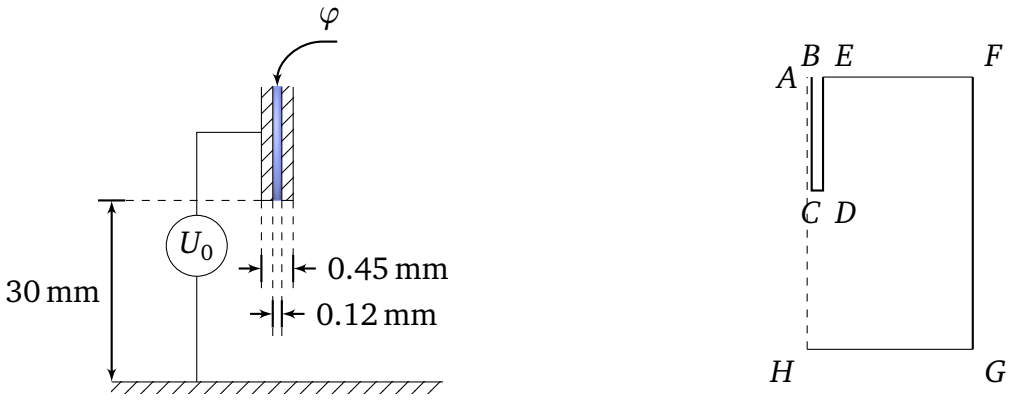

(a) **(b)**

Figure 7.20: Schematic view and main parameters of the simulation domain and labels of the boundaries of the computational domain for the simulation of electrosprays from dripping liquid. (a) Schematic view and main parameters of the simulation domain. (b) Labels of the boundary conditions applied to the computational domain (see Table 7.3).

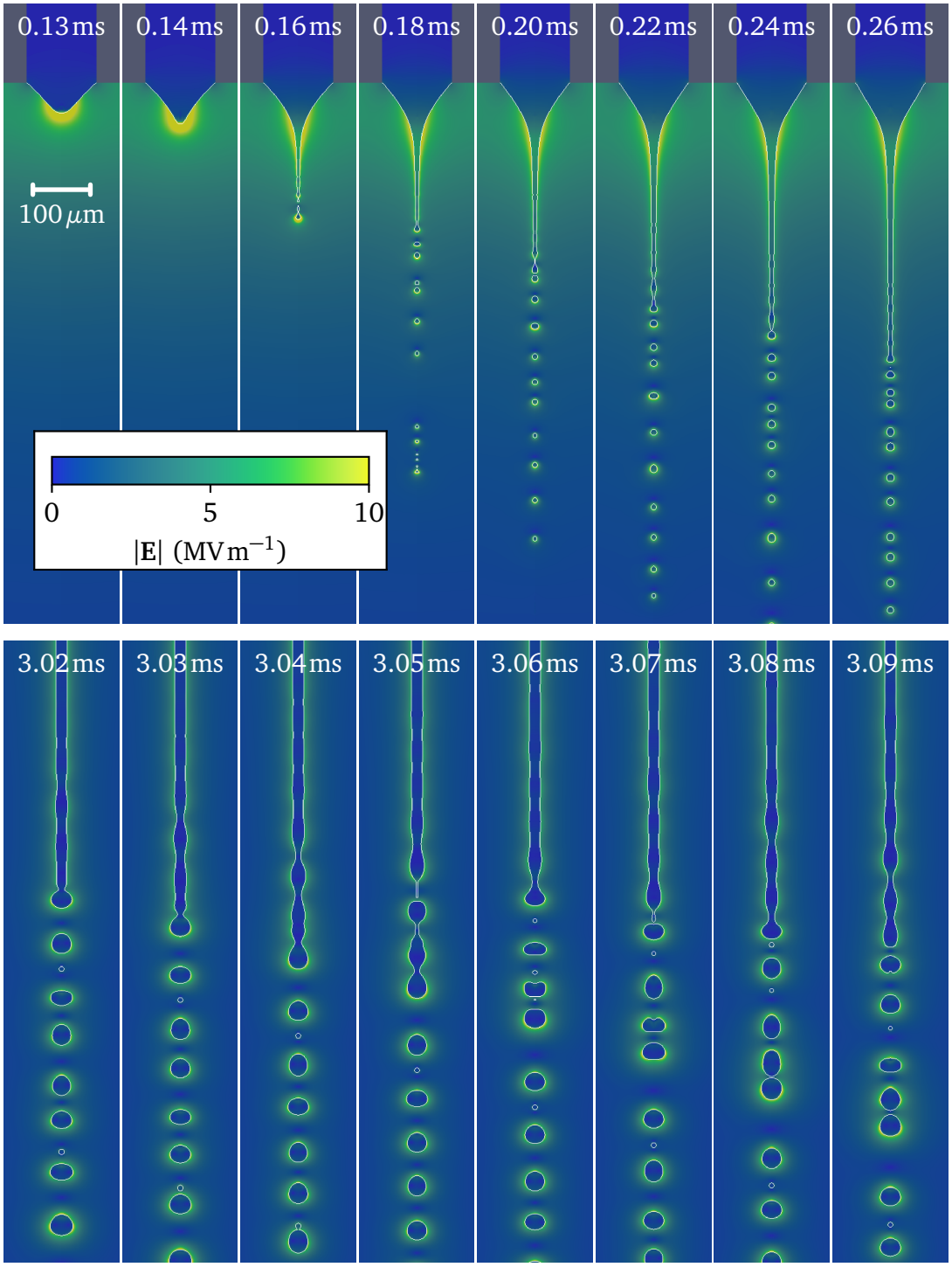

Figure 7.21: Ejections from an electrospray with flow rate $6.2\,\mathrm{ml\,h^{-1}}$. Top row: onset and first few ejections of the electrospray. Bottom row: ejections from the fully developed (steady state) jet.

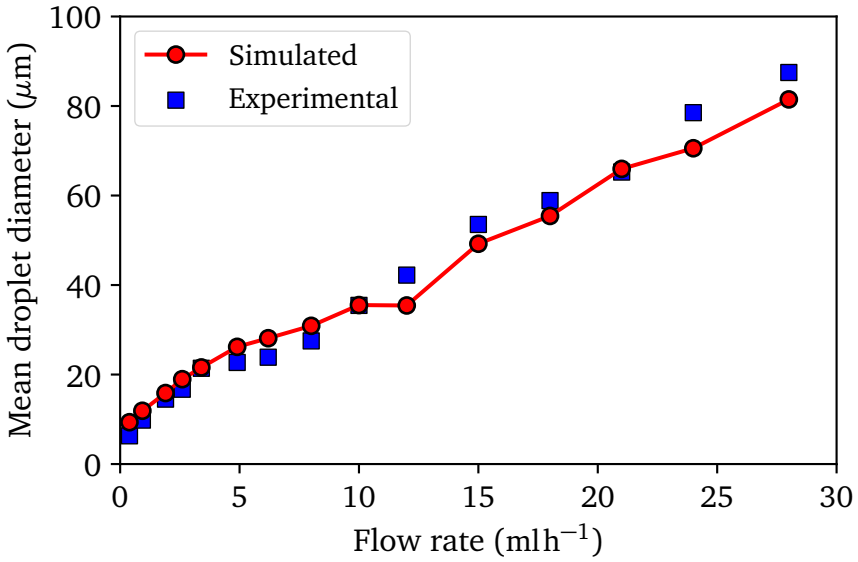

Figure 7.22: Comparison of simulated mean droplet diameter with experimental results from [113], Fig. 2(a).

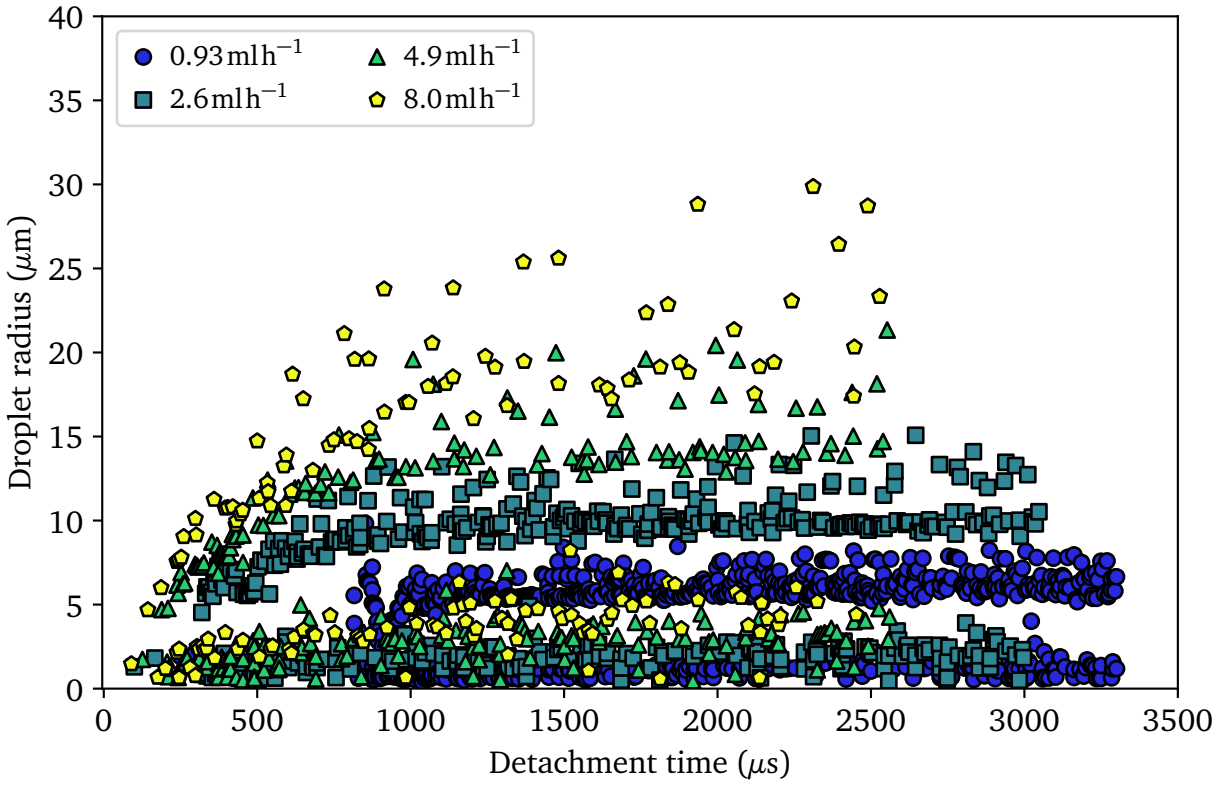

Figure 7.23: Size of successive ejections in function of time for different flow rates. For clarity, only a few of the simulated flow rates are shown.

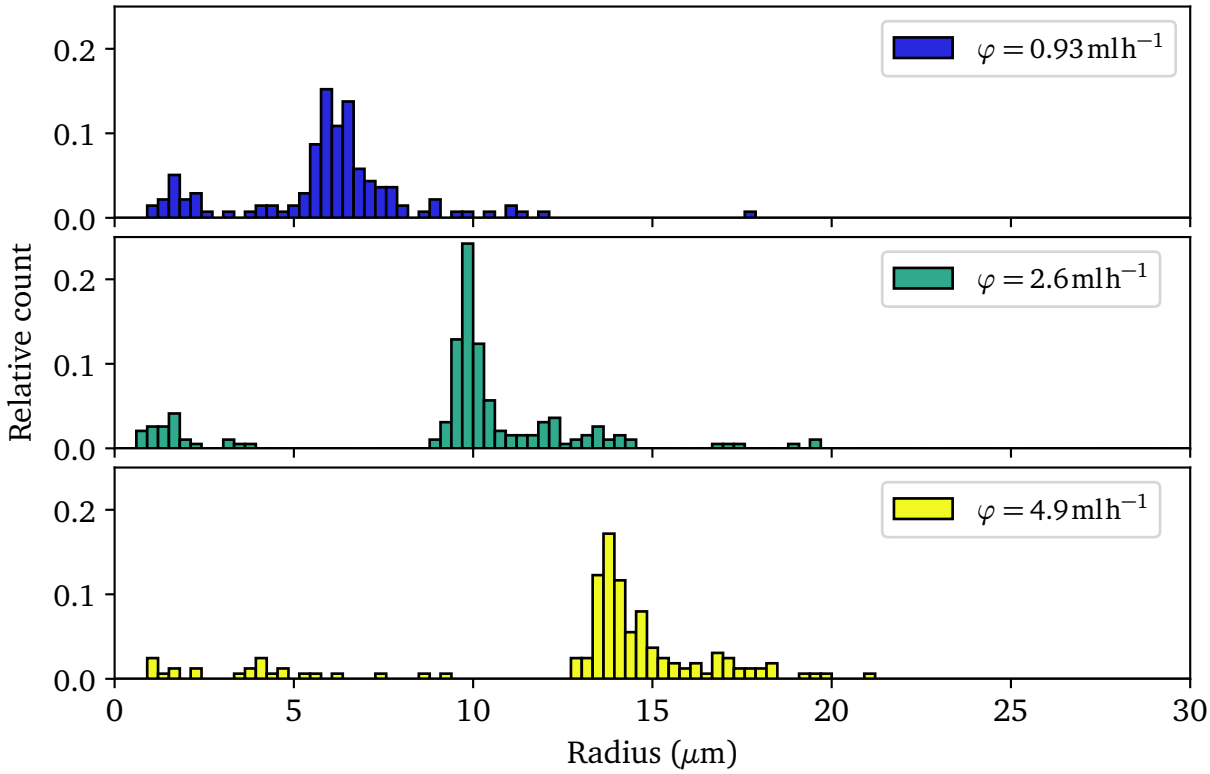

Figure 7.24: Size distributions of atomised droplets for different flow rates.

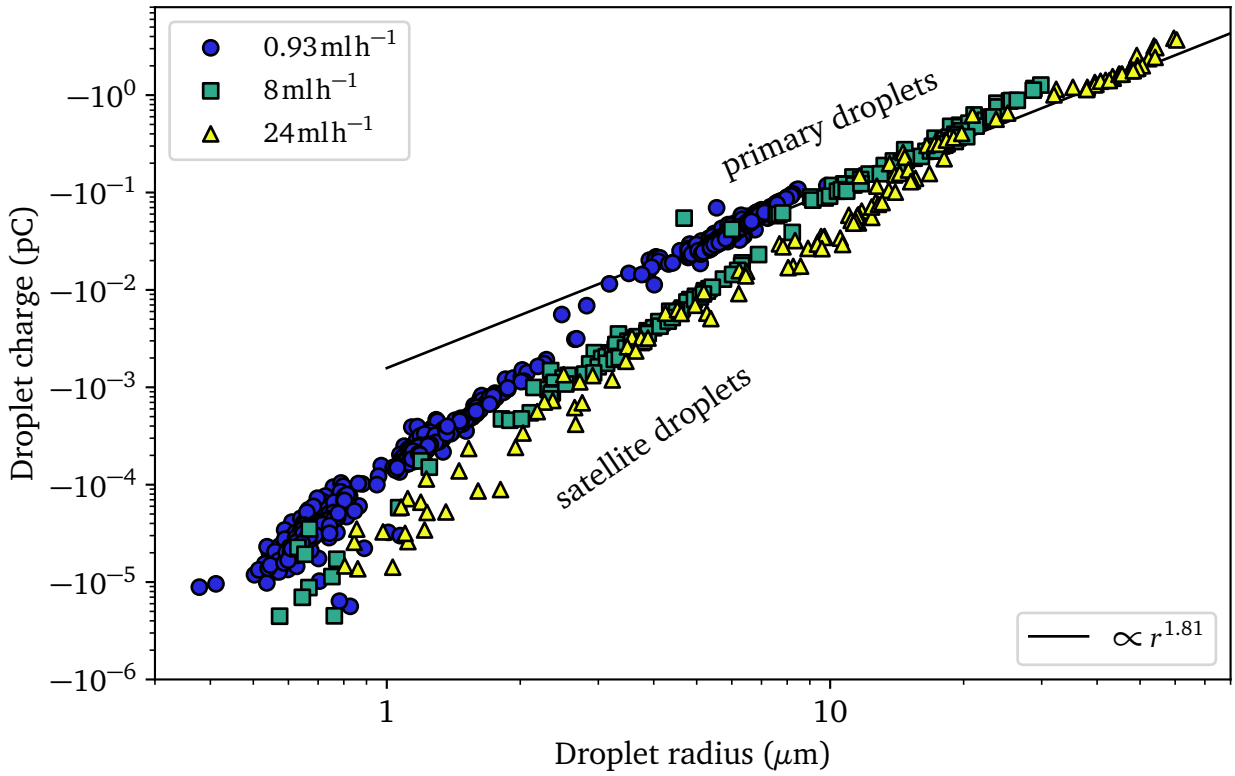

Figure 7.25: Charge-radius characteristic of atomised droplets for different flow rates. Solid line: best fit for primary droplets for all simulated flow rates. For clarity, only a few of the simulated flow rates are shown.

8 Summary and Outlook

8.1 Summary

In this thesis, the electrohydrodynamic behaviour of liquids subjected to electric fields is considered by means of numerical simulations. The numerical solver is based on the open source computational fluid dynamics library OpenFOAM, modified to perform fully coupled electrohydrodynamic simulations. A diffuse interface approach is used for both the hydrodynamic and electroquasistatic problem. This allows to robustly handle topology changes of the fluid-fluid interface occurring frequently in numerical simulations of electrospray atomisation. A dynamical contact angle model including contact line hysteresis effects is integrated into the electrohydrodynamic solver. The stick-slip behaviour of contact lines, particularly relevant in the case of sessile droplets subjected to strong electric fields, is thus captured. Free charge in liquids is modelled in the electroquasistatic approximation by considering the capacitive, resistive and convective currents in the liquids. Dynamical charging effects when the time scales of charge relaxation and fluid flow are comparable can thus be represented. These effects play a major role in electrospraying, where tangential electric fields acting on the free charge at the surface of the jet drive the electrospray.

Fluid flows involved in three relevant technical applications are studied using the numerical solver developed in this thesis. First, the case of oscillating droplet on the surface of high voltage insulators is considered. The dynamics of the modal oscillations are studied in a first step and validated with experimental data. Then, the partial discharge inception field strength is evaluated for different static droplets, depending on their volume and contact angle. The results show that partial discharges occur in all cases in the vicinity of the contact line, where an electric field singularity is observed. The dependency of the inception voltage on the different voltages is shown to be consistent with semi-analytically calculated indices characterising the singularity. The partial discharge inception results are validated with experimental data on static droplets.

In a second step, the behaviour of an on-demand droplet generator is characterised. In this setup, electric fields are used to force the detachment of liquid droplets from a capillary. The simulated behaviour of acetone droplets, which exhibit a short charge relaxation time compared to the typical scale of fluid motion, is compared to experimental results, showing good agreement. The dynamics on the capillary indicate that droplets are simply accelerated away from the capillary by the electric forces, so that detachment is obtained in a straightforward manner. However, in the case of a lower conductivity liquid, n-pentane, droplets are accelerated towards

the capillary with the electric forces. Detachment is thus obtained in a two step process, first dominated by the electric forces, and then by the weight of the droplets. The difference between the two behaviours is directly tied to the different dynamical charging behaviour, which produce different electric forces on the droplets.

In the final part of the thesis, atomisation of microdroplets is studied. The case of electrosprays in the cone-jet mode from sessile droplets is considered. Due to the large size difference between the sessile droplets and atomised microdroplets, adaptive mesh refinement and load balancing techniques are used to ensure that a sufficient spatial resolution is obtained, while keeping the computational cost acceptable. The dynamics of the different ejections of the transient electrospray are studied for a range of test liquids. The electrospray is found to scale independently of experimental parameters such as sessile drop volume and applied voltage. A power law scaling between the charge and size of atomised droplets is found, with different exponents depending on the atomised liquid. The simulations are validated using a universal scaling law derived in the literature relating the charge and size of the first ejection of electrosprays. The quantitative results on simulated microdroplet sizes are further validated by comparison with experimental data in the case of electrospray from dripping liquid.

8.2 Outlook

For future research, the numerical model could be further improved to account for additional electrohydrodynamic effects. The modelling of ionic species in this thesis neglects the effect of the diffusion of ionic species. Furthermore, the mobilities of all ionic species in liquids are aggregated into a single constant, the electrical conductivity. In practice, the apparent electrical conductivity may depend on the local flow patterns and electric field distribution. The electrohydrodynamic model could be extended to account for this effect by considering transport equations for each ionic species separately [65].

The characterisation of electrosprays is a topic of interest for future research. However, numerical simulations require large computational resources. Optimisation of the numerical solver in terms of computational costs would be beneficial for future works. The equations representing the electrohydrodynamic problem were solved in a segregated manner. This introduces strong constraints on the stability of the time stepping scheme, in particular for liquids with short electrical relaxation times. The efficiency of the solver could be improved for these cases, by considering different time step sizes for the hydrodynamic and electroquasistatic problems. Solver efficiency could also be improved by solving the equations in a coupled manner, rather than segregated.

On the application side, partial discharge prediction on high-voltage insulators in the dynamic case has not been addressed in this thesis. The oscillatory motion of droplets on high-voltage insulators leading to large deformations of their interface was not considered for partial discharge

inception field calculations discussed in Section 5.5.3. Including partial discharge detection, similarly to the procedure described in Section 5.5.2, into the electrohydrodynamic solver could allow to identify local electric field patterns producing partial discharges.

Finally, the simulation package developed in this thesis is readily applicable to characterise other electrohydrodynamic flows involving conductive fluids. Since contact line dynamics are modelled taking hysteretic effects into account, electrowetting applications, where single droplets are manipulated in a controlled manner by electric fields [69], can be also modelled. Other examples include microfluidics, where e.g. the application of electric fields can be used to control the size of droplets produced in a T-junction droplet generator [102].

Bibliography

[1] A. Baniabedalruhman. *Dynamic Meshing Around Fluid-Fluid Interfaces With Applications To Droplet Tracking In Contraction Geometries*. PhD thesis, Michigan Technological University, 2015. Cited on page 41.

[2] A. Barrero and I. G. Loscertales. Micro- and nanoparticles via capillary flows. *Annual Review of Fluid Mechanics*, 39(1):89–106, 2007. Cited on page 91.

[3] S. Batzdorf. *Heat transfer and evaporation during single drop impingement onto a superheated wall*. PhD thesis, Technische Universität Darmstadt, 2015. Cited on page 36.

[4] J. P. Borra, D. Camelot, K.-L. Chou, P. J. Kooyman, J. C. M. Marijnissen, and B. Scarlett. Bipolar coagulation for powder production: micro-mixing inside droplets. *Journal of Aerosol Science*, 30(7):945–958, 1999. Cited on page 90.

[5] J.-P. Borra, D. Camelot, J. C. M. Marijnissen, and B. Scarlett. A new production process of powders with defined properties by electrohydrodynamic atomization of liquids and post-production electrical mixing. *Journal of Electrostatics*, 40–41:633–638, 1997. Proceedings of the 8th International Conference on Electrostatics. Cited on page 90.

[6] J. B. Bostwick and P. H. Steen. Capillary oscillations of a constrained liquid drop. *Physics of Fluids*, 21(3):032108, 2009. Cited on page 17.

[7] J. B. Bostwick and P. H. Steen. Dynamics of sessile drops. Part 1. Inviscid theory. *Journal of Fluid Mechanics*, 760:5–38, 2014. Cited on page 17.

[8] C. J. Bouwkamp. A note on singularities occurring at sharp edges in electromagnetic diffraction theory. *Physica*, 12(7):467–474, 1946. Cited on page 18.

[9] J. U. Brackbill, D. B. Kothe, and C. Zemach. A continuum method for modeling surface tension. *Journal of Computational Physics*, 100(2):335–354, 1992. Cited on page 36.

[10] I. M. Braver, P. S. Fridberg, K. L. Garb, and I. M. Yakover. The behavior of the electromagnetic field near the edge of a resistive half-plane. *IEEE Transactions on Antennas and Propagation*, 36(12):1760–1768, Dec 1988. Cited on pages 18, 19, and 24.

[11] B. Chang, G. Nave, and S. Jung. Drop formation from a wettable nozzle. *Communications in Nonlinear Science and Numerical Simulation*, 17(5):2045–2051, 2012. Cited on page 76.

[12] B. Chang, A. Shah, I. Routa, H. Lipsanen, and Q. Zhou. Low-height sharp edged patterns for capillary self-alignment assisted hybrid microassembly. *Journal of Micro-Bio Robotics*, 9(1):1–10, 2014. Cited on page 76.

[13] C.-T. Chang, J. B. Bostwick, S. Daniel, and P. H. Steen. Dynamics of sessile drops. Part 2. Experiment. *Journal of Fluid Mechanics*, 768:442–467, 2015. Cited on pages 18 and 56.

[14] C.-T. Chang, J. B. Bostwick, P. H. Steen, and S. Daniel. Substrate constraint modifies the Rayleigh spectrum of vibrating sessile drops. *Phys. Rev. E*, 88:023015, 2013. Cited on pages 18 and 56.

[15] D.-R. Chen and D. Y. H. Pui. Experimental investigation of scaling laws for electrospraying: Dielectric constant effect. *Aerosol Science and Technology*, 27(3):367–380, 1997. Cited on page 91.

[16] S. Chen, D. B. Johnson, P. E. Raad, and D. Fadda. The surface marker and micro cell method. *International Journal for Numerical Methods in Fluids*, 25(7):749–778, 1996. Cited on page 26.

[17] M. Cloupeau and B. Prunet-Foch. Electrohydrodynamic spraying functioning modes: a critical review. *Journal of Aerosol Science*, 25(6):1021–1036, 1994. Cited on pages 1, 90, and 92.

[18] R. T. Collins, K. Sambath, M. T. Harris, and O. A. Basaran. Universal scaling laws for the disintegration of electrified drops. *Proceedings of the National Academy of Sciences*, 110(13):4905–4910, 2013. Cited on pages 91, 95, 99, 104, and 137.

[19] R. Courant, K. Friedrichs, and H. Lewy. Über die partiellen Differenzengleichungen der mathematischen Physik. *Mathematische Annalen*, 100:32–74, 1928. Cited on page 32.

[20] J. Crank, P. Nicolson, and D. R. Hartree. A practical method for numerical evaluation of solutions of partial differential equations of the heat-conduction type. *Proceedings of the Cambridge Philosophical Society*, 43(1):50–67, 1947. Cited on page 32.

[21] H. Dastourani, M. R. Jahannama, and A. Eslami-Majd. A physical insight into electrospray process in cone-jet mode: Role of operating parameters. *International Journal of Heat and Fluid Flow*, 70:315–335, 2018. Cited on page 91.

[22] L. de Juan and J. Fernández de la Mora. Charge and size distributions of electrospray drops. *Journal of Colloid and Interface Science*, 186(2):280–293, 1997. Cited on pages 90 and 91.

[23] J. Fernández de la Mora. The fluid dynamics of Taylor cones. *Annual Review of Fluid Mechanics*, 39(1):217–243, 2007. Cited on pages 90 and 91.

[24] J. Fernández de la Mora and I. G. Loscertales. The current emitted by highly conducting Taylor cones. *Journal of Fluid Mechanics*, 260:155–184, 1994. Cited on pages 91 and 95.

[25] E. B. Dussan V. and S. H. Davis. On the motion of a fluid-fluid interface along a solid surface. *Journal of Fluid Mechanics*, 65(1):71–95, 1974. Cited on page 7.

[26] M. Enayati, M.-W. Chang, F. Bragman, M. Edirisinghe, and E. Stride. Electrohydrodynamic preparation of particles, capsules and bubbles for biomedical engineering applications. *Colloids and Surfaces A: Physicochemical and Engineering Aspects*, 382(1):154–164, 2011. A collection of papers from the 8th EUFOAM Conference and the Meetings of COST Actions D43 and P21. Cited on page 90.

[27] H. B. Eral, D. J. C. M. 't Mannetje, and J. M. Oh. Contact angle hysteresis: a review of fundamentals and applications. *Colloid and Polymer Science*, 291(2):247–260, Feb 2013. Cited on page 5.

[28] I. S. Fayzrakhmanova and A. V. Straube. Stick-slip dynamics of an oscillated sessile drop. *Physics of Fluids*, 21(7):072104, 2009. Cited on pages 17 and 59.

[29] E. Fehlberg. Low-order classical Runge-Kutta formulas with step-size control and their application to some heat-transfer problems. *NASA Technical Report 315*, 1969. Cited on page 15.

[30] S. Feier-Iova. *The Behaviour of Water Drops on Insulating Surfaces Stressed by Electric Field*. PhD thesis, Technische Universität, Darmstadt, December 2009. Cited on pages 48 and 49.

[31] S. Feier-Iova and V. Hinrichsen. Partial discharge inception voltage of water drops on insulating surfaces stressed by electrical field. In *2009 IEEE Electrical Insulation Conference*, pages 21–25, May 2009. Cited on pages 48 and 66.

[32] J. B. Fenn, M. Mann, C. K. Meng, S. F. Wong, and C. M. Whitehouse. Electrospray ionization for mass spectrometry of large biomolecules. *Science*, 246(4926):64–71, 1989. Cited on page 90.

[33] C. Ferrera, J. M. López-Herrera, M. A. Herrada, J. M. Montanero, and A. J. Acero. Dynamical behavior of electrified pendant drops. *Physics of Fluids*, 25, 2013. Cited on page 94.

[34] J. H. Ferziger and M. Perić. *Computational Methods for Fluid Dynamics*. Springer, Berlin, third edition, 2002. Cited on page 30.

[35] Thomas P. Forbes, F. Levent Degertekin, and Andrei G. Fedorov. Electrohydrodynamics of charge separation in droplet-based ion sources with time-varying electrical and mechan-

ical actuation. *Journal of the American Society for Mass Spectrometry*, 21(4):501–510, 2010. Cited on page 38.

[36] O. Fujii, K. Honsali, Y. Mizuno, and K. Naito. Vibration of a water droplet on a polymeric insulating material subjected to ac voltage stress. *IEEE Transactions on Dielectrics and Electrical Insulation*, 17(2):566–571, April 2010. Cited on pages 49 and 52.

[37] C. Galusinski and P. Vigneaux. On stability condition for bifluid flows with surface tension: Application to microfluidics. *Journal of Computational Physics*, 227(12):6140–6164, 2008. Cited on pages 36 and 74.

[38] M. Gamero-Castaño. The structure of electrospray beams in vacuum. *Journal of Fluid Mechanics*, 604:339–368, 2008. Cited on page 90.

[39] M. Gamero-Castaño and V. Hruby. Electrospray as a source of nanoparticles for efficient colloid thrusters. *Journal of Propulsion and Power*, 17(5):977–987, 2001. Cited on page 90.

[40] M. Gamero-Castaño and V. Hruby. Electric measurements of charged sprays emitted by cone-jets. *Journal of Fluid Mechanics*, 459:245–276, 2002. Cited on page 90.

[41] A. M. Gañán-Calvo, J. Dávila, and A. Barrero. Current and droplet size in the electrospraying of liquids. Scaling laws. *Journal of Aerosol Science*, 28(2):249–275, 1997. Cited on pages 90, 91, 103, and 104.

[42] A. M. Gañán-Calvo, J. M. López-Herrera, N. Rebollo-Muñoz, and J. M. Montanero. The onset of electrospray: The universal scaling laws of the first ejection. *Scientific Reports*, 6:32357, 2016. Cited on pages 91 and 100.

[43] A. M. Gañán-Calvo and J. M. Montanero. Revision of capillary cone-jet physics: Electrospray and flow focusing. *Phys. Rev. E*, 79:066305, 2009. Cited on page 100.

[44] H. Gao, Z. Jia, Y. Mao, Z. Guan, and L. Wang. Effect of hydrophobicity on electric field distribution and discharges along various wetted hydrophobic surfaces. *IEEE Transactions on Dielectrics and Electrical Insulation*, 15(2):435–443, April 2008. Cited on pages 49 and 66.

[45] S. J. Gaskell. Electrospray: Principles and practice. *Journal of Mass Spectrometry*, 32(7):677–688, 1997. Cited on page 90.

[46] R. S. Gorur, G. G. Karady, A. Jagota, M. Shah, and A. M. Yates. Aging in silicone rubber used for outdoor insulation. *IEEE Transactions on Power Delivery*, 7(2):525–538, April 1992. Cited on page 48.

[47] F. H. Harlow and J. E. Welch. Numerical calculation of time-dependent viscous incompressible flow of fluid with free surface. *The Physics of Fluids*, 8(12):2182–2189, 1965. Cited on page 26.

[48] C. W. Hirt and B. D. Nichols. Volume of fluid (VOF) method for the dynamics of free boundaries. *Journal of Computational Physics*, 39(1):201–225, 1981. Cited on page 27.

[49] R. L. Hoffman. A study of the advancing interface. I. Interface shape in liquid–gas systems. *Journal of Colloid and Interface Science*, 50(2):228–241, 1975. Cited on page 7.

[50] C. Huh and L. E. Scriven. Hydrodynamic model of steady movement of a solid/liquid/fluid contact line. *Journal of Colloid and Interface Science*, 35(1):85–101, 1971. Cited on page 7.

[51] M. Idemen. Confluent edge conditions for the electromagnetic wave at the edge of a wedge bounded by material sheets. *Wave Motion*, 32(1):37–55, 2000. Cited on page 24.

[52] R. I. Issa. Solution of the implicitly discretised fluid flow equations by operator-splitting. *J. Comput. Phys.*, 62(1):40–65, January 1986. Cited on page 33.

[53] H. Jasak. *Error Analysis and Estimation for the Finite Volume Method With Applications to Fluid Flows*. PhD thesis, Imperial College London, January 1996. Cited on page 29.

[54] A. Jaworek and A. Krupa. Classification of the modes of EHD spraying. *Journal of Aerosol Science*, 30(7):873–893, 1999. Cited on pages 1 and 90.

[55] S. Keim, D. Koenig, and V. Hinrichsen. Experimental investigations on electrohydrodynamic phenomena at single droplets on insulating surfaces. In *2003 Annual Report Conference on Electrical Insulation and Dielectric Phenomena*, pages 133–136, Oct 2003. Cited on page 48.

[56] S. F. Kistler. Hydrodynamics of wetting. *Wettability*, 6:311–430, 1993. Cited on pages 6 and 7.

[57] I. D. Koufogiannis, E. Sorolla, J. R. Mosig, and M. Mattes. Analyzing corona breakdown with a finite element-based electromagnetic solver. In *2013 7th European Conference on Antennas and Propagation (EuCAP)*, pages 2312–2314, April 2013. Cited on pages 64 and 65.

[58] A. Krivda and D. Birtwhistle. Breakdown between water drops on wet polymer surfaces. In *2001 Annual Report Conference on Electrical Insulation and Dielectric Phenomena (Cat. No.01CH37225)*, pages 572–580, 2001. Cited on page 48.

[59] H. Lamb. *Hydrodynamics*. Cambridge University Press, 1932. Cited on page 17.

[60] P. S. Laplace. *Traité De Mécanique Céleste: Supplément au dixième livre du traité de mécanique céleste sur l'action capillaire*. Number v. 6. Duprat, 1805. Cited on page 4.

[61] T. Latychevskaia and E. C. Meister. Axisymmetric liquid hanging drops. *Journal of chemical education*, 83:117–126, 12 2005. Cited on page 14.

[62] I. W. Lenggoro, K. Okuyama, J. Fernández de la Mora, and N. Tohge. Preparation of ZnS nanoparticles by electrospray pyrolysis. *Journal of Aerosol Science*, 31(1):121–136, 2000. Cited on page 90.

[63] L. K. Lim, J. Hua, C.-H. Wang, and K. A. Smith. Numerical simulation of cone-jet formation in electrohydrodynamic atomization. *AIChE Journal*, 57(1):57–78, 2011. Cited on page 91.

[64] Nicklas Linder. *Numerical Simulation of Complex Wetting*. PhD thesis, Technische Universität, Darmstadt, 2015. Cited on page 37.

[65] J. M. López-Herrera, A. M. Gañán-Calvo, S. Popinet, and M. A. Herrada. Electrokinetic effects in the breakup of electrified jets: A volume-of-fluid numerical study. *International Journal of Multiphase Flow*, 71:14–22, 2015. Cited on pages 38 and 117.

[66] J. M. López-Herrera, S. Popinet, and M. A. Herrada. A charge-conservative approach for simulating electrohydrodynamic two-phase flows using volume-of-fluid. *Journal of Computational Physics*, 230(5):1939–1955, 2011. Cited on page 38.

[67] J. Löwe and V. Hinrichsen. Experimental investigation of the influence of electric charge on the behavior of water droplets in electric fields. In *2019 IEEE 20th International Conference on Dielectric Liquids (ICDL)*, pages 1–6, June 2019. Cited on pages 52 and 60.

[68] J. Löwe, M. Secklehner, and V. Hinrichsen. Investigation of surface charges on polymeric insulators and the influence of sessile water droplets. In *2017 INSUCON - 13th International Electrical Insulation Conference (INSUCON)*, pages 1–7, May 2017. Cited on pages 56 and 60.

[69] J. Plog m, J.-M. Löwe, Y. Jiang, Y. Pan, and A. L. Yarin. Control of direct written ink droplets using electrowetting. *Langmuir*, 35(34):11023–11036, 2019. PMID: 31345035. Cited on page 118.

[70] G. I. Makarov and A. V. Osipov. Structure of Meixner's series. *Radiophysics and Quantum Electronics*, 29(6):544–549, June 1986. Cited on pages 18 and 24.

[71] C. Marangoni. *Sull'espansione delle goccie d'un liquido galleggianti sulla superfice di altro liquido*. Fratelli Fusi, 1865. Cited on page 4.

[72] B. Marungsri, W. Onchantuek, A. Oonsivilai, and T. Kulworawanichpong. Analysis of electric field and potential distributions along surface of silicone rubber insulators under various contamination conditions using finite element method. *International Journal of Electrical and Computer Engineering*, 3(5):1237 – 1247, 2009. Cited on page 49.

[73] J. Meixner. The behavior of electromagnetic fields at edges. *IEEE Transactions on Antennas and Propagation*, 20(4):442–446, July 1972. Cited on page 18.

[74] J. R. Melcher. *Continuum Electromechanics*. MIT Press, 1981. Cited on pages 8, 9, and 10.

[75] J. R. Melcher and G. I. Taylor. Electrohydrodynamics: A review of the role of interfacial shear stresses. *Annual Review of Fluid Mechanics*, 1(1):111–146, 1969. Cited on page 12.

[76] F. Mugele and J.-C. Baret. Electrowetting: from basics to applications. *Journal of Physics: Condensed Matter*, 17(28):R705–R774, July 2005. Cited on pages 1 and 7.

[77] M. H. Nazemi. *Experimental Investigations on Water Droplets on Polymeric Insulating Surfaces under the Impact of High Electric Fields*. PhD thesis, Technische Universität Darmstadt, Darmstadt, April 2016. Cited on pages 48, 51, 66, 68, and 69.

[78] N. Nikolopoulos, K.-S. Nikas, and G. Bergeles. A numerical investigation of central binary collision of droplets. *Computers and Fluids*, 38(6):1191–1202, 2009. Cited on page 79.

[79] F. Olyslager. The behavior of electromagnetic fields at edges in bi-isotropic and bi-anisotropic materials. *IEEE Transactions on Antennas and Propagation*, 42(10):1392–1397, Oct 1994. Cited on page 18.

[80] Openfoam 4.x. `http://www.openfoam.org`, 2016 (Retrieved September 2017). Cited on page 27.

[81] S. Osher and J. A. Sethian. Fronts propagating with curvature-dependent speed: Algorithms based on Hamilton-Jacobi formulations. *Journal of Computational Physics*, 79(1):12–49, 1988. Cited on page 26.

[82] Y. Ouedraogo, E. Gjonaj, H. De Gersem, and S. Schöps. Simulation of transient electrospray dynamics in conductive fluids. *IEEE Transactions on Magnetics*, 56(2), 2020. Cited on pages 2, 91, 99, and 101.

[83] Y. Ouedraogo, E. Gjonaj, T. Weiland, H. De Gersem, C. Steinhausen, G. Lamanna, B. Weigand, A. Preusche, A. Dreizler, and M. Schremb. Electrohydrodynamic simulation of electrically controlled droplet generation. *International Journal of Heat and Fluid Flow*, 64:120–128, 2017. Cited on pages 2, 47, 73, 75, 79, 83, 84, 85, and 87.

[84] A. J. Phillips, D. J. Childs, and H. M. Schneider. Aging of nonceramic insulators due to corona from water drops. *IEEE Transactions on Power Delivery*, 14(3):1081–1089, July 1999. Cited on pages 48 and 66.

[85] R. Pillai, J. Berry, D. Harvie, and M. Davidson. Electrokinetics of isolated electrified drops. *Soft Matter*, 12, 2016. Cited on page 91.

[86] A. Prosperetti. Linear oscillations of constrained drops, bubbles, and plane liquid surfaces. *Physics of Fluids*, 24(3):032109, 2012. Cited on page 17.

[87] S. Quan and D. P. Schmidt. A moving mesh interface tracking method for 3d incompressible two-phase flows. *Journal of Computational Physics*, 221(2):761–780, 2007. Cited on page 26.

[88] D. Quéré. Wetting and roughness. *Annual Review of Materials Research*, 38(1):71–99, 2008. Cited on page 76.

[89] D. Rettenmaier, D. Deising, Y. Ouedraogo, E. Gjonaj, H. De Gersem, D. Bothe, C. Tropea, and H. Marschall. Load balanced 2D and 3D adaptive mesh refinement in OpenFOAM. *SoftwareX*, 10:100317, 2019. Cited on pages 41 and 42.

[90] S. N. Reznik, A. L. Yarin, A. Theron, and E. Zussman. Transient and steady shapes of droplets attached to a surface in a strong electric field. *Journal of Fluid Mechanics*, 516:349–377, 2004. Cited on page 91.

[91] W. Rohlfs, G. F. Dietze, H. D. Haustein, and R. Kneer. Two-phase electrohydrodynamic simulations using a volume-of-fluid approach: A comment. *Journal of Computational Physics*, 231(12):4454 – 4463, 2012. Cited on page 38.

[92] I. V. Roisman, L. Opfer, C. Tropea, M. Raessi, J. Mostaghimi, and S. Chandra. Drop impact onto a dry surface: Role of the dynamic contact angle. *Colloids and Surfaces A: Physicochemical and Engineering Aspects*, 322(1–3):183 – 191, 2008. Cited on page 37.

[93] H. Rusche. *Computational fluid dynamics of dispersed two-phase flows at high phase fractions*. PhD thesis, Imperial College London, 2003. Cited on page 35.

[94] S. M. I. Saad and A. W. Neumann. Axisymmetric drop shape analysis (ADSA): An outline. *Advances in Colloid and Interface Science*, 238:62–87, 2016. Cited on pages 14 and 16.

[95] Y. Saad. *Iterative Methods for Sparse Linear Systems*. Society for Industrial and Applied Mathematics, Philadelphia, PA, USA, 2nd edition, 2003. Cited on page 32.

[96] K. Sarkar, P. Hoos, and A. Urias. Numerical Simulation of Formation and Distortion of Taylor Cones. *Journal of Nanotechnology in Engineering and Medicine*, 3(4), 2013. 041001. Cited on page 91.

[97] D. A. Saville. Electrohydrodynamics: The Taylor-Melcher leaky dielectric model. *Annual Review of Fluid Mechanics*, 29(1):27–64, 1997. Cited on page 11.

[98] T. Schutte and S. Hornfeldt. Dynamics of electrically stressed water drops on insulating surfaces. In *IEEE International Symposium on Electrical Insulation*, pages 202–207, June 1990. Cited on page 48.

[99] J. S. Sharp, D. J. Farmer, and J. Kelly. Contact angle dependence of the resonant frequency of sessile water droplets. *Langmuir*, 27(15):9367–9371, 2011. PMID: 21682292. Cited on page 18.

[100] A. T. Shih and C. M. Megaridis. Suspended droplet evaporation modeling in a laminar convective environment. *Combustion and Flame*, 102(3):256–270, 1995. Cited on page 72.

[101] Y. D. Shikhmurzaev. Dynamic contact angles and flow in vicinity of moving contact line. *AIChE Journal*, 42(3):601–612, 1996. Cited on page 6.

[102] M. Shojaeian and S. Hardt. Fast electric control of the droplet size in a microfluidic T-junction droplet generator. *Applied Physics Letters*, 112(19):194102, 2018. Cited on page 118.

[103] H. Songoro. *Electrohydrodynamic Modeling of Droplet Vibrations under the Influence of Electric Fields*. PhD thesis, Technische Universität Darmstadt, Darmstadt, March 2015. Cited on pages 26 and 49.

[104] F. E. Sorolla Rosario. *Contribution to modeling multipactor and corona discharges in high power electromagnetic fields*. PhD thesis, EPFL, Lausanne, 2012. Cited on page 64.

[105] C. Steinhausen, G. Lamanna, B. Weigand, R. Stierle, J. Gross, A. Preusche, and A. Dreizler. Experimental investigation of droplet injections in the vicinity of the critical point: A comparison of different model approaches. In *Proceedings ILASS–Europe 2017. 28th Conference on Liquid Atomization and Spray Systems*, 2017. Cited on pages 72 and 73.

[106] J. Stengele, K. Prommersberger, M. Willmann, and S. Wittig. Experimental and theoretical study of one- and two-component droplet vaporization in a high pressure environment. *International Journal of Heat and Mass Transfer*, 42(14):2683 – 2694, 1999. Cited on pages 1 and 72.

[107] H. A. Stone, J. R. Lister, and M. P. Brenner. Drops with conical ends in electric and magnetic fields. *Proceedings of the Royal Society of London. Series A: Mathematical, Physical and Engineering Sciences*, 455:329–347, 1999. Cited on page 91.

[108] M. Strani and F. Sabetta. Free vibrations of a drop in partial contact with a solid support. *Journal of Fluid Mechanics*, 141:233–247, 1984. Cited on page 17.

[109] T. Takuma, T. Kawamoto, and H. Fujinami. Effect of conduction on field behavior near singular points in composite medium arrangements. *IEEE Transactions on Electrical Insulation*, EI-17(3):269–275, June 1982. Cited on page 18.

[110] K. Tang and A. Gomez. Generation by electrospray of monodisperse water droplets for targeted drug delivery by inhalation. *Journal of Aerosol Science*, 25(6):1237–1249, 1994. Cited on page 90.

[111] K. Tang and A. Gomez. On the structure of an electrostatic spray of monodisperse droplets. *Physics of Fluids*, 6(7):2317–2332, 1994. Cited on pages 90 and 92.

[112] K. Tang and A. Gomez. Generation of monodisperse water droplets from electrosprays in a corona-assisted cone-jet mode. *Journal of Colloid and Interface Science*, 175(2):326–332, 1995. Cited on page 90.

[113] K. Tang and A. Gomez. Monodisperse electrosprays of low electric conductivity liquids in the cone-jet mode. *Journal of Colloid and Interface Science*, 184(2):500–511, 1996. Cited on pages 90, 91, 100, 107, 108, 113, and 137.

[114] G. Taylor. Disintegration of water drops in an electric field. *Proceedings of the Royal Society of London. Series A, Mathematical and Physical Sciences*, 280(1382):383–397, 1964. Cited on page 90.

[115] B. Techaumnat, S. Hamada, and T. Takuma. Effect of conductivity in triple-junction problems. *Journal of Electrostatics*, 56(1):67–76, 2002. Cited on page 23.

[116] R. H. Temperton and J. S. Sharp. Vibrational modes of elongated sessile liquid droplets. *Langmuir*, 29(15):4737–4742, 2013. PMID: 23517045. Cited on pages 18 and 59.

[117] J. Thomson. XLII. On certain curious motions observable at the surfaces of wine and other alcoholic liquors. *The London, Edinburgh, and Dublin Philosophical Magazine and Journal of Science*, 10(67):330–333, 1855. Cited on page 4.

[118] G. Tomar, D. Gerlach, G. Biswas, N. Alleborn, A. Sharma, F. Durst, S. W. J. Welch, and A. Delgado. Two-phase electrohydrodynamic simulations using a volume-of-fluid approach. *Journal of Computational Physics*, 227(2):1267–1285, 2007. Cited on page 38.

[119] Z. Tukovic and H. Jasak. A moving mesh finite volume interface tracking method for surface tension dominated interfacial fluid flow. *Computers and Fluids*, 55:70–84, 02 2012. Cited on page 26.

[120] S. O. Unverdi and G. Tryggvason. A front-tracking method for viscous, incompressible, multi-fluid flows. *Journal of Computational Physics*, 100(1):25–37, 1992. Cited on page 26.

[121] J. Vejrazka, L. Vobecka, and J. Tihon. Linear oscillations of a supported bubble or drop. *Physics of Fluids*, 25(6):062102, 2013. Cited on page 17.

[122] L. F. Velásquez-García, A. I. Akinwande, and M. Martínez-Sánchez. A planar array of micro-fabricated electrospray emitters for thruster applications. *Journal of Microelectromechanical Systems*, 15(5):1272–1280, Oct 2006. Cited on page 90.

[123] S. Verdoold, L. L. F. Agostinho, C. U. Yurteri, and J. C. M. Marijnissen. A generic electrospray classification. *Journal of Aerosol Science*, 67:87–103, 2014. Cited on page 90.

[124] C. P. Vicente Quiles. *Passive Intermodulation and Corona Discharge for Microwave Structures in Communications Satellites*. PhD thesis, Technische Universität Darmstadt, Darmstadt, August 2005. Cited on page 64.

[125] O. V. Voinov. Hydrodynamics of wetting. *Fluid Dynamics*, 11(5):714–721, Sep 1976. Cited on page 6.

[126] T. Voskuilen. Mesh balancing. `https://github.com/tgvoskuilen/meshBalancing`, 2014 (Retrieved July 2018). Cited on page 41.

[127] K. W. Wagner. Erklärung der dielektrischen Nachwirkungsvorgänge auf Grund Maxwellscher Vorstellungen. *Archiv für Elektrotechnik*, 2(9):371–387, Sep 1914. Cited on page 44.

[128] P. C. Wayner. Intermolecular forces in phase-change heat transfer: 1998 Kern Award Review. *AIChE Journal*, 45(10):2055–2068, 10 1999. Cited on page 72.

[129] F. Weckenmann, B. Bork, E. Oldenhof, G. Lamanna, B. Weigand, B. Boehm, and A. Dreizler. Single acetone droplets at supercritical pressure: Droplet generation and characterization of PLIFP. *Zeitschrift Fur Physikalische Chemie – International Journal of Research in Physical Chemistry and Chemical Physics*, 225:1417–1431, 2011. Cited on pages 72, 73, and 79.

[130] J. Wei, W. Shui, F. Zhou, Y. Lu, K. Chen, G. Xu, and P. Yang. Naturally and externally pulsed electrospray. *Mass Spectrometry Reviews*, 21(3):148–162, 2002. Cited on page 91.

[131] W. Wei, Z. Gu, S. Wang, Y. Zhang, K. Lei, and K. Kase. Numerical simulation of the cone–jet formation and current generation in electrostatic spray—modeling as regards space charged droplet effect. *Journal of Micromechanics and Microengineering*, 23(1):015004, 2013. Cited on pages 91 and 99.

[132] H. G. Weller. A new approach to VOF-based interface capturing methods for incompressible and compressible flow. *OpenCFD Ltd., Report TR/HGW/04*, 2008. Cited on page 35.

[133] Q. Xu, H. Qin, Z. Yin, J. Hua, D. W. Pack, and C.-H. Wang. Coaxial electrohydrodynamic atomization process for production of polymeric composite microspheres. *Chemical Engineering Science*, 104:330–346, 2013. Cited on page 91.

[134] Q. Yang, B. Q. Li, and Y. Ding. 3D phase field modeling of electrohydrodynamic multiphase flows. *International Journal of Multiphase Flow*, 57:1–9, 2013. Cited on page 39.

[135] V. Yang. Modeling of supercritical vaporization, mixing, and combustion processes in liquid-fueled propulsion systems. *Proceedings of the Combustion Institute*, 28(1):925–942, 2000. Cited on page 72.

[136] K. Yokoi, D. Vadillo, J. Hinch, and I. Hutchings. Numerical studies of the influence of the dynamic contact angle on a droplet impacting on a dry surface. *Physics of Fluids*, 21(7):072102, 2009. Cited on page 6.

[137] T. Young. III. An essay on the cohesion of fluids. *Philosophical Transactions of the Royal Society of London*, 95:65–87, 1805. Cited on page 4.

[138] C. U. Yurteri, R. P. A. Hartman, and J. C. M. Marijnissen. Producing pharmaceutical particles via electrospraying with an emphasis on nano and nano structured particles - a review. *KONA Powder and Particle Journal*, 28:91–115, 2010. Cited on page 90.

[139] X. Zhang and O. A. Basaran. An experimental study of dynamics of drop formation. *Physics of Fluids*, 7(6):1184–1203, 1995. Cited on page 83.

[140] X. Zhang and O. A. Basaran. Dynamics of drop formation from a capillary in the presence of an electric field. *Journal of Fluid Mechanics*, 326:239–263, 11 1996. Cited on page 83.

[141] Y. Zhu, K. Haji, M. Otsubo, C. Honda, and N. Hayashi. Electrohydrodynamic behaviour of water droplet on an electrically stressed hydrophobic surface. *Journal of Physics D: Applied Physics*, 39(9):1970–1975, 2006. Cited on page 49.

List of Acronyms and Symbols

Acronyms

1D	one-dimension
2D	two-dimensions
3D	three-dimensions
BC	Boundary Condition
CFL	Courant-Friedrichs-Lewy
CSF	Continuum Surface Force
EHD	Electrohydrodynamic
EQS	Electroquasistatic
FEM	Finite Element Method
FVM	Finite Volume Method
MPI	Message Passing Interface
MULES	Multidimensional Universal Limiter for Explicit Solutions
PD	Partial Discharge
PDE	Partial Differential Equation
PISO	Pressure-Implicit with Splitting of Operators
rms	root mean square
SiR	Silicone Rubber
VoF	Volume of Fluid

Symbols

$\mathbf{C}$	cell centroid
$\mathbf{C}_f$	face centroid
Ca	capillary number
D	diffusion coefficient
$\mathbf{D}$	electric displacement field
$\mathbf{d}_f$	length vector between cell centroids
$\mathbf{E}$	electric field
e	elementary charge

f_{H}	Hoffman's empirical function
$\mathbf{f}_{\mathrm{c}}$	Lorentz force density acting on free charge
$\mathbf{f}_{\mathrm{e}}$	electric force density
$\mathbf{f}_{\mathrm{p}}$	polarization force density
$\mathbf{f}_{\mathrm{s}}$	surface tension force density
$\mathbf{g}$	gravitational acceleration
$\mathbb{I}$	unit tensor
K	interface curvature
k_{B}	Boltzmann's constant
l_{μ}	characteristic viscous length
m	singularity index
n	concentration
$\mathbf{n}$	interface normal
$\mathbf{P}$	polarization density
Pe	Péclet number
$\mathbf{p}$	electric dipole moment
p	pressure
p_{d}	dynamic pressure
R_1	first principal radius of curvature
R_2	second principal radius of curvature
$\mathbf{S}_f$	face area vector
S	surface
$\mathbb{T}_{\mathrm{e}}$	electromechanical stress tensor
T	temperature
t	time
$\mathbf{u}_k$	unit vector associated to k
$\mathbf{u}$	velocity
V	volume
V_{P}	control volume
V_{cl}	contact line velocity
z	valency

Greek symbols

α	volume fraction field
α	ionisation coefficient
β	dimensionless electric field strength
γ	surface tension

δ_{ij}	Kronecker delta
ε	electric permittivity
ε_0	vacuum electric permittivity
ε_r	relative electric permittivity
η	attachment coefficient
θ	contact angle
θ_{adv}	limiting advancing contact angle
θ_{dyn}	dynamic contact angle
θ_{e}	equilibrium contact angle
θ_{rec}	limiting receding contact angle
κ	electrical conductivity
μ	dynamic viscosity
ρ	material density
ϱ_{e}	free charge density
τ_{D}	characteristic diffusion time
τ_{e}	charge relaxation time scale
τ_{m}	magnetic time scale
τ_{P}	transport process time scale
Φ	electric potential
ϕ	volumetric flux
ϕ_{m}	mass flux
χ_{e}	electric susceptibility
ω	angular frequency
ω	mobility

List of Figures

5 Droplet Oscillations on High Voltage Insulators

6 Electrically Forced Droplet Generation

7 Transient Electrosprays

List of Tables

Acknowledgements

I would like to express here my gratitude to the many people who have made this thesis possible:

- Prof. Dr.-Ing. Herbert De Gersem for giving me the opportunity to work at TEMF and hosting this project.
- PD Dr. rer. nat. habil. Erion Gjonaj for his day-to-day supervision. His suggestions and critical reviews played a major role in improving my work.
- Prof. Dr.-Ing. Cameron Tropea for kindly accepting to be a co-referee for my thesis.
- Prof. Dr. rer. nat. Sebastian Schöps for his valuable comments on my thesis.
- Christoph Steinhausen, Andreas Preusche, Jens Löwe for providing experimental data.
- Thomas Antritter, Achim Bender, Benjamin Franz, Dr.-Ing. Daniel Rettenmaier and Christiane Schlawitschek with whom I had the pleasure to collaborate on extending to the OpenFOAM library, making many of the computations presented in this thesis possible.
- The administrative and technical staff of TEMF, Heike Koch, Dragos Munteanu and Achim Wagner.
- Dr. phil. nat. Wolfgang Müller for his precious help with the cluster.
- My colleagues at TEMF for the very friendly atmosphere and daily discussions. I would like to especially thank my coworkers in the research group Coupled Problems, Kyle Taylor, Steffen Schmid and Dr.-Ing. Yvonne Späck-Leigsnering for the many interesting discussions.
- My family for their unconditional love and continuous encouragement.

I would like to acknowledge the Deutsche Forschungsgemeinschaft (DFG) for their financial support, in the framework of the Collaborative Research Center Transregio 75 “Droplet Dynamics under Extreme Ambient Conditions”.